MECHANICAL PROPERTIES OF ONE-DIMENSIONAL NANOSTRCTURES, EXPERIMENTAL MEASUREMENT AND NUMERICAL SIMULATION

by

Xiaoxia Wu

A dissertation submitted to the faculty of
The University of North Carolina at Charlotte
in partial fulfillment of the requirements
for the degree of Doctor of Philosophy in
Mechanical Engineering

Charlotte

2012

Approved by:

Dr. Terry T. Xu

Dr. Ronald E. Smelser

Dr. Aixi Zhou

Dr. Doug Cooper

ABSTRACT

XIAOXIA WU. Mechanical properties of one-dimensional nanostructures, experimental measurement and numerical simulation (Under the direction of DR. TERRY T. XU)

One-Dimensional (1D) nanostructures are generally defined as having at least one dimension between 1 and 100 nm. Investigations of their mechanical properties are important from both fundamental study and application point of view. Different methods such as *in-situ* tensile test and Atomic Force Microscopy (AFM) bending test have been used to explore the mechanical properties of 1D nanostructures. However, searching for reliable measurement of 1D nanostructures is still under way. In this dissertation, two methods, Atomic Force Acoustic Microscopy (AFAM)-based method and nanoindentation, were explored to realize reliable study of mechanical properties of two kinds of energy conversion-related nanomaterials: single crystalline rutile TiO_2 nanoribbons and alkaline earth metal hexaboride MB_6 (M=Ca, Sr, Ba) 1D nanostructures.

The work principle of AFAM-based method is: while an AFM cantilever is in contact with a tested nanostructure, its *contact* resonance frequencies are different from its *free* resonance frequencies. The cantilever resonant frequency shift is correlated to the Young's modulus of the tested nanostructure based on Hertz contact mechanics. The measured modulus of BaB_6 nanostructures was 129 GPa, which is much lower than the value determined using the nanoindentation method. Due to the small load (120 nN) applied on the nanostructure during the experiment, the AFAM-based method may actually measure the mechanical property of the outside oxidation layers of BaB_6 nanostructures.

Nanoindentation is capable of giving insights to both Young's modulus and hardness of bulk elastic-plastic materials. The assumptions behind this method are that the material being tested is a homogeneous half-space. Cares must be taken to extract properties of tested materials when those assumptions are broken down. Nanoindentation on a 1D nanostructure is one of such cases that those assumptions are invalid. However, this invalidity was not realized in most published work on nanoindentation of 1D nanostructures, resulting in unreliable data on mechanical properties of 1D nanostructures. In this work, factors which could affect measured nanostructure-on-substrate system modulus such as the selection of a substrate to support the nanostructure, the cross section of a nanostructure, the width-to-thickness ratio (or diameter) of a nanostructure, and the nanostructure-substrate contact mechanism were first subjected to a systematic experimental investigation. A Finite Element Modeling (FEM)-based data inverse analysis process was then proposed to extract the intrinsic modulus of nanostructures from measured system modulus. This data inverse process solved the intrinsic modulus of nanostructures by equalizing the simulated nanostructure-on-substrate modulus with the experimentally measured system modulus. In finite element simulation, another important aspect: the experimental indenter area function in addition to aforementioned other factors was carefully considered. Based on systematic experimental and numerical investigations, the Young's modulus of rutile TiO_2 nanoribbons, CaB_6 nanostructures, SrB_6 nanostructures and BaB_6 nanostructures was determined to be 360, 175-365, 300-425 and 270-475 GPa, respectively. These numbers are the first reported mechanical properties for these nanomaterials. Besides the finite element simulation, an "analytical" solution to obtain a nanostructure-on-substrate system modulus is also presented.

Compared to the finite element simulation, the solution could significantly reduce processing time for the data inverse method. It is applicable to a nanostructure with a width to thickness ratio larger than 4. This part of dissertation work clearly demonstrates that both experimental and numerical investigations are needed for studying of mechanical properties of 1D nanostructures by nanoindentation.

ACKNOWLEDGMENTS

My deepest gratitude is to my advisor, Dr. Terry T. Xu. I would not have gone this far without her encouragement and support from every aspects, research and personal life. Dr. Xu is so knowledgeable that she always can guide me to a meaningful research direction. She sponsored me to attend workshops and conferences, which definitely broaden my horizon and sharpen my skills of presentation. I thank her for being a good role model in paying attention to details, organizing data and thoughts clearly and thoroughly. I am also truly indebted to Dr. Ronald E. Smelser, who inspired me with his personal experiences in pursuit his PHD degree. His long-term spiritual support and encouragement will be valuable treasures throughout my life. I am grateful to Dr. Aixi Zhou and Dr. Doug Couper for their insightful comments on the topic, which motivate me for a clear presentation. I am thankful to the Center of Metrology, Department of Mechanical Engineering and Engineering Science, and the Center of Optoelectronics and Optical Communications at UNC Charlotte for providing multi-user SEM, AFM and nanoindentation. I appreciate the valuable suggestions and comments from Professor Xiaodong Li at University of South Carolina, Professor Gang Feng at Villanova University and supporting staff at Agilent Technology nanomechanics division for nanoindentation usage. I thank Professor Stuart Smith and his group for helping me with LabVIEW programming and hardware hook-up in the AFAM based method. I would like to thank Dr. Haitao Zhang for all the advice, suggestions and training. I am thankful to Dr. Harish Cherukuri for his guidance and advice regarding course works and graduate study. I also thank helps and supports from my fellow students and friends, Zhiliang Pan, Zhe Guan, Youfei Jiang, Jing Bi among many others.

I appreciate the financial support from the National Science Foundation (CMMI 0800366 and 0748090), the American Chemical Society - Petroleum Research Fund (PRF No. 44245-G10), and The University of North Carolina at Charlotte (UNC Charlotte).

Finally, I thank my parents, Jun Wu and Guolan Jiang, for their love, encouragement and inspiration. My appreciation also goes to my husband, Jinquan Cheng, for his support.

TABLE OF CONTENTS

LISTS OF TABLES

LISTS OF FIGURES

CHAPTER 1: INTRODUCTION

1.1 Motivation

One-Dimensional (1D) nanostructures are generally defined as having at least one dimension in somewhere between 1 and 100 nm (Xia, *et al.*, 2003). Depending on their morphology, 1D nanostructures can be further divided into nanobelts (NB), nanotubes (NT), nanowires (NW), nanorods, nanosprings, and nanoribbons *etc*.

From a theoretical point of view, nanostructures are different from their bulk counterparts in the following two ways: (i) the extremely small scale of nanostructures could result in a less-defect structure. The mechanical properties, such as Young's modulus and yield strength, could reach the theoretical limit. For example, single wall carbon NTs have demonstrated exceptional mechanical properties: very high Young's modulus of 1.25 TPa (Krishnan, *et al.*, 1998) and tensile strength of 200 GPa (Zhao, *et al.*, 2002); fully reversible bending for high bending angles (Iijima, *et al.*, 1996). (ii) large surface area to volume ratio, which might results in size effect of nanostructures. Surface atoms have different electron densities and fewer bonding neighbors than atoms inside a nanostructure. Molecular dynamic simulations have revealed that surface atoms could either increase or decrease the elastic stiffness (Miller and Shenoy, 2000, Park, *et al.*, 2009). With an electric-field-induced resonance method, Young's modulus of ZnO NWs was found to increase dramatically as diameters decrease (Chen, *et al.*, 2006). However, recent *in-situ* tensile tests of Si NW indicated that Young's modulus decreased from their bulk Young's modulus for NWs with diameters being less than 30 nm (Zhu, *et al.*,

2009). Moreover, bending tests showed that Young's modulus of gold NWs was essentially diameter independent (Wu, *et al.*, 2005). In summary, nanostructures could show higher, lower or comparable modulus to their bulk counterparts. But the questions are: will all nanostructures have a mechanical property that's upto their theoretical limit just like single wall carbon nanotubes? Or are the mechanical properties close to their bulk counterparts? Will mechanical properties of 1D nanostructures show size effect or not? To answer these questions, the mechanical property of a 1D nanostructure needs to be carefully studied from a theoretical and an experimental point of view.

On the other hand, studying the mechanical property of the 1D nanostructures is important from an application point of view. If nanostructures are to play some roles in a building block for future nanotechnology, a thorough understanding of their mechanical behavior is essential. As we know, for bulk material applications in engineering, structural engineering design always requires a safety factor (*SF*), which is defined as $SF=UTS/R$, where R is the applied stress and UTS is the ultimate tensile strength. The same philosophy applies to possible design of a nanostructure device. The applied stress on a nanostructure needs to be carefully designed so that the nanostructure can be operated safely. To design the working stress, mechanical properties, such as Young's modulus and yield strength need to be well understood. As a result, studying mechanical property of nanostructures is important from an application point of view.

1.2 Some General Terms

Before discussing the currently available techniques for mechanical tests of 1D nanostructures, it is beneficial to describe some general terms which will be used extensively throughout the dissertation.

1.2.1 EBID

Electron Beam Induced Deposition (EBID) is a material deposition technique that has been around since 1934 when Steward found contamination growth in his electron optical system (van Dorp and Hagen, 2008). The basic principle of EBID is: Gas molecules - from either contamination or introduced precursor gas, liquid or solid material in a Scanning Electron Microscope (SEM) chamber - are dissociated into volatile and nonvolatile components under the influence of a SEM e-beam. Nonvolatile components adhere to the substrate, where deposition is supposed to occur, and form deposition (EBID). Alternatively, nonvolatile components react with substrate to form volatile components and leave a trench on the substrate.

In mechanical testing of nanostructures, EBID is generally used to bond nanostructures onto a test apparatus. The general procedures are: (i) Attach the nanostructure onto the test apparatus and locate one end of the nanostructure under SEM; (ii) Zoom in to the end of the nanostructure with the image center being the location where deposition will occur. Choose a right accelerating voltage and spot size of SEM; (iii) contamination inside the SEM chamber will be dissociated, and carbon will deposit onto the nanostructure and affix the nanostructure onto the test apparatus.

1.2.2 AFM

Atomic Force Microscopy (AFM), invented by Binnig, Quate and Gerber in 1986 (Binnig, *et al.*, 1986), is one of several very high-resolution Scanning Probe Microscopes (SPM). It has resolution of a nanometer, which is more than 1000 times larger than the optical diffraction limit. As shown in Figure 1.1 (A), AFM consists of the following main parts: (1) a cantilever, the sensing part of the AFM. It is typically made of silicon or

silicon nitride with a sharp tip at its end. Figure 1.1 (B) shows a commercial AFM cantilever with a rectangular cross section. There are also triangular cantilevers, which typically have a smaller spring constant; (2) a PZT scanner to move the AFM tip related to the tested sample. Depending on the AFM mode, the scanner could be affixed to the sample stage and the cantilever will hold still during the scanning process, as shown in Figure 1.1 (A). The scanner could also be affixed to the cantilever holder while the sample is stationary; (3) laser and photodiode used to detect AFM cantilever deflection and (4) feedback electronics to control the scanner's up and down movement so that the AFM cantilever deflection is kept constant. The trace of the scanner movement corresponds to the sample topography.

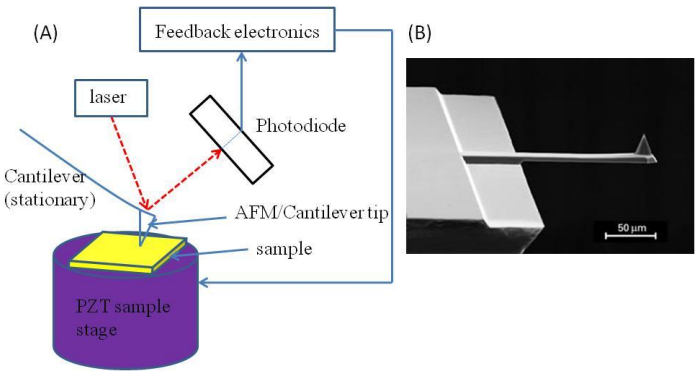

Figure 1.1: (A) Schematic illustration of the main components of an AFM. (B) An AFM cantilever with a sharp tip on one end and attaches to a chip on the other end. (Image courtesy www.schaefer-tec.com)

Depending on an application, AFM is working either in image mode or force mode. In image mode, the cantilever tip is brought into contact with the sample through extending the PZT scanner or the sample stage. Interaction forces between the AFM tip

and the sample, such as Van der Waals force, contact force or adhesion, are kept constant by holding the AFM cantilever deflection constant. While in force mode, the cantilever is continuously pushed against the tested sample. In other words, the load applied on the tested sample increases with time. With a well-calibrated cantilever spring constant k_c, the force-scanner movement curve could be used to extract the mechanical property of a tested sample, as discussed in Section 1.3.3.

Since the forces applied on a sample by an AFM cantilever are determined by cantilever spring constant and its defection, accurately calibrating cantilever spring constant is critical for AFM based mechanical measurement methods. There are many different ways to calibrate the cantilever spring constant k_c, as reviewed by Butt *et al.* (Butt, *et al.*, 2005), Pettersson *et al.* (Pettersson, *et al.*, 2007) and Palacio and Bhushan (Palacio and Bhushan, 2010). Here we have briefly summarized their findings. For normal cantilever spring constant calibration, the AFM cantilever is pushed vertically against a tested structure. The calibration methods include, but are not limited to, the following: (1) Calculation from its geometry parameters. For a cantilever with a constant rectangular cross-section, $k_c = \frac{Ewt^3}{4L^3}$, where E is Young's modulus of the material that the cantilever is made of, w, t, L are width, thickness and length of the cantilever, respectively. The calculated spring constant is typically different from the experimentally determined ones. This discrepancy is due to many reasons, such as a non-uniform cantilever thickness, and the oxidation layer on the top and bottom of the cantilever, among others. (2) Measurement using a thermal noise method (Hutter and Bechhoefer, 1993). It is one of the widely used methods and implemented in many commercial AFMs. A cantilever is generally simplified as a spring-mass system. The effective spring

constant is related to its mean square deflection $< \Delta Z_c^2 >$ under thermal fluctuation, that is, $k_c = \frac{k_B T}{<\Delta Z_c^2>}$, where k_B is the Boltzmann constant and T is the absolute temperature of the calibration. (3) Measurement by adding a known mass. The spring constant is extracted from shift of the resonance frequencies before and after a known mass is added. Note that adding mass to a cantilever tip and sticking them together could be a nontrivial job. (4) Measurement using a reference cantilever (meetings.aps.org/meeting/MAR07/event/) or by directly applying a known force to the cantilever and measuring its deflection. The cantilever spring constant can be determined from the force-deflection curve. Nowadays, some AFM cantilever vendors calibrate their cantilevers individually using one of the aforementioned methods. In such case, no further cantilever spring constant is needed.

For lateral cantilever spring constant calibration, currently available calibration methods include, but are not limited to the following: (1) Calculating from its geometry parameters. Similar to the normal spring constant calibration, this method could suffer from significant errors because of the uncertainty of the AFM cantilever dimension; (2) Scanning tip on an inclined surface with a known slope and obtaining the spring constant through force balance equations (Ogletree, *et al.*, 1996). The method is very complicated and could wear the AFM tip; and (3) The resonant frequency method (Jeon, *et al.*, 2004). By applying an electrical current to a triangular cantilever in a magnetic field, the cantilever is excited into torsion. The cantilever lateral spring constant can be calculated from the torsional resonant frequency. Unfortunately, this method could not be used for cantilevers with a rectangular cross section. Cantilever lateral spring constant is generally more difficult to calibrate than normal spring constant.

Cantilevers are typically mounted under a certain tilt angle with respect to sample's surface. The tilt is necessary to ensure that the tip, rather than the chip onto which the cantilever is attached, touches the sample first (Heim, *et al.*, 2004, Stiernstedt, *et al.*, 2005). The tilt angle ranges from 7^o to 20^o in commercial AFMs. Due to the tilt, the effective spring constant of a rectangular cantilever should be obtained by dividing the calibrated spring constant by a factor $\cos^2\alpha(1-2D\tan\alpha/L)$, where α is the tilt angle, D is height of tip, and L is length of the cantilever. The effective spring constant is typically 10 to 15% higher than the one calibrated using the aforementioned methods.

1.3 Current Mechanical Property of 1D Nanostructures Testing Methods

Due to their small dimensions, mechanical characterization of 1D nanostructures remains challenging. Several experimental techniques, as reviewed by Zhu *et al.* (Zhu, *et al.*, 2007) and Agrawal *et al.*(Agrawal and Espinosa, 2009)., have been developed and used to measure the mechanical properties of 1D nanostructures. These techniques include, but are not limited to the following: (i) axial tensile tests, (ii) electrically/magnetically driven resonant method, (iii) AFM-based methods, including (a) lateral force approach, (b) normal force approach, (c) Atomic Force Acoustic Microscopy (AFAM) based method and (d) AFM nanoindentation and (iv) nanoindentation using commercial nanoindenters. The techniques, including sample manipulation, working principle, pros and cons, are reviewed in the following sections.

1.3.1 Axial Tensile Test

A tensile test is one of the most traditional methods to measure material mechanical properties of bulk material. It has fully standardized testing procedures to determine Young's modulus, yield strength, which generally following the 0.2% offset

strain rule, tensile strength, and ultimate tensile strength of a substance. The failure pattern of tested material, ductile or brittle, can be observed during the experiment.

A tensile test has also been used to measure mechanical properties of 1D nanostructures. A successful axial tensile test on 1D nanostructures includes four main steps: (i) pick up a single nanostructure and properly align and fix the nanostructure in such a way that the load direction is along the axial direction of the nanostructure; (ii) accurately measure the force applied on the nanostructure; (iii) make precise diameter measurement and obtain cross section area of the nanostructure. Whether the cross section is rectangular, circular, elliptical, solid or tube-like will affect the cross section area, from which stress applied on the nanostructure will be calculated; and (iv) accurately calculate deformation of the nanostructure, strain under tensile load.

With a custom-made manipulator, Young's modulus of single NTs was measured inside a SEM (Yu, *et al.*, 1999, Yu, *et al.*, 2000). The whole setup is shown in Figure 1.2(A). The picking up and fixing NT to a test apparatus process were as follows: (1) Because of electrostatic attraction or Van der Waals forces between a NT and an AFM tip, one or several CNTs "jump" to the AFM tip when they were brought close to each other,; (2) A strong bonding of about 100 nm^2 in size was made using EBID to fix CNT on the tip of an AFM cantilever 1. The other end of the NT was attached to the tip of another AFM cantilever 2 using EBID. The cantilever 2 had a smaller spring constant compared to cantilever 1. The principle of applying force and measuring NT deformation, as illustrated in Figure 1.2 (B), is: as the top relative rigid cantilever 1 was driven up vertically, the deflection of bottom flexible cantilever 2 and length change of the NT were simultaneously captured by a series of SEM images. Given the deflection of the

AFM cantilever 2 and its calibrated spring constant, force applied on the NT was calculated. The strain of NT was determined from its length change from the recorded SEM images. The technique pioneered tensile tests for 1D nanostructures, however, a few aspects of the test can be improved: (1) it was difficult to align the NT with applied force to pure tensile stress with minimum bending stresses. (2) force and strain of the NT determination could suffer from image reading errors.

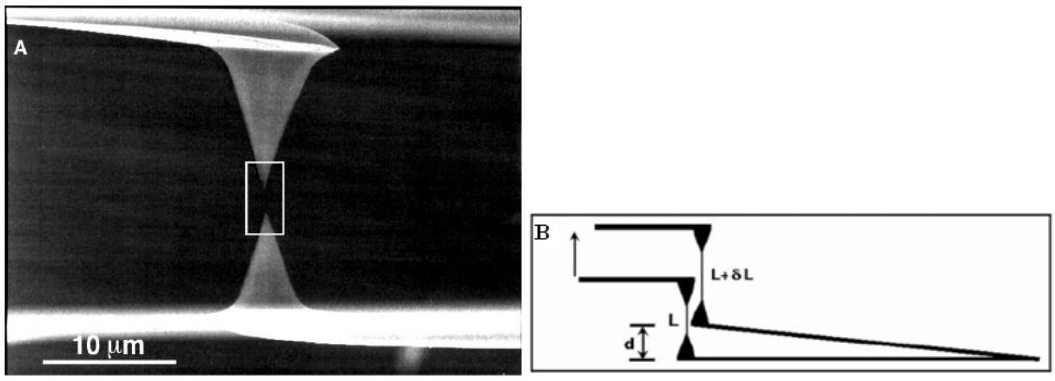

Figure 1.2: (A) SEM image of a NT tensile test setup; (B) schematic drawing shows the principle of a tensile test. When the top rigid cantilever 1 was driven upward, the lower cantilever bent upward by a distance *d*, while the NT was stretched from its initial length of *L* to *L*+δ*L* because of force exerted by the AFM tips. Force was calculated as *kd*, where *k* was the spring constant of the lower cantilever 2, and the strain of NT was δ*L*/*L* (Yu, *et al.*, 2000).

To make the pick-up and alignment process of a nanostructure easier, a sharp tungsten tip with a high aspect ratio fixed on a nanomanipulator (Klocke Nanotechnik, Germany) was used to pick up Si NWs (Zhu, *et al.*, 2009). The ultra sharp tungsten tip was better than an AFM tip in terms of pick-up of nanostructures, and was widely used in many kinds of nanomanipulators. One possible reason could be that charges accumulate on the sharp probe tip and make the electric field the stronger at the tip. As a result, the

force between a sharp tungsten tip and a nanostructure was larger than that between an AFM tip with a bigger aspect ratio and an nanostructure. The other end of the NW was fixed on the side of an AFM cantilever, which has a small spring constant of 0.70 ± 0.05 N/m. Fixing nanostructures on the side of an AFM cantilever was easier than putting them onto an AFM tip. However, this could introduce torsion of the cantilever, which the authors believed to have minor effect on the nanostructure's mechanical properties measurement. Similar to Yu's tensile test (Yu, *et al.*, 2000), force applied on the NW was calculated from cantilever deflection. Both cantilever deflection and NW elongation were determined from SEM images taken during the tensile test, which could induce some measurement uncertainties.

A tensile test of electrospun polyethylene oxide nanofibers with a diameter of around 700 nm was carried out (Tan, *et al.*, 2005). The pick-up and alignment process of the nanofibers were as follows: (1) a wood frame with strings was placed between two electrodes of an electrospinning device. Aligned nanofibers were deposited between the two strings of the wood frame and were further fixed to the coverslip with a masking tape. Tensile force were applied on the nanofibers and was measured by a piezoresistive AFM cantilever with a typical spring constant of 8 N/m, as shown in Figure 1.3. The piezo-resisitive cantilever had a resistive gauge integrated into its arm to sense its deflection. Force can be calculated from deflection of the cantilever and its spring constant. Nanofiber deformation and its diameter were measured by a CCD camera. The force resolution was ± 0.2 μN, and the displacement resolution was ± 0.2 μm. The set-up suffers from the complication of glass fiber and superglue used to attach the AFM cantilever to the nanofiber, lower displacement resolution and possible nanofiber dimension

measurement error under the CCD camera. Despite the shortcomings of the method, and the large diameter of the nanofiber here which is actually out of nano range, the setup was reviewed here to emphasize the importance of good sample alignment, and force measurement with a separate sensor, the piezo-resistive cantilever. However, different from the aforementioned tensile tests, the set-up uncoupled deformation of the cantilever and nanostructure, which could improve measurement accuracy.

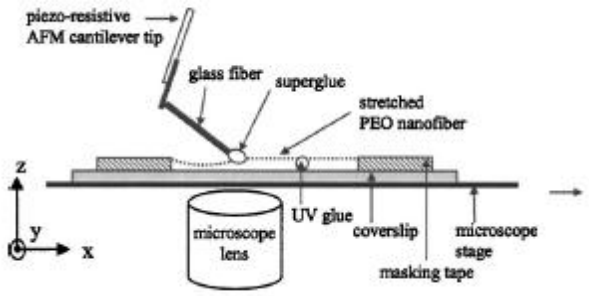

Figure 1.3: Set-up of a ensile test for nanofiber (Tan, *et al.*, 2005)

A Microelectromechanical/nanoelectromechanical system (MEMs/NEMs) (Espinosa, *et al.*, 2007, Zhang, *et al.*, 2010, Zhu and Espinosa, 2005) was also used to measure the mechanical properties of 1D nanostructures inside a Transmission Electron Microscope (TEM). The MEMs system included of three parts: a load sensor, a specimen holder to hold 1D nanostructures, and a thermal actuator, as shown in Figure 1.4 (from left to right). Pd NWs were manipulated onto the specimen holder following steps: (1) disperse Pd NWs in solution and put a few drops of solution onto a TEM grid; (2) pick up a single NW from the TEM grid using a nanomanipulator, and fix the NW to the nanomanipulator using EBID; (3) Move the NW-nanomanipulator assembly to the edges of the specimen holder and fix the free end of the NW to the specimen holder; (4) cut the

NW off from the nanomanipulator using a focused iron beam and fix the end of NW onto the other half of the specimen holder. The load on the NW was applied by the thermal actuator but measured by the separate load sensor, which is essential for a successful tensile test. The tensile test also has good strain measurement strategy. The strain of the NW was measured through length change between two marks generated by EBID, similar to use an extensometer to measure strain on macro-scale specimens. However, shortcomings of the test include: (i) Complication in device manufacturing and sample manipulation; (ii) challenge of load measurement. The load was related to a capacitance change with sub-fermto-Farad resolution, which was very challenging to measure.

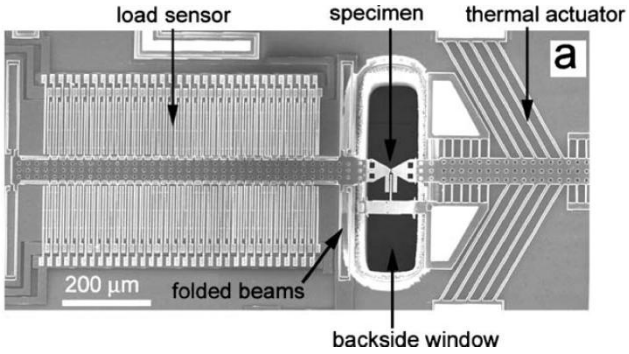

Figure 1.4: Setup of MEMs for 1D nanostructure tensile testing (Zhu and Espinosa, 2005)

In conjunction with a quantitative nanoindenter, a micromechanical device was proposed to perform uni-axial tensile testing on 1D nanostructures (Lu, *et al.*, 2010). The whole setup, shown in Figure 1.5, could be put inside a SEM or TEM. Force resolution of the nanoindenter is about a few tens of nN. Based on finite element simulations, Young's modulus of the tested nanostructures was extracted from measured load *vs.* nanoindenter displacement curve.

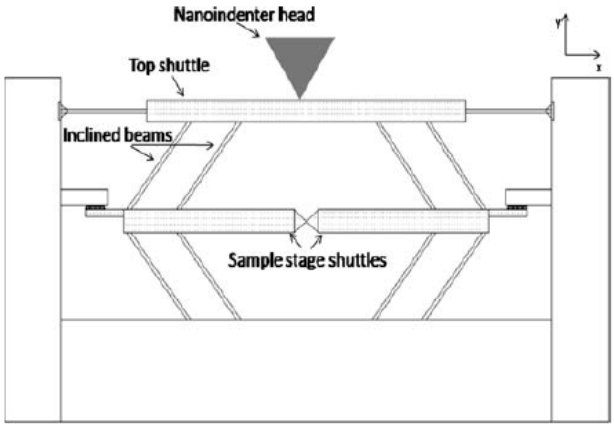

Figure 1.5: Schematic illustration of the microelectronic device. The device was driven by an in-situ nanoindenter. 1D nanostructures sit on the sample state shuttle (Lu, *et al.*, 2010).

Besides using a complicated device to apply force on a nanostructure and measure its mechanical properties, an easy way to apply tensile force on NWs inside TEM was proposed (Han, *et al.*, 2007). NWs were randomly distributed onto carbon supporting film on a TEM Cu grid. NWs found bridged on a broken part of the supporting film were identified for tensile testing. Irradiated by an electron beam, the supporting carbon thin film polymerized and shrunk 4 to 5%, stretched and applied load to the NW. Similar force using a force mediation polymer was used to selectively bend the NWs for strains up to 24% (Walavalkar, *et al.*, 2010). This loading method allowed for conducting atomic level structural investigation under tension inside a TEM. However, it is not clear how to fix a NW onto the carbon thin film. Load that applied on NW is not calibrated, neither. Additionally, the observed plastic like deformation of NW could be because of the metastability of NWs (Burki, *et al.*, 2005) under electron irradiation.

In summary, significant progress has been made in tensile tests of 1D nanostructures, from sample picking-up and aligning, to force applying and measuring, to

strain of a nanostructure measuring. Detailed lists of common procedures for different tensile tests are shown in Table 1.1. The highlighted methods are preferred when compared to other available methods. For sample picking-up and aligning, an ultra sharp probe is preferred to picking up nanostructures. Self-assembly is a better option for nanostructure alignment on a test apparatus. For force applying and measuring, a separate sensor measuring load applied on nanostructure has an advantage over cases where the cantilever serves as both sensor and actuator at same time, where displacement of a cantilever and a nanostructure are coupled with each other and special attention is needed for decoupling those two terms. Force measurement at micro and nano range remains challenging. Furthermore, the strain of a nanostructure is better calculated from a gauge length change, instead of a "Cross-head" deformation which measures the average deformation along nanostructure length. As to the tensile test used in reference (Han, *et al.*, 2007), the amount of load applied on nanostructures needs further investigation. Whether electron irradiation will alter deformation pattern of nanostructures is still debatable.

Table 1.1: Lists of common procedures for different tensile tests

References	Sample picking-up; aligning and fixing	Force applying and measuring	Strain measuring
(Zhu, *et al.*, 2009), (Yu, *et al.*, 1999, Yu, *et al.*, 2000)	AFM tip/ultra sharp tungsten probe to pick up sample and fix it using EBID.	One AFM cantilever to apply force. Deformation of the other cantilever is correlated to force.	SEM images, "cross-head" strain
(Tan, *et al.*, 2005)	Self-assembly nanostructure and fix it using a masking tape.	A piezoresistive cantilever to apply and measure force.	Optical images, "cross-head" strain
(Espinosa, *et al.*, 2007, Zhang, *et al.*, 2010, Zhu and Espinosa, 2005)	Ultra sharp tungsten probe to pick up sample and fix it using EBID.	A thermal actuator to apply force and a separate sensor to measure force.	SEM images; gage strain, gages defined by two marks generaged by EBID.
(Han, *et al.*, 2007)	Randomly distributed on a supporting film. No alignment	Irradiate electron beam on the supporting film to make it shrink and apply force	TEM images, "cross-head" strain

1.3.2 Electrically/Magnetically Driven Vibration

According to continuum mechanics, resonant frequency of either a one-end clamped or a both-ends clamped (clamped-clamped) beam is proportional to $\sqrt{E}$, where E is Young's modulus of the beam. 1D nanostructure was generally simplified as a continuum beam. As a result, given resonant frequency of the 1D nanostructures, their Young's modulus can be deduced. Young's modulus measurement of a nanostructure consists of three main steps: (1) manipulating the nanostructure; (2) exciting the nanostructure into resonance; and (3) detecting the vibration and determining its resonant frequency.

Poncharal *et al.*(Poncharal, *et al.*, 1999) electrically drove a NT/NW into vibration inside a TEM. The sample manipulation processes were as follows: (i) A fiber composed of carbon NTs was attached to a fine golden wire, which was mounted on a small electrically insulated support so that a potential could be applied; (ii) the assembly was inserted into a custom-built specimen holder, which was provided with a piezo-driven translational and rotational stages to accurately position the NTs relative to a counter electrode, as shown in Figure 1.6(A). NTs became electrically charged and one of them was attracted to the counter electrode when a static potential V_s was applied, as shown in Figure 1.6(B). After an AC voltage applied, the NT vibrated due to alternating attractive and repulsive force. By sweeping frequency of the AC voltage, and monitoring the vibration amplitude of NT based on TEM images, the resonant frequency that gave the maximum NT vibration amplitude was determined. Depending on the relative orientation of the NW to the counter electrode, the NW can either be axially excited (parametric vibration) or vertically excited (Chen, *et al.*, 2006). Failing to properly distinguish the two modes could lead to large deviation between a measured and the actual Young's modulus.

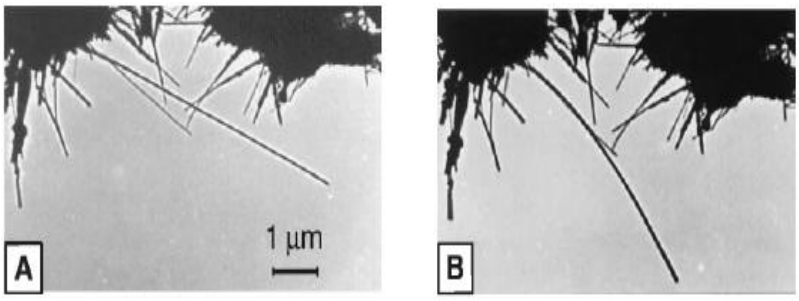

Figure 1.6: TEM image of an extruded NT. (A) an uncharged NT. (B) charged NT bending toward a counter electrode. The counter electrode at the bottom of the image was not shown (Poncharal, *et al.*, 1999).

Instead of using TEM/SEM images to determine whether 1D nanostructure was in resonance or not, Rao's group (Ciocan, *et al.*, 2005, Gaillard, *et al.*, 2005) designed a built-in integrated circuit to measure the resonant frequency of a cantilever NT. Basically, an ac voltage, V_{ac}, as well as a dc voltage, V_{dc}, induced charges on multiwall NT, and the electric force between charges residing on NT and counter electrode caused the NT to oscillate. The modulated charge on the NT was detected coherently using a lock-in amplifier set for the NT's 2^{nd} resonant frequency detection. The 2^{nd} resonant frequency was used because of the relatively small error (3%) in frequency estimation compared to the first order one (18%). The calculated bending modulus of NTs from their 2^{nd} resonant frequency was in excellent agreement with those reported in literature, which indicated that resonant frequency could be accurately measured using the integrated circuit.

In addition to excite NWs electrically, a magnetomotive technique (Tabib-Azar, *et al.*, 2005) was also used to excite nanostructures into resonance. NWs were grown laterally across a trench. When an NW was placed in an uniform magnetic field B and passed through an alternative current $I_D(t)$ perpendicular to the magnetic field, Lorentz force was generated on the NW and caused it to move perpendicular to $I_D(t)$ and B direction. The movement of NW through a magnetic field generated an electromotive force/voltage across two ends of the NW, which was measured with a network analyzer. By sweeping the frequency of the alternative current $I_D(t)$, the electromotive voltage spectra was obtained and frequency corresponding to maximum electromotive voltage was considered as the resonant frequency of the NW. The technique acquired NW resonant frequency using a circuit rather than depending on an image. Therefore, it can be conducted under ambient conditions instead of inside a SEM or a TEM. However, it

suffers from drawbacks of the following aspects: (1) it requires an intense magnetic field (0.4 T-1.2 T); (2) the *Q* factor of electromotive voltage spectra was small, which caused uncertainty in determining the resonant frequency of NW and (3) it only works for conducting NWs.

There are also other techniques to excite a NW into vibration and monitor its resonant frequency. A piezo-electric element was used to excite a Si NW directly grown across the trench of a Si die. Displacement of the nanostructure was detected using an interferometric method (Belov, *et al.*, 2008). When driving frequency of the piezo-electric element was the same as the resonant frequency of the Si NW, the motion of NW relative to bottom of the trench created a moving fringe pattern, from which NW resonant frequency could be determined. The technique does not require electrical contacts of NW to allow a current path through it, and it can detect vibration of multiple NWs simultaneously. However, the resolution of detecting displacement in 1D nanostructures using the interferometric method, is limited by diffraction of light as a general.

The above mentioned magnetomotive technique and piezo-electric exciting/ interferometric detecting method were applied for Si NEMS resonators characterization. Theoretically, any combination of exciting/displacement detecting methods for NEMS resonators hold promise for measuring the resonant frequency of 1D nanostructures which can be correlated to their Young's modulus. Most of the current available NEMS exciting and displacement detecting methods and their pros and cons are reviewed by Ekinci *et al.*(Ekinci and Roukes, 2005).

In summary, Young's modulus of nanostructures can be determined from their resonant frequency based on beam continuum mechanics. The main focus of these

techniques is determination resonant frequency of a nanostructure. Any technique which can detect resonant frequency of a nanostructure has the potential to obtain its modulus. Table 1.2 lists a few techniques, including their exciting and detecting methods, and pros and cons, used in measuring resonant frequency of a nanostructure.

Table 1.2: Techniques of measuring resonant frequency of a nanostructure

References	Exciting	Detecting	Pros	Cons
(Poncharal, *et al.*, 1999)	Electric force between a NT and a counter electrode	TEM images	Pioneered the technique	Obtain resonant frequency based on images
(Ciocan, *et al.*, 2005, Gaillard, *et al.*, 2005)	Same as above	Modulated charges on a NT	Overcomes cons of above	Challenge in measuring charge
(Tabib-Azar, *et al.*, 2005)	Lorentz force	Electromotive voltage across two ends of NW	Can be done in ambient condition	Intense magnet field; Small *Q*; NWs need be conduct
(Belov, *et al.*, 2008)	Piezo-electric element drove a NW and the supporting die	Light interferometry	Easy to drive NW into resonance	Detection limited by diffraction of light

1.3.3 AFM Based Methods

AFM has been widely used to study mechanical properties of 1D nanostructures (Li, *et al.*, 2010). The general principle of using an AFM to measure mechanical properties of 1D nanostructure is as follows: when an AFM cantilever is pressed against a tested nanostructure, force acting on nanostructure is given by $F = k_c S_N \Delta U_N$, where S_N is the sensitivity of the AFM photodiode and ΔU_N is the photodiode voltage change before and after the cantilever is pressed against the nanostructure. The system displacement *d*,

from deformation of both the cantilever and the nanostructure, is AFM scanner (or sample stage) extension depending on model of the AFM. The system stiffness of the cantilever and the nanostructure can be obtained from *F* and *d*. Furthermore, the stiffness due to deformation of the nanostructure alone can be extracted from the system stiffness. The mechanical property of the nanostructure can be extracted from its stiffness based on (i) the continuum beam bending theory (for lateral and normal force approach), (ii) the static Hertz contact (for AFM nanoindentation) and (iii) the dynamic contact (Atomic Force Acoustic Microscopy).

(i) Bending Tests

AFM bending tests were based on the continuum beam bending theory. For a continuum cantilever beam under load *F* at distance *x* from the clamped end, deflection at the load point is

$$d(x) = \frac{Fx^3}{3EI} \tag{1-1}$$

And Young's modulus of beam can be calculated by

$$E = \frac{kx^3}{3I} \tag{1-2}$$

where $d(x)$ is the beam deflection, I is its moment of inertia. $k = F/d(x)$ is its stiffness. Likewise, the deflection of a clamped-clamped beam is

$$d(x) = \frac{Fx^3(L-x)^3}{3EIL^3} \tag{1-3}$$

And its Young's modulus is

$$E = \frac{kx^3(L-x)^3}{3IL^3} \tag{1-4}$$

where L is length of the beam. For a simply-supported beam,

$$d(x) = \frac{Fx^2(L-x)^2}{3EIL} \tag{1-5}$$

And its Young's modulus is given by

$$E = \frac{kx^2(L-x)^2}{3IL} \tag{1-6}$$

The cantilever deflection also can be obtained for other boundary conditions, such as a clamped-simply-supported boundary condition.

It is generally accepted that the continuum beam bending theory can be extended to study mechanical properties of 1D nanostructures with cross section dimensions being larger than a few tens of nanometers. In other words, nanostructure Young's modulus can be calculated from the equation (1-2), (1-4) and (1-6) would a bending test *F-d* curve on nanostructure be available.

Depending on the direction of a force applied with respect to the axis of a nanostructure, bending tests can be further divided into two groups, as illustrated in Figure 1.7, (a) The lateral force approach, where force is perpendicular to the nanostructure and side of the AFM tip is in contact with the nanostructure; The AFM cantilever is under torsion and (b) The normal force approach, where the apex of the AFM tip is in contact with the nanostructure and the AFM cantilever is under bending.

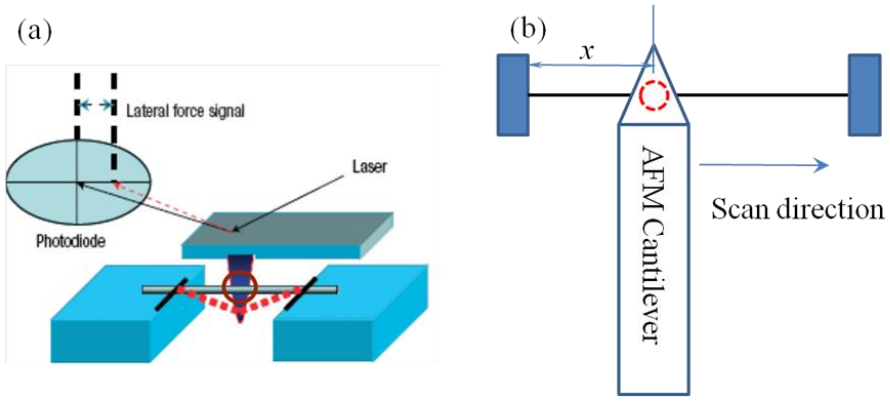

Figure 1.7: (a) Schematic illustration of a lateral bending (Wu, *et al.*, 2005) and (b) a normal bending using AFM.

(a) Lateral Force Approach

Wong *et al.* (Wong, *et al.*, 1997) pioneered the technique using an AFM lateral force mode to bend multi-walled carbon NTs (MWNTs) and SiC nanorods. 1-D nanostructures were randomly dispersed onto a substrate and selectively clamped down to substrate by the islands, the yellow part shown in Figure 1.8, which was fabricated with a conventional lithography method. As the AFM tip is scanned perpendicularly to the nanostructure under a lateral force of F=7.7 nN, deflection of the nanostructure $d(x)$ at a distance x from the clamped end was recorded by AFM images. According to the continuum beam model, Young's modulus of nanostructure was calculated from Eq. (1-2). This method could suffer from complications due to nanostructures-substrate friction. Furthermore, the effective bonding location of between the nanostructures and substrate could be uncertain due to possible leakage of the pinning materials in the shadow-mask process (Wu, *et al.*, 2005). The uncertainty would affect the x determination and Young's modulus of nanostructure as a result. On the other hand, $d(x)$ actually includes deflection of both the cantilever and the nanostructure. Ignoring deflection of the cantilever could lead to underestimation of the Young's modulus of a nanostructure.

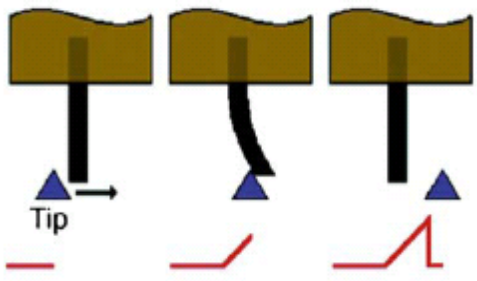

Figure 1.8: A schematic illustration of a one end clamped NT deflected by an AFM tip laterally (Wong, *et al.*, 1997)

To overcome the above mentioned complications due to nanostructures-substrate friction, Song *et al.* (Song, *et al.*, 2005) and Chueh *et al.* (Chueh, *et al.*, 2007) directly bent vertically grown ZnO and RuO_2 NWs by scanning across those nanostructures using an AFM tip with a 20° cone angle. Cantilevers had a normal spring constant of 4.5 N/m. As the tip scanned over the top of the NWs, force and deflection of NWs were determined from AFM images and modulus of the nanostructures was calculated similar to reference (Wong, *et al.*, 1997). This technique allows mechanical properties measurement of individual NWs of different lengths in an aligned array without any sample manipulation. However, as the authors pointed out, a disadvantage of the technique is its inaccuracy in evaluating the size of individual NWs. Another uncertainty for this technique is: the AFM tip could apply an eccentric force on the NWs and underestimate their Young's modulus. For a 45 nm ZnO NW, the measured elastic modulus was 29±8 GPa, which is far smaller than that of bulk ZnO.

Clamped-clamped nanostructures-over-trench configuration has also been used to study Young's modulus, yield strength and the strain hardening effect of Au (Wu, *et al.*, 2005), Ag (Wu, *et al.*, 2006) and Ge (Ngo, *et al.*, 2006) nanostructures under lateral bending approach. The experimental setup is shown in Figure 1.7 (a). The procedures of sample preparation were as follows: (1) the nanostructures were dispersed into solutions; (2) a few drops were put onto the substrate with trench and (3) A single nanostructure across the trench was located and the ends of the nanostructure were fixed to the edges of the trench using EBID. Rectangular cantilevers with average normal force constant of 20 to 40 N/m and 1 to 3 N/m were used. A Dimension 3100 AFM from DI instruments, equipped with a Nanoman software package and x-y closed loop control, was used to

conduct the lateral bending test. The lateral force *F vs.* displacement at mid-point of NW *d* was analyzed to determine its Young's modulus and yield strength. During data analysis, steps to obtain nanostructure modulus were: (i) calculate the spring constant of a combined nanostructure-AFM cantilever system $k_{obs} = \frac{F}{d}$. (ii) obtain spring constant of the nanostructure as $k_w = \frac{k_{obs} k_c}{k_c - k_{obs}}$, where k_c was the lateral bending spring constant, calibrated by lateral bend cantilever over edge of the trench. (iii) Young's modulus of NW was then calculated using Eq. 1.4 at $x=L/2$. Experimental results showed that yield strength of NWs was close to theoretical limit, whereas Young's modulus was diameter independent and closed to their bulk counterpart. As the authors pointed out, errors of this method stem from estimation of the NW and cantilever physical dimensions, AFM photodetector sensitivity and uncertainty due to lack of *z* closed-loop control. Without a *z* closed-loop control, AFM tip-nanostructure contact location, as illustrated in the green circle of Figure 1.7 (a), is unknown, which will cause uncertainty of the force on nanostructure estimation and Young's modulus measurement.

(b) Normal Force Approach

Normal force approach, as illustrated in Figure 1-7(b), applies a force on a nanostructure perpendicular to the surface supporting it. The dashed line red circle stands for AFM tip and AFM tip apex is in contact with the nanostructure. Depending on the operation mode of AFM, normal force approach is divided into two groups: (i) AFM cantilever scanned along the nanostructure at a constant load and (ii) AFM tip continuously pressed against the nanostructure at a fixed location *x*.

For the first group, orientation of the cantilever was perpendicular to the nanostructure and scan direction, as shown in Figure 1.7 (b). Two scans with a zero force and a constant force (F), respectively, along a nanostructure were conducted. Scanner extensions along the nanostructure at zero force (curve 1) and at the constant force (curve 2) were recorded. Scanner extension due to applied force $d(x)$ was obtained by subtracting curve 1 from curve 2. By doing this, the authors believed that possible initial slack of the nanostructure could be removed. Young's modulus was calculated from Eq. (1-2) (San Paulo, *et al.*, 2005, Silva, *et al.*, 2006) for one end clamped nanostructures and Eq. (1-4) for clamped-clamped nanostructures(Chen, *et al.*, 2006, Chen, *et al.*, 2007, Mai and Wang, 2006, San Paulo, *et al.*, 2005, Tabib-Azar, *et al.*, 2005).

The second group operated at the force mode of an AFM. Force applied on a nanostructure *vs.* extension of the scanner, a linear curve (curve i), was obtained at a distance x away from the fixed end. Force *vs.* extension of the scanner curve on an infinitely hard substrate (curve ii) was also acquired. Authors tried to eliminate deflection of the AFM cantilever and obtain the pure deformation of the nanostructure by subtracting curve i from curve ii. The force on nanostructure (F) *vs.* the nanostructure deflection curve was obtained. Young's modulus of nanostructures was calculated from Eq. (1-2) for one end clamped nanostructure (San Paulo, *et al.*, 2005, Xiong, *et al.*, 2006). A similar approach was used to study the mechanical property of a vertically grown silicon NW (Gordon, *et al.*, 2009). Note that force on the AFM tip and the nanostructure are same while their deflections are different during a measurement. Trying to eliminate deflection of the AFM cantilever by subtracting cantilever *F vs.* deflection curve from cantilever-on-nanostructure *F vs.* deflection curve is problematic. The method in

reference (Wu, *et al.*, 2005) is better in terms of eliminating deflection of the AFM cantilever and obtaining nanostructure modulus accurately.

For lateral or normal bending tests, knowing the correct boundary condition between a nanostructure and trench edge is critical in extracting the mechanical properties of 1D nanostructures from load *vs.* scanner extension curves (Chen, *et al.*, 2006, Chen, *et al.*, 2007, Mai and Wang, 2006). Figure 1.9 shows a comparison of experimental *vs.* model predicted deflection of a nanostructure under different boundary conditions (clamped-clamped Eq. (1.3), simply–supported Eq. (1.5), and one simply supported end with one fixed end) for silver NWs. While Figure 1.9 (a) and (b) confirmed that a clamped-clamped boundary condition described the nanostructure and edge of trench well, Figure 1.9 (c-e) indicated that a simple support boundary condition was more appropriate for those particular cases. As a result, simply assuming a clamped-clamped boundary condition for NW and edge of trench could underestimate Young's modulus of the nanostructure. To eliminate measurement uncertainty associated with unsure of boundary condition, experimental data was compared with model results using different boundary conditions, and the boundary condition gave a maximum match between experiment and model results was used to extract Young's modulus of the nanostructure.

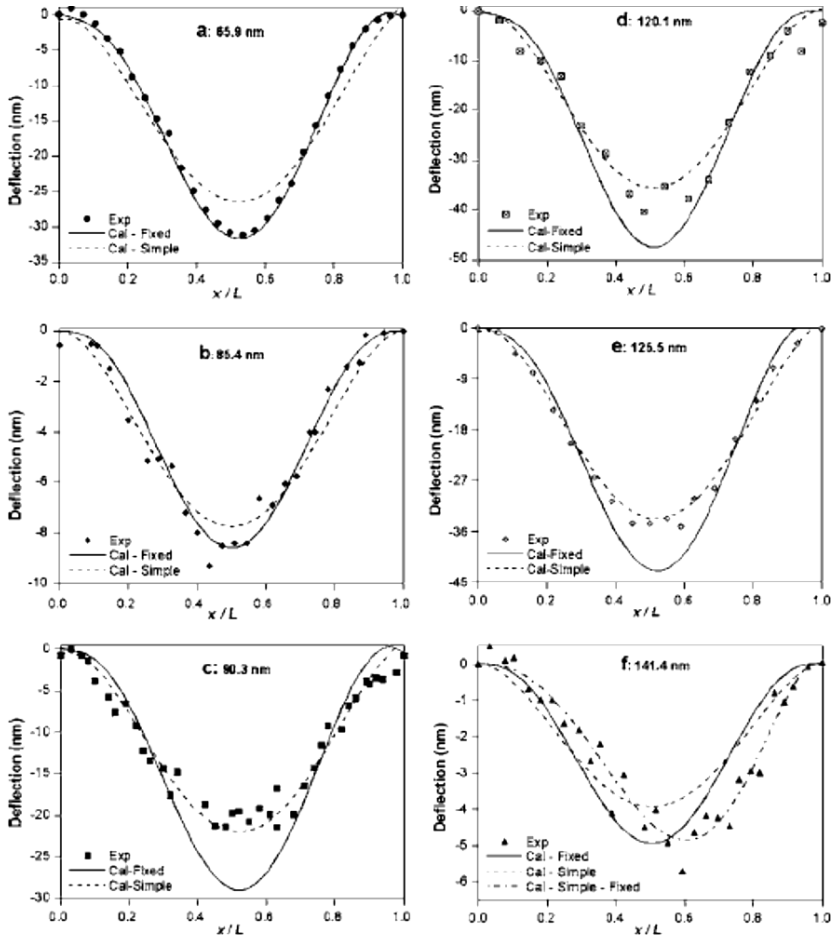

Figure 1.9: Comparison of experimental and model predicted deflections for silver NWs of different diameters (Chen, *et al.*, 2006)

Another issue in bending testing is the "swing effect"/slippage (Chen, *et al.*, 2006) of an AFM tip off the tested nanostructure, which typically happened in the normal force bending mode. If the AFM tip moves off axis of the nanostructures, it will apply an eccentric force on nanostructures and make them swing to the side. The slippage could introduce a substantial uncertainty of Young's modulus. To mitigate slippage effect on mechanical property measurement, AFM tip scanned along NW many times and the load-deflection profile gave the largest vertical component of the AFM cantilever deflection

was selected to extract Young's modulus of the nanostructure. Another approach to minimize slippage effect is using a special AFM cantilever tip, which was modified by a FIB milling process to produce a "tooth" shape groove with a dent width of 150 nm. The groove can secure the AFM tip on the nanostructure during the measurement process (Zhang, *et al.*, 2008).

The normal force bending test was also used to study the mechanical properties of graphene, a one-atom-thick carbon, as reviewed by Zhu *et al.* (Zhu, *et al.*, 2010). Graphene were suspended over a photolithographically defined circular holes etched with buffered hydrofluoric acid (Lee, *et al.*, 2008, Poot and van der Zant, 2008) or a trench of width between 0.5 μm and 5 μm (Frank, *et al.*, 2007, Gomez-Navarro, *et al.*, 2008). Suspended graphene were obtained by mechanically exfoliating kish graphite across trenches (Bunch, *et al.*, 2007). As the AFM tip being pushed against a suspended graphene sheet, force *vs.* extension of AFM scanner curve was obtained. The curve could give effective spring constant of the suspended graphene. Assuming graphene was clamped to the edge of circular hole or trench, Young's modulus of the graphene was extracted based on theory of a macroscopic plate (Poot and van der Zant, 2008) or a beam (Frank, *et al.*, 2007) bending under tension. A series of load and unloading curves on graphene matched each other well, which indicated that clamped boundary condition between graphene and the edge of trench was a valid assumption (Lee, *et al.*, 2008). Membrane theory was recently proved to be best in describing graphene's mechanical behavior. Young's modulus and fracture strength of graphene was measured to be 1.0 TPa and 130 GPa. For this kind of setup to measure mechanical property of graphene, Frank *et al.* emphasized that the spring constant of AFM cantilever should be comparable

to that of graphene sheets. Either too stiff or too flex cantilever could lead to inaccurate determination of graphene's mechanical properties.

(ii) AFM Nanoindentation

AFM nanoindentation test has been used to study mechanical property of polymer (Cappella and Silbernagl, 2008, Jee and Lee, 2010, Kovalev, *et al.*, 2004). The test is also used to measure mechanical properties of a nanostructure (Sohn, *et al.*, 2010) and its plastic deformation (Lucas, *et al.*, 2008, Lucas, *et al.*, 2007). The extraction of mechanical properties in a nanoindentation test was based on the Hertz contact theory, in contrast to the beam bending theory in bending tests. Sample preparation for nanoindentation test is simple compared to AFM bending tests, where only samples across trench are good for further testing. The sample preparation procedures for nanoindentation tests were as follows: (1) nanostructures were scraped from the substrate where they grew and dispersed into solutions through ultrasoincation; (2) a few drops of solution were placed onto a clean substrate and (3) an individual nanostructure was located through an AFM scanning for further testing. 2-spring-in series model (one for AFM cantilever and the other for contact interaction between the AFM tip and the nanostructure) was typically used to extract modulus of a nanostructure from *F-d* curve.

Like a thin film material, a nanostructure needs to be supported by a substrate. The substrate, used to support a nanostructure, will affect the *F-d* curve and the Young's modulus measurement. Recently, substrate effect on the Young's modulus measurement of a NB with AFM nanoindentation method was theoretically modeled (Zhang, 2010). In their model, a 3-spring-in-series model was used to model the indentation process. The model was based on the 2-spring-in-series model discussed above but with an extra

spring. The extra spring accounted for the nanostructure and substrate receding contact stiffness. In summary, due to the small dimension of nanostructures, the substrate effect, the extra spring, needs to be considered. Otherwise, extracted nanostructure modulus is error prone.

AFM nanoindentation test was not extensively adopted to study the mechanical property of 1D nanostructures. Reasons could be as follows: (1) the complicated theoretical model makes extracting nanostructures mechanical property non-trivial. (2) the parasitic lateral motion of the AFM tip during indentation (Huang, *et al.*, 2007) makes mechanical property measurement even harder. An AFM indentation test may result in unwanted lateral motion. The lateral motion makes indentation test on nanostructures with a circular cross section, such as NWs and NTs, almost impossible.

(iii) Atomic Force Acoustic Microscopy (AFAM) Based Method

AFAM based method is another technique to evaluate the near-surface mechanical property (Rabe, *et al.*, 2000, Rabe, *et al.*, 1996). This method has been used to study the mechanical property of ZnO NWs (Stan, *et al.*, 2007), Te NWs and faceted aluminum nitride NTs (Stan, *et al.*, 2009), SiO_2 NWs with a Si core (Stan, *et al.*, 2010). The method correlates the mechanical property of nanostructures to resonant frequency of the AFM cantilever while being pressed against a tested sample under a certain load. Sample preparation procedures for AFAM tests are similar to AFM nanoindentation: (1) disperse as-grown nanostructure into a solution; (2) put a few drops of solution onto a substrate; (3) locate an individual nanostructure and land the AFM tip onto it and (4) sweep driving frequency of the AFM cantilever and obtain its contact resonant frequency. A schematic illustration of AFAM setup to measure the cantilever resonant frequency is

shown in Figure 1.10. The detailed procedures to correlate the contact resonance frequencies with mechanical properties of the tested materials will be discussed in Chapter 2.

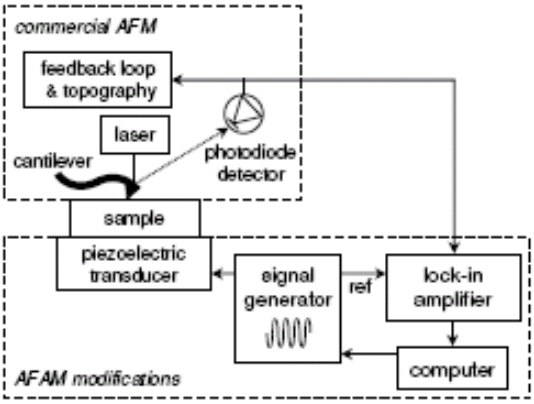

Figure 1.10: The schematic illustration of the experimental apparatus for AFAM based mechanical property testing method. (Hurley, *et al.*, 2007)

When conducting mechanical property tests on 1D nanostructures with AFAM, certain restrictions/requirements apply, which are listed as follows: (1) a closed-loop AFM scanner. Otherwise, indenting right on top of the nanostructures is challenging. A successful mechanical property test on a nanostructure with AFAM consists of two steps, i.e. (i) locating the nanostructure through AFM tapping mode scanning and (ii) withdrawing cantilever from the surface of nanostructure and re-engaging the cantilever under contact mode with a scan area of zero on top of the nanostructure. Most of AFM scanners now available on the market are made of PZT, which shows creep and hysteresis behavior. Without a proper feed-back (closed-loop) control to compensate the creep and hysteresis behavior, landing exactly on top of a nanostructure is ambitious. (2) the engagement of an AFM cantilever on the surface of a nanostructure must be gentle or

tip of the cantilever will be blunted because of the impact force during engaging. (3) this AFAM based method is improper for the nanostructures with high Young's modulus, since most of AFM tip on nanostructure system deformation will comes from the AFM tip. The technique is inapplicable for measuring materials with very low modulus, like biomaterials, neither. The contact stiffness between the AFM tip and a material of low modulus is so small that the contact resonant frequency of the AFM cantilever will be close to its free resonant frequency, no matter the cantilever is in contact with a soft material A or a soft material B. Therefore, materials A and B are indistinguishable.

(iv) Summary of AFM Related Measurement Techniques

AFM based techniques use the AFM cantilever as a force sensor to measure the load applied on nanostructures. The cantilever itself deflects while indenting or bending nanostructures. As a result, cantilever-on-nanostructure generally needs to be modeled with 2-spring-in-series system, *i.e.* a spring for cantilever itself (spring 1) and a spring for nanostructure bending/AFM tip indenting on nanostructure (spring 2). A properly chosen cantilever with suitable spring stiffness is important for all the AFM based techniques. Two extreme cases should generally be avoided: (1) spring stiffness of spring 1 is much lower than that of spring 2. System deformation for this case will be mainly from spring 1 so that the nanostructure would be like rigid comparing to cantilever. It is impossible for cantilever to distinguish one tested material from another; (2) spring stiffness of spring 1 is much larger than spring 2. The force resolution is low due to the small displacement of spring 1. An ideal case would be spring 1 and 2 having similar stiffness.

Among three AFM based techniques, bending test was most often used due to its simplicity in extracting nanostructure mechanical properties based on the beam bending

theory. Each technique has its advantages and limitations as shown in Table 1.3. Researchers should choose a proper technique to measure mechanical property of nanostructures, based on their AFM hardware capability and willingness to analyze complex interaction models between cantilever and nanostructure or not.

Table 1.3: Comparison of different AFM modes for 1D nanostructure mechanical test

Operation Mode		Pros	Cons
Bending	Lateral force mode	Extracting mechanical property is based on simple beam bending theory.	Difficult to calibrate the cantilever lateral spring constant; Depending on AFM hardware: The distance between cantilever tip apex and contact point between cantilever and nanostructure, which will affect applied torsion on nanostructure, is uncertain without a *Z*-closed loop control of AFM scanner.
	Normal force mode	Extracting mechanical property is based on simple beam bending theory.	Eccentric force could be applied on nanostructure and "swing effect"/slippage, making it hard to scan exactly on top of a nanostructure.
Nanoindentation		Straightforward for wide nanostructures, such as a NB.	Complicated in extracting mechanical property from contact model; Substrate effect, unwanted AFM tip lateral motion are hard to deal with.
AFAM		Contact resonant frequency of AFM cantilever can be accurately measured.	Depending on accurate AFM cantilever dynamic analysis, tip-sample contact modeling and AFM hardware.

1.3.4 Nanoindentation

Nanoindentation is another method to study mechanical properties of 1D nanostructures. Different from AFM based nanoindentation, where force sensor—AFM cantilever deflects itself during measurements, nanoindenter has a separate force and displacement sensor. It is widely used for material mechanical property characterization,

especially for bulk materials. Among many techniques used to characterize mechanical properties of nanostructures discussed so far, nanoindentation is attractive because (i) it is a relatively easy and quick testing technique; (ii) it can achieve excellent force resolution and control (better than 1.0 μN), and fine displacement resolution (better than 0.1 nm) (Oliver and Pharr, 1992); and (iii) it can provide a wealth of information regarding mechanical properties of a material. Both hardness and Young's modulus of the tested sample can be obtained from one single nanoindentation test.

The Hertz contact problem—an elastic half space indented by a rigid, axisymmetric indenter is the foundation of nanoindentation(Oliver and Pharr, 1992). Solutions for the elastic contact problem indicated that

$$P = \alpha h^m \tag{1-7}$$

Where P is the load applied on indenter and h is the indenter displacement into surface. α is a constant. m = 1.0 for flat-punch indenter; m = 1.5 for a spherical indenter and m = 2.0 for a conical indenter.

Berkovich, or cube corner indenter, is typically used for small scale nanoindentation tests. Because of sharpness of the indenter, plasticity is generally induced beneath the indenter, which makes analysis of load-displacement curve much more complicated. Analysis of nanoindentation load-displacement curves to obtain mechanical properties of a tested material is generally divided into two types: (1) forward analysis, where mechanical properties are fitted from the loading part of a load-displacement curve (Hainsworth, *et al.*, 1996, Jha, *et al.*, 2010); (2) backward analysis, where mechanical properties are extracted from unloading part of the load-displacement curve.

Forward analysis is initially studied for materials with considerable elastic recovery during unloading, such as very hard material and heterogeneous systems like hard coating on substrate system. The procedure to obtain the mechanical property of test material is: (1) Assume an indenter shape (equivalent conical indenter is assumed to approximate Berkovich indenter) and constitutive equation of the tested materials; (2) Fit load-displacement curve to the equation (Hainsworth, *et al.*, 1996)

$$P = E(\Phi_{\mathrm{m}}\sqrt{\frac{E}{H}} + \Psi_{\mathrm{m}}\sqrt{\frac{H}{E}})^{-2}h^2 \tag{1-8}$$

Where Φ_{m} and Ψ_{m} are indenter constants. (3) Given one of E and H, the other can be fitted from equation (1-8). Based on the procedures of obtaining mechanical properties, we see that disadvantages of the method are: (i) it is based on the assumption of an ideal indenter shape, such as a conical indenter which has a very sharp tip. However, the indenters used in most experiments are typically blunted especially after being used for a long time. The tip radius is around tens or even hundreds of nanometers. The minimum load for the assumption to be true is 1 mN, and (ii) the constitutive equation of materials could be very complicated. For example, fitting of equation (1-8) for a material showing strain hardening could be problematic.

Backward analysis, on the other hand, is a general practice of most nanoindentation data analysis and is adapted by commercial nanoindenters. Unloading part of the load-displacement curve, shown in Figure 1.11, is elastic, and the stiffness of the initial unloading part is given by (Oliver and Pharr, 1992):

$$S = \frac{dP}{dh} = \frac{2}{\sqrt{\pi}}E_r\sqrt{A} \tag{1-9}$$

$$H = \frac{P}{A} \tag{1-10}$$

where E_r is the reduced modulus. A is the projected area of the elastic contact between the nanoindenter and the tested material. H is the hardness of the tested material.

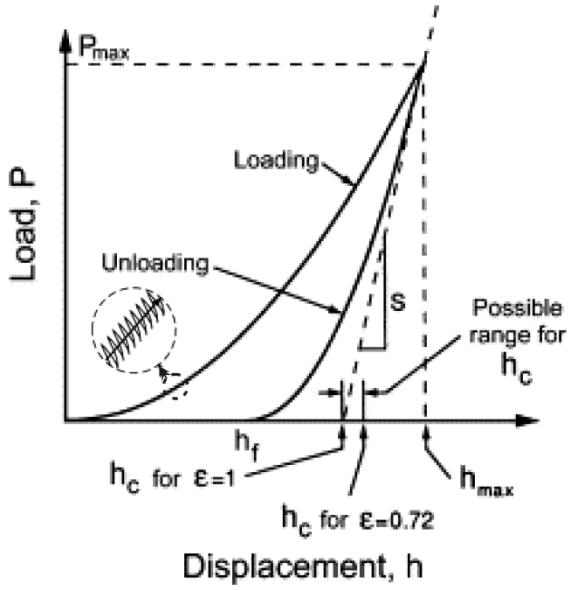

Figure 1.11: A typical load-displacement curve of nanoindentation result(Oliver and Pharr, 1992)

The equation (1-9) is based on solid theoretical modeling and extensive finite element simulations. The advantages of the backward analysis are: (1) It holds for any indenter geometry, such as spherical, conical and flat punch indenter. King confirmed that flat ended punches with square and triangular cross sections only deviate from the equation (1-9) by 1.2% and 3.4% respectively (King, 1987). (2) Given experimentally measured stiffness S and contact area A, E_r can be easily obtained. Furthermore, S and A can be accurately determined based on the methods outlined in the reference (Oliver and Pharr, 1992). The unloading part of load-displacement is typically fitted with a power law equation, and S can be obtained as derivative of the power law equation at the unloading

point. *A* is calibrated with a standard reference sample such as silica. The area function, which gives a correct modulus of a standard reference sample, is considered area function of the indenter.

One obvious disadvantage of back analysis is: it uses a standard reference sample to calibrate indenter area function *A*. Depending on the tested material yielding property, "pile-up" could happen for materials like aluminum and "sink-in" could happen for stiff materials. To correct the pile-up/sink-in caused uncertainty of contact area, Joslin and Oliver eliminated contact area from the equation (1-9) and (1-10) for elastic homogeneous system (Joslin and Oliver, 1990). They obtained the following

$$\frac{H}{{E_r}^2} = \frac{4}{\pi}\frac{P}{S^2} \quad \textbf{(}1\text{-}11)$$

P/S^2 is often plotted to check whether $\frac{H}{{E_r}^2}$ are constant. If either H or ${E_r}^2$ is known, the other can be determined from the above equation.

Even though nanoindentation was designed for studying the mechanical property of homogeneous bulk material, it has been extended to study Trabecular bone with porous structure (Gan, *et al.*, 2010) and mechanical properties of nanostructures, such as ZnO and SnO_2 semiconducting nanobelts (Mao, *et al.*, 2003), ZnS (Li, *et al.*, 2005, Yang, *et al.*, 2005), $Al_4B_2O_9$ and $Al_{18}B_4O_{33}$ NWs (Tao, *et al.*, 2007) and GaN and ZnO NWs (Feng, *et al.*, 2006), vanadium doped ZnO nanofibers (Chen, *et al.*, 2010), and Indium nano/microwires (Kumar and Kiran, 2010). It is worth pointing out that a few steps need to be carefully followed while indenting nanostructures: (1) Different from AFM based nanoindentation or AFAM method, the indenter used in nanoindentation is made of diamond, which is rigid compared to most tested materials. The indenter shape is persevered and thereby contact area is well determined throughout the indentation

process. The diamond indenter, however, could damage a nanostructure surface while scanning and locating a single nanostructure to perform an indentation test. It is critical to choose a proper scanning load to minimize damage to the nanostructure. (2) Similar to most of the AFM based methods, nanoindentation also depends on the hardware resolution while positioning the indenter on top of the tested nanostructures. The sample stage is mostly controlled by PZT materials, which show hysteresis effect. The effect could cause the target scanning area to be a little bit off the actual one. To make the target and actual areas overlap and indent exactly on top of a nanostructure, the offset should be manually compensated while choosing the scan area. (3) The tested nanostructures are expected to be reasonably smooth. Otherwise, there will be large uncertainty associated with the contact area between the nanostructure and the nanoindenter and thereby cause inaccurate measurement of nanostructures' mechanical property. (4) Due to the large force applied on the sample during indentation, the underline substrate effect could come into play, similar to a thin film on a substrate system. What the nanoindenter measured is actually an effective modulus of the nanostructure-on-substrate system. As a result, extracting the mechanical property of a tested material from the effective system modulus is critical for a nanoindentation test (Feng, *et al.*, 2006, Shu, *et al.*, 2009).

1.3.5 Other Techniques

The flow induced by a single laser-induced cavitation bubble was used to manipulate and measure Young's modulus of a single Co NW with a diameter of about 40 nm (Huang, *et al.*, 2010). The as-grown NWs were dispersed into ink and the solution was filled into a gap formed by two glass slides. A laser beam created cavitation bubbles inside the gap. During the bubble expansion and further collapse process, some of the

NWs near the bubble were bent by the force generated due to different velocity across their length. The dynamics of the NW was recorded with a high speed camera at a framing rate of up to 450,000 per second. By analyzing those images in conjunction with the hydrodynamic beam equation, Young's modulus of the NW was obtained. The obtained Young's modulus was only tenth of their bulk counterpart, which could possibly be due to low resolution of the high speed camera. Furthermore, improvement for both experiment and modeling is needed to make this method suitable for mechanical property measurement of a nanostructure.

1.4 Methods Used in This Dissertation

In reviewing the current available testing methods of 1D nanostructures' mechanical property, we noticed that tensile tests require a manipulator, either home-made or commercially available, to apply load and displacement to a nanostructure. Alignment of a nanostructure to make it under pure tension is challenging. Furthermore, obtaining the strain of a nanostructure from recorded SEM images could be problematic. On the other hand, the pros and cons of the techniques for obtaining Young's modulus from their dynamic resonant frequency are listed in Table 1.2. Measuring the resonant frequency of a modulated charge could be challenging too. Additionally, for AFM based nanostructure bending methods, the normal bending mode could suffer from nanostructure slippage and eccentric loading. Without an AFM closed loop control in *z*-direction, uncertainty of contact location between the side of an AFM tip and a nanostructure could lead to error in determining mechanical properties of nanostructures using the lateral bending mode.

With the pros and cons of each mechanical property testing methods and the hardware availability in mind, two methods are selected in current study: (1) AFAM based mechanical property measurement of nanostructures; (2) nanoindentation. Sample preparation processes for both methods are relatively easy: dispersing the as-grown nanostructures in a solution and dropping the solution onto a bare substrate. The individual nanostructures will then be located and chosen for further testing. For the AFAM based method, an AFM is used to conduct the test. After a single nanostructure is located, the AFM cantilever is pressed against the nanostructure and the cantilever contact resonant frequency is obtained. Nanostructure modulus is the extracted from the cantilever contact resonant frequency. For the nanoindentation method, a commercial nanoindenter is used to press against the nanostructure-on-substrate system. The nanostructure modulus is extracted from the load reacting on indenter *vs*. indenter displacement into the system curve

1.5 Dissertation Outline

This study of mechanical properties of 1D nanostructures consists of 6 chapters. This chapter covers motivations of the study and literature review of currently available testing methods of 1D nanostructures' mechanical property. The pros and cons of each method are reviewed. Two methods have been chosen for further study in this dissertation work considering hardware availability and ease of sample preparation. Chapter 2 presents a nanostructure mechanical property measurement using an atomic force acoustic microscopy. It covers the working principle of the methods, experiment setup, results/data analysis and discussion, whereas Chapters 3 through 5 focus on the mechanical property of a nanostructure measurement using a commercial nanoindenter.

Chapter 3 studies the mechanical property of TiO_2 nanoribbons, which have width-to-thickness ratios about 5. The nanoribbon has been laid on three different substrates. Our results indicated that sapphire is the best substrate for the nanoindentation test of these particular nanoribbons. A substrate selection rule for general nanostructure mechanical property test is presented for the first time. Chapter 4 studies the mechanical properties of divalent alkaline earth metal hexboride MB_6 nanostructures, which have a width-to-thickness ratios falling between 1 and 2. Chapter 5 provides a semi-analytical solution for the nanoindentation on a nanoribbon-on-substrate system. Chapter 6 summarizes studies in the present dissertation and postulates possible future works.

CHAPTER 2: MEASUREMENT OF MECHANICAL PROPERTY USING AN ATOMIC FORCE ACOUSTIC MICROSCOPY (AFAM)

2.1 Introduction

Atomic force microscopy has been widely used to measure the mechanical property of 1D nanostructures, as reviewed in Chapter 1. This chapter discusses one of those AFM based methods. The method is called the AFAM based method. It is used to study the Young's modulus of a BaB_6 nanostructure due to (1) its high force and displacement resolution, and (2) relative easiness in sample manipulation. While an AFM cantilever is in contact with a tested nanostructure, its *contact* resonance frequencies are different from its *free* resonance frequencies. The shift of the resonant frequency is correlated to the Young's modulus of the nanostructure. An add-in transducer to an AFM makes the cantilever resonant frequency measurement possible.

Section 2.2 presents the AFM cantilever dynamics and the working principle of using AFAM based method for mechanical property measurement of nanostructures. Section 2.3 includes the experimental setup of the AFAM based method and the detailed procedures to measure AFM cantilever contact resonant frequency. Section 2.4 focuses on results and data analysis and Section 2.5 discusses the method.

2.2 AFAM Based Method to Measure Mechanical Property

AFAM based method measures mechanical property of 1D nanostructures by indirectly measuring the AFM cantilever resonant frequency while it is pressed again a

tested 1D nanostructures. Cantilever dynamics and the formula for its contact resonant frequency are reviewed in this section.

2.2.1 Cantilever Dynamics

The AFM cantilever dynamics are highly nonlinear and remain challenging, as reviewed in by Raman *et al.* (Raman, *et al.*, 2008). Understanding the cantilever dynamics is important to make a full and good use of an AFM. Raman *et al.* pointed out that "…understanding these phenomena can offer deep insight into the physics of dynamic atomic force microscopy and provide exciting possibilities for achieving improved material contrast with gentle imaging force in the next generation of instruments…" (Raman, *et al.*, 2008). Here we review the AFM cantilever dynamics.

(a) Continuous Model of the Cantilever

AFM cantilever is generally described as a rectangular and homogeneous Euler beam. Its dynamics is captured by the Euler-Bernoulli equation. The equation for a beam with external forces applied at its free end is given by (Lozano and Garcia, 2009, Turner, *et al.*, 1997):

$$EI\frac{\partial^4 w(x,t)}{\partial x^4} + a_0\frac{\partial w(x,t)}{\partial t} + \rho ab\frac{\partial^2 w(x,t)}{\partial t^2} = \delta(x-L)(F_{exc}(t) + F_{t-s}(d)) \qquad (2\text{-}1)$$

E and ρ are Young's modulus and mass density of the cantilever material. a ,b and L are width, thickness and length of the cantilever, respectively. I is its moment of inertia; $w(x,t)$ is the time-dependent vertical displacement of the beam at a distance x away from the end that is fixed to the cantilever holder using a spring leaf. a_0 is the hydrodynamic damping coefficient. The generalized function $\delta(x)$ is infinity when x is zero and is zero otherwise. $\delta(x-L)$ accounts for the concentrated load applied at $x = L$. $F_{exc}(t)$ is

the excitation force applied to the cantilever and $F_{t-s}(d)$ is the AFM tip and tested sample interaction force. *d* is instantaneous tip apex-tested sample surface separation

$$d = z_c + w(L,t) \tag{2-2}$$

z_c is the initial tip apex-tested sample distance. The boundary conditions of the AFM cantilever are: one end of cantilever is fixed with zero displacement and rotation; the other end is momentum and shear stress free, *i.e*.

$$w(x,t)|_{x=0} = 0, \left.\frac{\partial w(x,t)}{\partial x}\right|_{x=0} = 0, \left.\frac{\partial^2 w(x,t)}{\partial x^2}\right|_{x=L} = 0, \left.\frac{\partial^3 w(x,t)}{\partial x^3}\right|_{x=L} = 0 \tag{2-3}$$

Substituting the *ansatz* $w(x,t) = X(x)T(t)$ into governing equation (2-1) and boundary conditions (2-3), cantilever displacement is expressed in terms of a series of eigenmodes

$$w(x,t) = \sum_{n=1}^{\infty} X_n(x)T_n(t) \tag{2-4}$$

Each mode is describes by (Rabe, *et al.*, 1996):

$$X_n(x) = \cos k_n x - \cosh k_n x - \frac{\cos k_n L + \cosh k_n L}{\sin k_n L + \sinh k_n L}(\sin k_n x - \sinh k_n x) \tag{2-5}$$

where $k_n L$ satisfies the equation $\cos k_n L \cosh k_n L + 1 = 0$. The deflection modes X_n are orthogonal. Based on dispersion relation $EIk^4 - \rho ab\omega^2 = 0$, Cantilever resonant frequency corresponding to k_n is given by:

$$\omega_n = \frac{(k_n L)^2}{{c_c}^2} \tag{2-6}$$

with $c_c = L\sqrt[4]{\frac{\rho ab}{EI}}$. Substituting *x* = *L* into equation (2-5), $z_n(t) = 2(-1)^n T_n(t)$ satisfy the following differential equation (Lozano and Garcia, 2008)

$$\ddot{z}_n(t) + \frac{\omega_n}{Q_n}\dot{z}_n(t) + \omega_n^2 z_n(t) = \frac{F_{exc}(t) + F_{t-s}(d)}{m},\ n=1,2,\ldots \tag{2-7}$$

With

$$\mathrm{Q_n} = \frac{\omega_n \rho \mathrm{bh}}{\mathrm{a_0}} \tag{2-8}$$

$$\mathrm{m} = 0.25\mathrm{m_c} \tag{2-9}$$

in which, m_c is the mass of the cantilever. The actual tip motion is given by

$$w(L,t) = \sum_{n=1}^{\infty} z_n(t)$$

For different deflection modes, the effective mass $m = 0.25\ m_c$ is same. Whereas resonant frequency ω_n is different, which indicates that the effective AFM cantilever spring constant of high-order deflection mode is higher than that of the first-order deflection k_c, where k_c is either calculated from cantilever dimensions or calibrated using methods summarized in Section 1.3.3. The aforementioned fact, different deflection mode having different spring constant, has implications on AFAM based mechanical property measurement. Force applied on a sample is large when the cantilever is under high-order resonance mode even though the average deflection is same as that of the first-order resonance mode.

(b) Q Factor of an AFM Cantilever Vibration

In a forced vibration, Q factor is a measurement of resonance sharpness. The Q factor is defined as

$$Q = \frac{\omega_0}{\omega_2 - \omega_1} = \frac{f_0}{f_2 - f_1}$$

where ω_0 is the resonant frequency of a vibration. The two frequencies ω_1, ω_2 are on either side of the resonant peak and correspond to a vibration amplitude of 0.707B, as shown in Figure 2.1. B is the maximum vibration amplitude when resonance occurs. *Q* factor, as defined above, represents damping of a vibration system. When an AFM

cantilever is in contact with a tested sample, the *Q* factor can be used to characterize the internal friction and plasticity onset of the tested sample (Caron and Arnold, 2009).

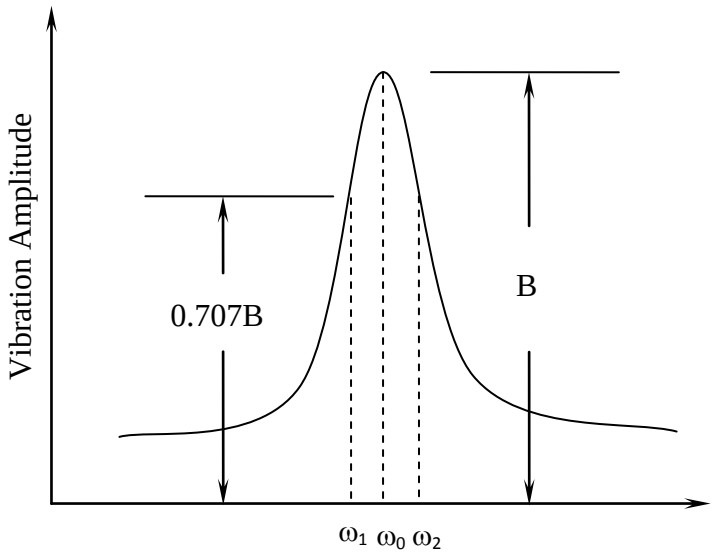

Figure 2.1: Schematic resonant spectrum of a forced vibration

2.2.2 Working Principle of AFAM Based Method

The AFAM based method for mechanical property measurement was pioneered by Rabe *et al.* (Rabe, *et al.*, 1996). Figure 2.2 illustrate the working principle of the method. The contact stiffness between the AFM tip and the tested sample modifies the dynamic of the cantilever. The contact resonance frequency falls between first and second resonant frequency of the cantilever. For an AFM tip with a hemispherical tip radius *R* is pushed against a tested bulk sample, based on Hertz contact mechanics, the contact stiffness between the AFM tip and the tested sample k^* is given by

$$k^* = \sqrt[3]{6E^{*2}RF_c} \tag{2-10}$$

where E^* is the reduced elastic modulus of the AFM tip-on-tested sample system, and is defined as

$$\frac{1}{E^*} = \frac{(1-{\nu_s}^2)}{E_s} + \frac{(1-{\nu_T}^2)}{E_T}$$

E_s, E_T, ν_s, ν_T are Young's modulus and Poisson's ratio of the tested sample and the material of the AFM tip, respectively. F_c is the load applied on the tested sample by the AFM cantilever.

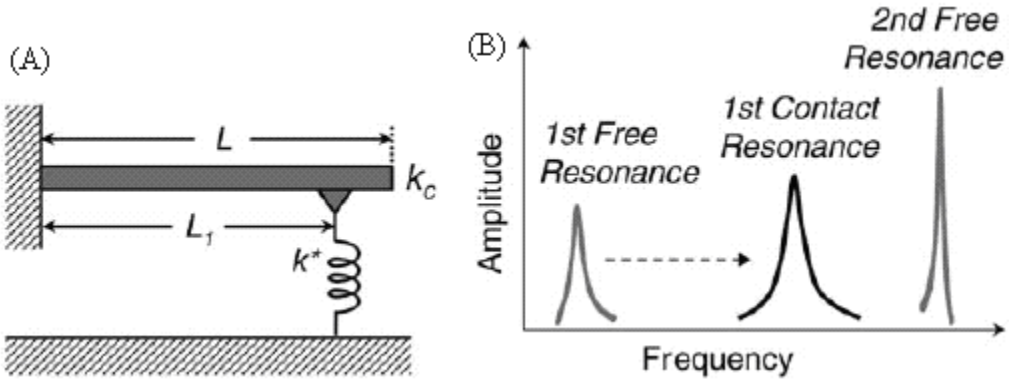

Figure 2.2: (A) A beam dynamics model for AFAM based method. A one-end clamped rectangular cantilever beam with a stiffness k_c was coupled to tested sample through a spring of stiffness k^* based on contact mechanic model. (B) Resonant spectra of an AFM cantilever. The first contact resonance calculated from the beam dynamic model shown in (A) was higher than first free resonance of the AFM cantilever but lower than its second free resonance (Hurley, *et al.*, 2007).

The contact stiffness between an AFM tip and a tested sample k^* generates a force between them and modifies the fourth boundary condition of the AFM cantilever, listed in (2-3), to

$$\left.\frac{\partial^3 w(x,t)}{\partial x^3}\right|_{x=L_1} = -k^* w(L_1, t) \qquad (2\text{-}11)$$

for a cantilever with a total length of L. L_1 is the tip location. L' is the distance between AFM tip and cantilever free end. Based on the method discussed in Section 2.2.1, k_n, wave number of the n^{th} AFM cantilever contact resonance, satisfies the following characteristic equation (Rabe, *et al.*, 1996):

$$\begin{aligned} &-(\cosh k_n L_1 \sin k_n L_1 - \sinh k_n L_1 \cos k_n L_1) \times (1 + \cos k_n L' \cosh k_n L') \\ &+(\cosh k_n L' \sin k_n L' - \sinh k_n L' \cos k_n L') \times (1 - \cos k_n L_1 \cosh k_n L_1) \\ &= 2\, {k_n}^3 \frac{EI}{k^*}(1 + \cos k_n(L_1 + L') \cosh k_n(L_1 + L')) \\ &= 2\, \frac{(k_n(L_1 + L'))^3 k_c}{3k^*}(1 + \cos k_n(L_1 + L') \cosh k_n(L_1 + L')) \end{aligned} \tag{2-12}$$

As discussed in Chapter 1, to make sure the AFM tip touches the tested sample surface first, AFM cantilever is usually tilted with respect to the tested sample at an angle α. A tangential spring constant κ between the AFM tip and the tested sample, in addition to the contact stiffness k^*, needs to be considered in the dynamic cantilever modeling. Assume that the AFM tip height is h, and the cantilever spring constant is k_c, the characteristic equation for the tilted cantilever in contact with the tested sample system is summarized as following (Hurley and Turner, 2007):

$$\frac{k^*}{k_c} = \frac{-B \pm \sqrt{B^2 - 4AC}}{6A} \tag{2-13}$$

where

$$A = \left(\frac{\kappa}{k^*}\right)\left(\frac{h}{L_1}\right)^2 (1 - \cos k_n L_1 \cosh k_n L_1) \times (1 + \cos k_n L' \cosh k_n L')$$

$$B = B_1 + B_2 + B_3$$

$$C = 2(k_n L_1)^4 (1 + \cos k_n L \cosh k_n L)$$

with

$$B_1 = \left(\frac{h}{L_1}\right)^2 (k_n L_1)^3 \left(\sin^2\alpha + \frac{\kappa}{k^*}\cos^2\alpha\right)$$
$$\times ((1 + \cos k_n L' \cosh k_n L')(\sin k_n L_1 \cosh k_n L_1 + \cos k_n L_1 \sinh k_n L_1)$$
$$- (1 - \cos k_n L_1 \cosh k_n L_1) \times (\sin k_n L' \cosh k_n L' + \cos k_n L' \sinh k_n L'))$$

$$B_2 = \left(\frac{h}{L_1}\right)(k_n L_1)^2 \left(\frac{\kappa}{k^*} - 1\right)\cos\alpha \sin\alpha\, ((1 + \cos k_n L' \cosh k_n L') \sin k_n L_1 \sinh k_n L_1$$
$$+ (1 - \cos k_n L_1 \cosh k_n L_1) \sin k_n L' \sinh k_n L')$$

$$B_3 = (k_n L_1)\left(\cos^2\alpha + \frac{\kappa}{k^*}\sin^2\alpha\right)$$
$$\times ((1 + \cos k_n L' \cosh k_n L')(\sin k_n L_1 \cosh k_n L_1 - \cos k_n L_1 \sinh k_n L_1)$$
$$- (1 - \cos k_n L_1 \cosh k_n L_1)(\sin k_n L' \cosh k_n L' - \cos k_n L' \sinh k_n L'))$$

In summary, k_n can be solved from either characteristic equation (2-12) or (2-13). Equation (2-13) is for a tilted cantilever. Furthermore, the contact resonance frequencies of a cantilever are obtained from the following dispersion relation (Rabe, *et al.*, 1996):

$$f_n = \frac{4\pi}{(k_n L)^2}\frac{L^2}{b}\sqrt{\frac{3\rho}{E}} \tag{2-14}$$

Whereas the free resonance frequencies of a cantilever ${f_n}^0$ are given by:

$${f_n}^0 = \frac{4\pi}{({k_n}^0 L)^2}\frac{L^2}{b}\sqrt{\frac{3\rho}{E}} \tag{2-15}$$

where ${k_n}^0 L$ are the solutions of $1 + \cos {k_n}^0 L \cosh {k_n}^0 L = 0$. Combing equation (2-14) and (2-15), the AFM cantilever contact resonant frequencies are given by

$$f_n = \left(\frac{k_n}{{k_n}^0}\right)^2 {f_n}^0 \tag{2-16}$$

The above equation circumvents the necessity to know density and Young's modulus of the cantilever.

For cantilevers with a tip being located at end of the AFM cantilever, i.e. $L'=0$, k_nL was solved from equation (2-12) for different k^*/k_c, which were listed in Table 2.1. Substituting k_nL values in Table 2.1 into equation (2-16), AFM cantilever contact resonant frequency and its free resonant frequency ratios were obtained, as listed in Table 2.2. From the Table, several important conclusions can be drawn: (1) For the first-order cantilever deflection mode, contact resonance is insensitive to k^* when $k^*/k_c<1$ or $k^*/k_c>100$. In other words, changing of k^* in those two zones does not significantly alters the cantilever contact resonant frequency. As a result, AFAM based method in ineffective to mechanical properties of a tested material in the two zones. (2) For higher-order deflection modes, such as $n=4$, contact resonant frequency is sensitive to k^* only when $k^*/k_c>100$, which indicates that high deflection mode should be used for materials with high modulus. However, it is worth pointing out that the effective high-order spring constant k_{nc} is higher than k_c, as discussed in Section 2.2.1. Contact load F_c on tested material and k^* as a result will be larger for high-order resonance of the cantilever.

Table 2.1: Solutions of k_nL from equation (2-12) (Rabe, *et al.*, 1996). Some spaces are left empty because the difference between contact and free end case is less than 0.001.

n	Free end k*=0	$k^*/k_c=0.1$	$k^*/k_c=1$	$k^*/k_c=10$	$k^*/k_c=100$	Pinned end k*=∞
1	1.8751	1.91891	2.2135	3.16765	3.82981	3.9266
2	4.69409	4.69699	4.7234	5.00112	6.40415	7.06858
3	7.85476	7.85538	7.86097	7.91896	8.58742	10.2102
4	10.9955	10.9958	10.9978	11.0185	11.2559	13.3518
5	14.1372	14.1373	14.1382	14.1479	14.2523	16.4934
6	17.2788		17.2793	17.2846	17.3396	19.635
7	20.4205			20.4239	20.4567	22.7765

Table 2.2: Frequency ratio f_n/f_n^0 for different deflection modes of a cantilever

n	f_n/f_n^0				
	k^*/k_c=0.1	k^*/k_c=1	k^*/k_c=10	k^*/k_c=100	Pinned end k*=∞
1	1.047274	1.39351	2.853813	4.1716282	4.385150033
2	1.001236	1.012527	1.135094	1.8613162	2.267574325
3	1.000158	1.001582	1.016414	1.1952522	1.689672978
4	1.000055	1.000418	1.004188	1.0479257	1.474516616

With a known contact stiffness between an AFM tip and a tested material, AFM cantilever contact resonant frequency will be determined. Vice versa, given the contact resonant frequency of an AFM cantilever, the contact stiffness between the AFM tip and a tested material can be determined. So is Young's modulus of tested material. The general procedures to extract mechanical property from contact resonant frequency are as follows: (1) Experimentally measure contact resonant frequency f_n, n = 1 case is often used; (2) Obtain k_n from equation (2-16); (3) Calculate k^* from equation (2-12) or (2-13) when AFM cantilever tilting is considered; and (4) Substitute k^* into equation (2-10) and obtain tested material Young's modulus assuming Poisson's ratio is close to bulk material value considering that variation of Poisson's ratio has minor effect on simulated load vs. displacement curve (Chen and Vlassak, 2001). Due to the difficulty of directly measuring the tip radius, a reference sample is generally used to circumvent the necessity of measuring AFM tip radius *R*, which will be discussed in a later section.

2.3 Experimental Setup

To measure mechanical property of 1D nanostructures, the nanostructures was deposited on a substrate. The AFAM based method is for a single nanostructure, instead of bundled nanostructures. The sample preparation procedure was as follows: (i) the as-

grown nanostructures were scraped from the substrate where they were grown, and dispersed into a solution through ultrasonication. (ii) A few drops of solution were dropped onto a clean substrate. After the solution was evaporated, some isolated nanostructures were left on the substrate. (iii) A individual nanostructure was then located and further tested.

Two types of methods were tried to excite an AFM cantilever into resonance: (1) directly excite the PZT inside the AFM cantilever holder. The external PZT driving signal was connected to the AFM Signal Access Module (SAM). (2) put tested nanostructure-on-substrate system onto a piezoelectric transducer at ultrasonic frequencies (V106-RM, 2.25 MHz, 0.50’ element diameter, Panametrics). SWC (shear wave couplant, Olympus Inspection and Measurement System) was used to transmit an acoustic wave from the transducer surface to the substrate, and then the nanostructure, and AFM cantilever. The nanostructure-on-substrate on transducer system preparing processes were as follows: (i) clean the piezoelectric transducer surface with alcohol using a cotton swab; (ii) scrape a bit of TWC couplant, put it onto the transducer surface, and the bit was flatten with a sharp knife edge to form a thin layer of couplant on the transducer surface; (iii) lay the substrate, with nanostructure deposited on its top surface, onto the thin layer of couplant and press the substrate at its corners against the transducer surface with tweezers. By carefully following these steps, the acoustic wave can be effectively transmitted to the nanostructure, and then AFM cantilever. Glycerin was also tried as a couplant. However, it quickly spread onto the top surface of substrate where the nanostructures were deposited. To eliminate the possible adverse effect on mechanical property measurement of a nanostructure, glycerin was abandoned for further usage.

Comparing the two aforementioned cantilever excitation methods, the first one directly excites the PZT inside cantilever holder. No extra component is required. However, the obtained contact frequency spectrum was quite noisy. Many resonant peaks, beside the cantilever contact resonance peak, were found in the spectrum. Factors, such as resonant frequency of the part where cantilever was connected, cantilever itself and insecure bond between PZT and other adjacent components, could be the reasons for those extra peaks. Properly picking the right cantilever contact resonant frequency from the noisy spectrum was challenging. As a result, the second type of excitation method was used throughout the experiment. A clean cantilever frequency spectrum could be easily obtained.

Different cantilevers with a variety of free resonant frequencies (from 100 KHz to 400 KHz), and wide spring constant range (between a few to 40 N/m) were tried. A sharp and distinctive resonant frequency spectrum could be easily obtained using commercial silicon cantilevers (PPP-SEIH, Nanosensors). The cantilevers were chosen for further study as a result. The nominal thickness, length and width of those cantilevers were 5.0±1.0, 225±10 and 33±8 μm, respectively. The spring constant of each cantilever was individually calibrated by the manufacturer. They were between 8 and 12 N/m. The free resonant frequency of a cantilever was about 130 KHz. The cantilever contact resonant frequency was about 4 times of its free resonant frequency.

A schematic diagram of the experimental setup of AFAM is shown in Figure 2.3. A function generator drives the piezoelectric transducer, which stays on the AFM sample stage, with a sinusoidal sine wave ($\sin\omega t$). The wave is subsequently transmitted to the substrate supporting 1D nanostructures, the nanostructure, and the AFM cantilever

pressed against the nanostructure. The same sinusoidal sine wave is also served as a reference signal to a lock-in amplifier (SR844 RF, Stanford Research Systems). The AFM cantilever deflection signal, accessed through the AFM Signal Access Module (SAM), is input into the lock-in amplifier, as illustrated in Figure 2.4. The $\sin\omega t$ component of the cantilever deflection is measured by the lock-in amplifier using a LabVIEW (National Instruments) program, as shown in Figure 2.5. By sweeping the driving frequency ω to the function generator, the cantilever spectrum while in contacting with the tested nanostructure, amplitude vs. driving frequency, is obtained. The frequency gives the maximum vibration amplitude is the contact resonant frequency of the cantilever at the load F_c.

An AFM (Dimension 3100, Veeco Instruments Inc.) in Optical Center of UNC Charlotte was used to conduct AFAM based nanostructure mechanical property measurement. The X-Y scanner scan range (~90 μm) is much larger than a multimode SPM, which has been generally used in an AFAM based method to measure material properties of those small-scale structures (Stan, *et al.*, 2007). The larger scan range requires extra noise dampening precautions at small-scale scans. This could be the reason for less accurate in software controlling. The larger scanner could also cause issues while landing an AFM tip right on top of a nanostructure. Equipped with a Signal Access Module (SAM), the AFM can take external driving signals to control the PZT insider the cantilever holder. The signal then excites the AFM cantilever, whose deflection signal can also be accessed through the SAM, an essential component for any AFAM based testing. The AFM also has NANOMAN software installed. The software enables user to switch between a tapping mode (for surface scanning to locate an interesting area) and a

contact mode (for local oxidation) while the AFM tip is engaged on a surface. This capacity makes the AFAM based measurement method feasible for nanostructure mechanical property measurement even with the large scanning range scanner. The general procedures to measure the contact resonant frequency of an AFM cantilever are as follows:

(1) Entering NANOMAN workspace;

(2) Setting the tapping mode scanning parameters, such as scan area, set point driving amplitude *etc*; Tuning the cantilever and recording its free resonant frequency; Setting the contact mode parameters, such as set point voltage, which determines applied load on a tested sample for the subsequent AFAM based mechanical property testing. The scan area for contact mode is set as zero. Correctly setting the contact mode parameters is extremely important. Wrong parameters could cause the AFM tip blunting during the cantilever engaging process.

(3) Scanning and locating a single nanostructure under tapping mode. Zooming in and trying to capture an image with minimum size but still be able to capture cross-sectional profile of the nanostructure. The center of AFM scanning is set as the target testing location.

(4) Switching to contact mode of the AFM and the AFM tip will land on the center of scanned image/targeted testing location.

(5) Sweeping driving frequency of the input signal to the transducer, and obtaining cantilever contact frequency spectrum. The cantilever contact resonant frequency is determined from the spectrum.

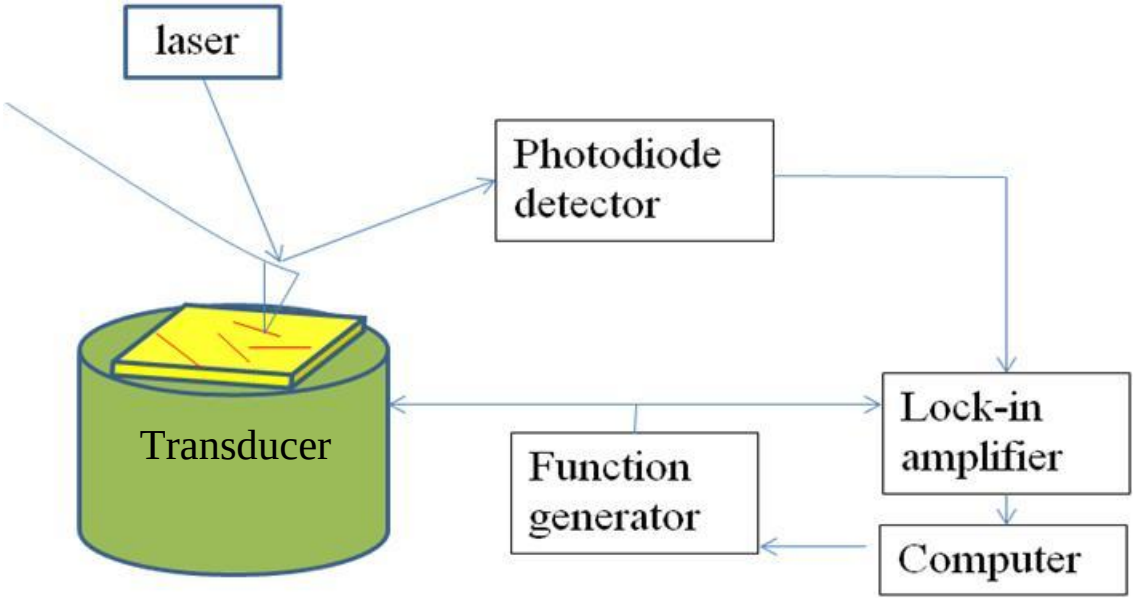

Figure 2.3: Schematic illustration of an AFAM setup for measuring AFM cantilever resonant frequency

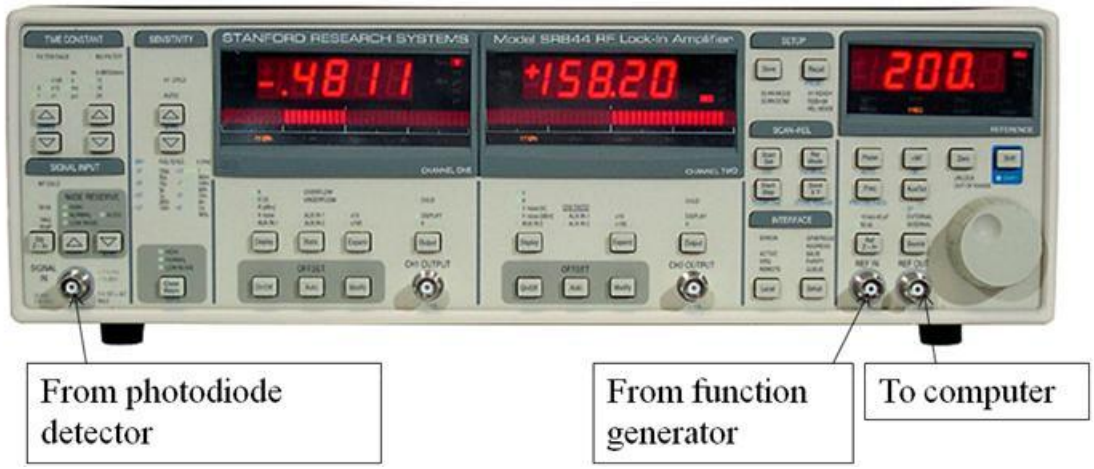

Figure 2.4: Signal in and out from a lock-in amplifier

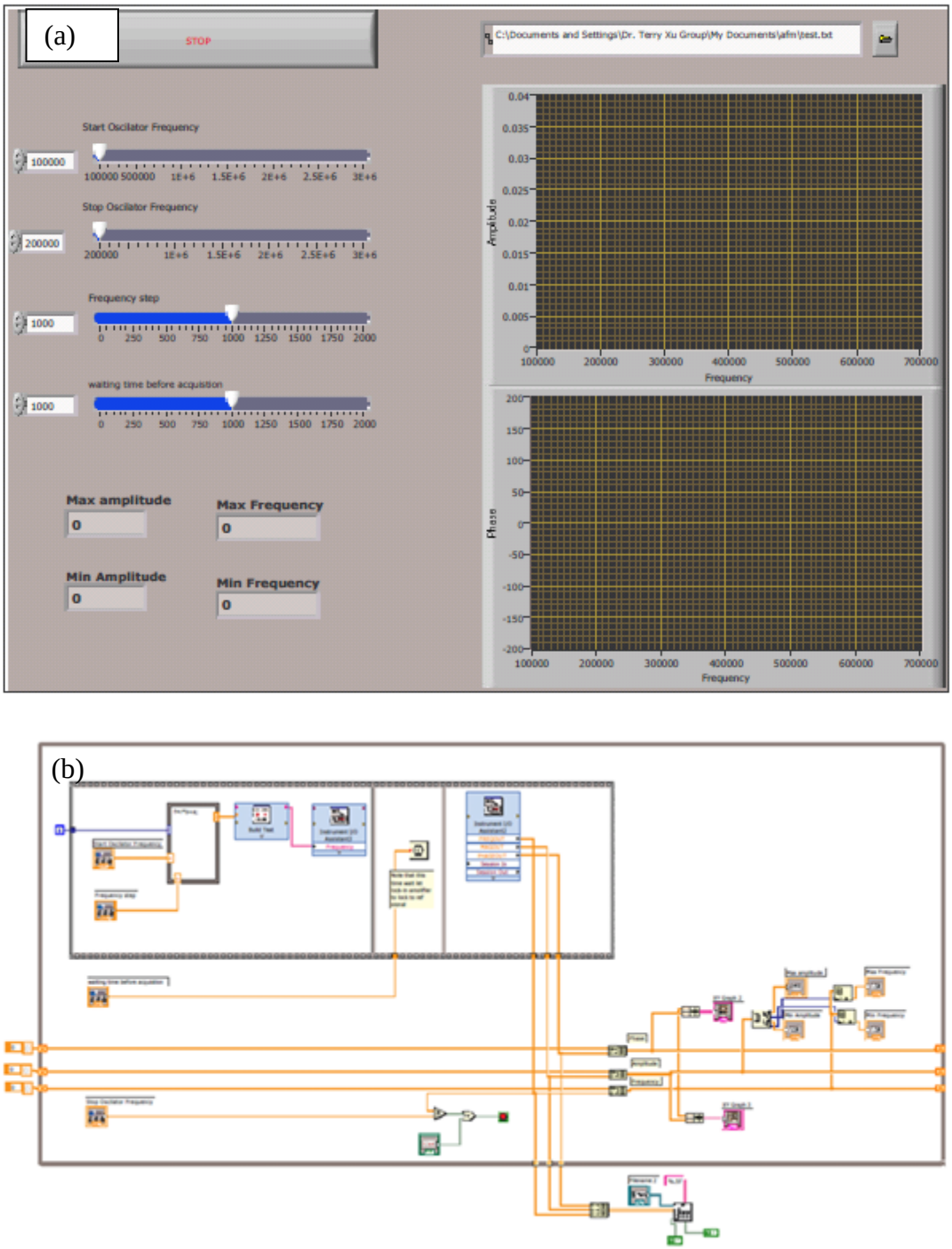

Figure 2.5: Screen shot of the LabVIEW program, (a) Front panel and (b) block diagram, used to measure the AFM cantilever contact resonant frequency

2.4 Results and Discussion

Using the procedures listed in Section 2.3, contact resonance frequencies of three cantilevers while contacting a single BaB_6 nanostructure-on-substrate system, and a Si substrate with 1 μm thick SiO_2 layer on top(SiO_2/Si) were measured. The frequencies on the system and SiO_2 on Si are listed in Table 2.3.

As discussed in Section 2.2, wave number k_n of an AFM cantilever, while contacting with a tested sample, is related to contact resonant frequency of the cantilever, see equation (2-14) or (2-16). The AFM tip–tested sample contact stiffness k^*can be calculated from k_n based on cantilever dynamics, see equation (2-12) or (2-13). Young's modulus of the tested sample will be extracted from k^* based on equation (2-10). The AFM tip worn out makes tip radius determination tricky. To avoid measuring the AFM tip apex radius, cantilever contact resonant frequency was also measured on a reference material, SiO_2/Si. Assume the AFM tip apex radius are same during the tests on the reference material and the system, and with a same applied load F_c, the ratio of equation (2-10) for the test system over that for reference material is

$$E_s{}^* = E_R{}^* \left(\frac{k_s{}^*}{k_R{}^*}\right) \tag{2-17}$$

where subscript S and R stands for the tested system and the reference material, respectively. Assume Young's modulus and Poisson's ratio of SiO_2/Si is 70 GPa and 0.3, respectively, and Young's modulus and Poisson's ratio of AFM tip material are 150 GPa and 0.17. The extracted Young's modulus of the tested BaB_6 nanostructure was listed in the last column of Table 2.3. The above procedure is a general practice in AFAM based mechanical property measurement, as adopted by some researchers (Stan, *et al.*, 2009).

Table 2.3: AFM cantilever contact resonant frequency on SiO_2/Si and nanostructures

Cantilever	Contact resonant frequency on SiO_2/Si (KHz)	Contact resonance frequency on NW(KHz)	Calculated Young's modulus of a BaB_6 nanostructure (GPa)
1	474	497	131.68
2	486	509	132.09
3	470	489	121.96

The obtained Young's modulus of the BaB_6 nanostructure is significantly lower than that of bulk BaB_6 materials (Kosolapova, 1990) and that measured using nanoindentation (as listed in Chapter 4). The discrepancy could be due to the following reasons:

1. AFM tip shape uncertainty: with a non-wearable AFM tip, the Young's modulus of tested material has a well defined relationship with AFM tip – tested material contact stiffness according to Equation (2-10). However, we noticed that the AFM tip continuously worn throughout the experiment. The AFM tips were examined inside a SEM before and after each contact resonant frequency measurement. Figure 2.6 shows SEM images of a typical worn tip and a new AFM tip. The tip wearing can also be inferred by the contact resonant frequency shift on one material before and after an experiment on glass (Hurley and Turner, 2007). The evolving of silicon AFM tip geometry during experiment has been found by previous researchers. Kopycinska-Muller, Geiss *et al.* (Kopycinska-Muller, *et al.*, 2006) conducted contact resonance spectroscopy measurements using ten AFM cantilevers. They found that neither punch nor hemisphere shape could successfully represent the shape of those AFM tips. Instead, the measured contact resonance frequencies

were successfully correlated to mechanical properties assuming contact stiffness and applied load on a tested sample satisfied an equation $k^* = \beta F_c^n$, where β is a factor depending on tip geometry and elastic properties of the tip and tested sample. *n* varies from 0 for a flat punch to 1/3 for a spherical indenter. Continuing tip blunting during experiment caused tremendous uncertainty of the measurements.

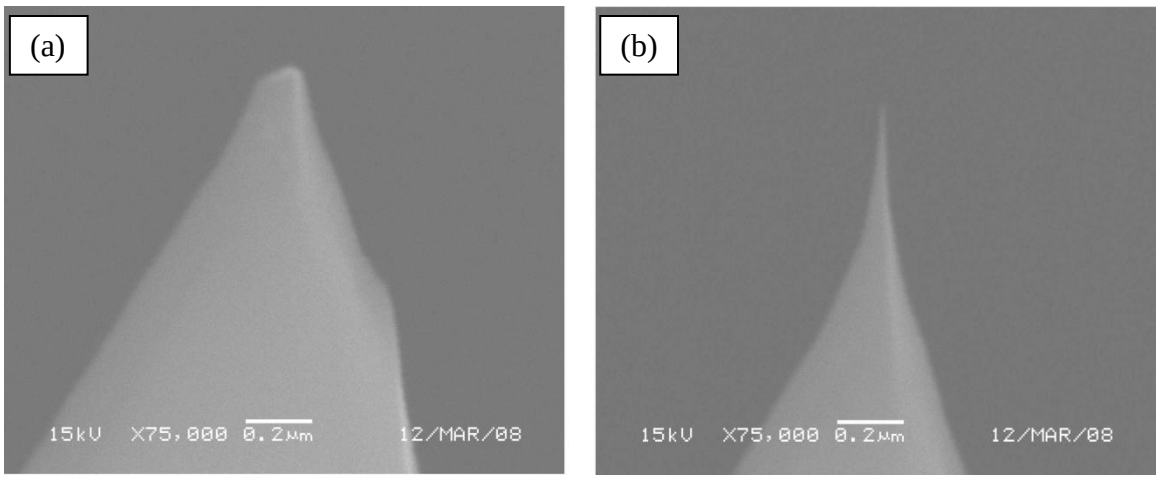

Figure 2.6: SEM images of (a) a typical worn tip, and (b) a new AFM tip

2. While the silicon AFM tip is contacted with materials of high modulus, like TiO_2 or MB_6 nanostructures, most of the deformation of an AFM tip-on-nanostructure system comes from the AFM tip. It could cause: (1) continuing blunting of the AFM tip; (2)the AFM cantilever contact resonant frequency actually being correlated to silicon modulus, while irrelevant to the properties of the tested materials, i.e. the AFAM based method can't be used to measure

mechanical properties of materials with high modulus. A diamond indenter should be used to measure their mechanical properties.

3. The tested BaB_6 nanostructures typically have oxidation layers, which will be discussed in Chapter 4. Moreover, a gentle load, 120 nN, was applied on the nanostructure by the AFM cantilever. The load induced deformation of the nanostructure could be confined in the oxidation layer. The measured modulus listed in Table 2.3 is slightly bigger than the Young's modulus of BaO calculated using first-principle (Ghebouli, *et al*.). The calculated Young's modulus at zero pressure is 104.51 GPa. In other words, the measured modulus could be modulus of the oxidation layer.
4. AFAM based method depends on the AFM hardware capability. Even though the AFM used is equipped with Nanoman software, which enables the AFM to switch between tapping mode and contact mode while the cantilever is engaged on a tested sample. The scanner in our AFM system is designed for large area scanning, which makes landing exactly on top of a nanostructure challenging. The inability to land at the target area and stay there during the whole testing process makes the tested results error prone.
5. In the aforementioned data analysis procedure, the AFM tip modulus was assumed to be same as their bulk counterparts. However, the two could be different due to the small radius of the AFM tip. Method using a second reference material to avoid the assumption has been introduced by Stan and Price (Stan and Price, 2006). The method improves the accuracy of the measured modulus of nanostructures.

2.5 Discussions

Mechanical property measurement of a 1D nanostructure using an AFAM was reviewed. Three tests on a 1D BaB_6 nanostructure were conducted and the nanostructure Young's moduli were analyzed. The obtained Young's modulus of the nanostructure is significantly lower than that measured by nanoindentation. Possible reasons to cause this discrepancy were discussed. As a conclusion, the AFAM based method is improper for measuring mechanical property of BaB_6 nanostructures due to (1) significant AFM tip blunting during the measurement, (2) the measured property could be for the oxidation layer of the nanostructure, instead of nanostructure itself because of the relative small load applied on the nanostructure. Nanoindentation was then mainly adopted for mechanical property measurement of 1D nanostructures in this dissertation.

CHAPTER 3: NANOINDENTATION ON TiO_2 NANORIBBONS

3.1 Introduction

As discussed in Chapter 1 and 2, nanoindentation is mainly used to measure mechanical property of 1D nanostructures throughout this dissertation work. Though nanoindentation can be performed relatively easily, a variety of factors need to be carefully considered to assure the accuracy of test results. For example, when studying the mechanical properties of thin films using nanoindentation, the underlying substrate could affect the measurement results significantly. In order to avoid the substrate effect, Bückle's rule (Bückle, 1973) is generally followed. The rule assumes that the substrate will not significantly affect the mechanical properties of a thin film if the indentation depth is less than 10% of the film thickness. However, it is often impractical to follow Bückle's rule as the thickness of films continuously decreases in many applications. Moreover, for a hard material on compliant substrate system, Bückle's rule is unrealistic due to the deformation of the substrate even under low load (Geng, *et al.*, 2008). Recently, the substrate effect has been extensively studied both numerically and experimentally in elastically mismatched film-on-substrate systems (Chen and Vlassak, 2001, Clifford and Seah, 2009, Gao, *et al.*, 2008, Han, *et al.*, 2006)**.** It has been shown that the substrate effects are significant: depending on the mismatch parameter between the elastic modulus of thin film and substrate, the effective modulus of the film-on-substrate system could be up to 10 times the modulus of the thin film itself (Gao, *et al.*, 2008). On the other hand**,**

to overcome many experimental issues associated with shallow indentation, such as indenter tip-film surface adhesion, specimen surface roughness, indenter tip bluntness and strain gradient effects, the substrate effect has been used to extrapolate the thin film elastic-plastic parameters from a moderate depth load-indenter displacement curve (Zhao, *et al.*, 2008). There is no doubt that the substrate effect is a very important consideration when determining mechanical properties of thin films.

In a similar manner, when performing the nanoindentation of a 1D nanostructure laid on a substrate, the substrate effect could also exist. To assure the testing accuracy, several questions need to be explicitly answered: How will the substrate affect the mechanical properties measurement of the 1D nanostructure? Will the substrate make the 1D nanostructure look more compliant or stiff? Are data produced by the software associated with the nanoindenter, the modulus of a nanostructure-on-substrate system, close to the "intrinsic" properties of the 1D nanostructure? An intrinsic property denotes the inherent property of the nanostructure, which is dependent mainly on the chemical composition or structure of the nanostructure. It is independent of how the nanostructure is measured. In the great majority of papers published on the nanoindentation of 1D nanostructures, the compliance induced by the contact between the nanostructure and the substrate was assumed to be negligible (Li, *et al.*, 2005, Mao, *et al.*, 2003). In other words, the measured modulus of nanostructure-on-substrate system was assumed as the intrinsic modulus of the nanostructure. *Is this assumption reasonable?* A double contact model for the nanoindentation of a nanowire on a flat substrate was proposed (Feng, *et al.*, 2006). The model considered two contacts in a series. One was the contact between the nanowire and the indenter (contact 1), modeled as an elliptical contact. The other was the

contact between the nanowire and the substrate (contact 2), modeled as a receding contact. Due to the difficulty to obtain the contact stiffness from the receding theory alone, the contact stiffness for contact 2 (S_2) was calculated using the analytical solutions derived from the elliptical contact theory with contact dimensions obtained from the receding contact theory. The calculated contact stiffness S_2 was much larger than the contact stiffness for contact 1 (S_1). Thus, a conclusion that contact 2 (*i.e.*, the substrate effect) could be ignored was drawn. However, an interesting question is raised: *could the contact stiffness between the nanowire and the substrate be overestimated?* Recently, Shu *et al.* numerically studied the nanoindentation of nanowires on elastic-plastic substrates and concluded that the measured hardness and Young's modulus of nanowires could be significantly influenced by the mechanical properties of the substrates (Shu, *et al.*, 2009). *Is there any experimental evidence for this conclusion?*

The present work is motivated by above research efforts and for the better understanding of the mechanical property measurement of 1D nanostructures with nanoindentation. Our focus is to explore how the substrate could affect the measured Young's modulus of 1D nanostructures. The work was done on titanium dioxide (TiO_2) nanoribbons. They are a class of nanomaterials with unique materials properties and promising applications in photo-catalysis, gas sensing, and photovoltaic devices (Chen and Mao, 2007). Both experimental work and numerical simulation were performed to study the Young's modulus of TiO_2 nanoribbons dispersed on three different substrates. Results showed that the properties of substrates significantly influenced the measured system modulus. To obtain reliable mechanical properties of a nanoribbon, suitable substrates need to be chosen. Otherwise, the Young's modulus of the nanoribbon could

be either overestimated or underestimated. For the single crystalline rutile TiO_2 nanoribbons, the measured modulus was close to the intrinsic modulus when sapphire(0001) was used as the substrate. The Young's modulus of TiO_2 nanoribbons with an average thickness of 30 nm and a half-width of 80 nm was determined to be around 360 GPa. To the best of our knowledge, this is the first time the Young's modulus of a rutile TiO_2 nanoribbon has been reported.

3.2 Experimental Details

Using a similar methodology described in our previous publication (Amin, *et al.*, 2007), TiO_2 1D nanostructures (Figure 3.1(a)) including both nanowires and nanoribbons were synthesized by annealing Ni-coated Ti powders. The 1D nanostructures were characterized to be single crystalline rutile with [110] as the preferred growth direction. The as-synthesized TiO_2 nanostructures were scraped off from powders and dispersed uniformly into absolute alcohol by ultrasonication. A few drops of alcohol solution were then deposited onto a substrate (1 cm × 1 cm). To study the substrate effect on the measurement of mechanical properties of 1D nanostructures, three different substrate materials including silicon substrate with 1 μm thick SiO_2 layer on top (SiO_2/Si), Si(100) and sapphire(0001) were used. Optical microscopy (Olympus BX51 research-level microscope; dark field) was employed to locate individual TiO_2 nanostructures on the substrate and to differentiate their morphologies. Under the optical microscope, the nanowires and nanoribbons appeared to be black and white, respectively. Our previous experience demonstrated that sliding of the nanostructure could occur, especially during the nanoindentation of a nanowire with a circular cross-section. The sliding phenomenon was more obvious when the expected Young's modulus of the nanowire was higher than

that of the substrate. Thus, to avoid the sliding problem during nanoindentation, only TiO_2 nanoribbons with rectangular cross-sections were selected and studied in this work. The nanoribbons identified by optical microscopy were further examined by Atomic Force Microscopy (AFM; Dimension 3100, Veeco Instruments Inc.) to verify their geometry and obtain dimensional information. The nanoribbons had an average thickness of 30 nm and a width of 150 nm. Figure 3.1(b) shows a representative AFM image of a single TiO_2 nanoribbon and the corresponding line profile. The selected nanoribbons were then subjected to nanoindentation without any further treatment.

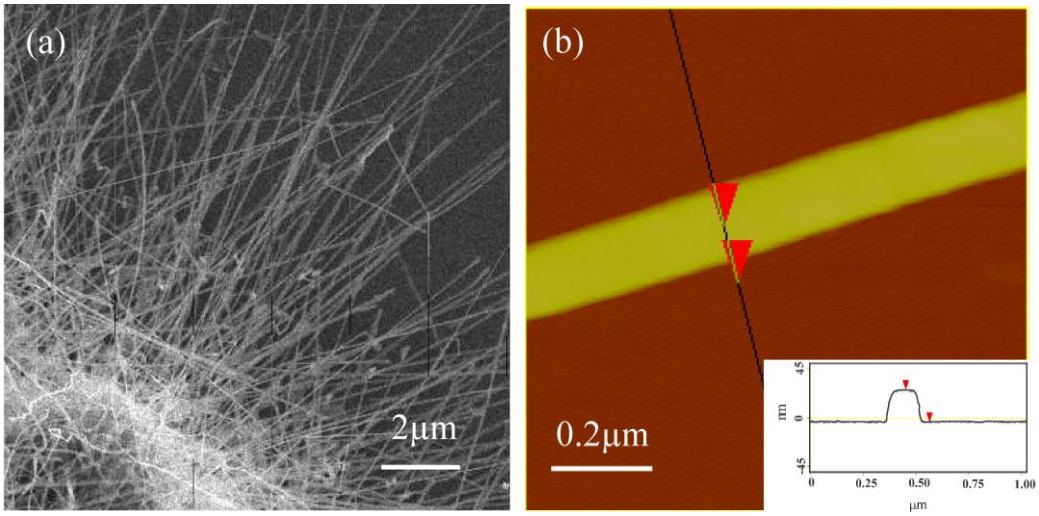

Figure 3.1: (a) the SEM image of as-synthesized TiO_2 1D nanostructures on a Ti powder. (b) an AFM image of a single TiO_2 nanoribbon. The inset is a cross-sectional profile of the nanoribbon, showing the nanoribbon is around 150 nm wide and 30 nm thick.

Nanoindentation was performed on both substrates and TiO_2 nanoribbons, using an Agilent Technology G200 nanoindenter equipped with the nanoVision Scanning Force Microscopy (SFM) option, the Continuous Stiffness Measurement (CSM) option and the

Dynamic Contact Module (DCM) option. The DCM head provides superior load resolution (1 nN) and displacement resolution (0.0002 nm) (MTS, 2007). A Berkovich indenter with a calibrated tip radius of ~ 80 nm was used. The tip radius was calibrated with a standard reference silica sample. The indentation processes were as follows: load to a set displacement with a constant strain rate of 0.05 s^{-1}; unload with the same strain rate to 10% of the maximum load and hold for 50 s to correct thermal drift; then complete the unloading. During the entire loading process, a harmonic perturbation with a 1 nm sinusoidal displacement was superimposed to the quasi-static main loading process for all tests. The amplitude and phase of the indenter displacement were measured with a synchronous detector. The harmonic contact stiffness *S* was determined continuously as a function of depth. (i) Nanoindentation of substrates. The loading depth was set to 120 nm. For each substrate material, 72 indentations clustered into two 6×6 matrices were made. The indentation data was processed by the software associated with the nanoindenter, by which the Young's modulus was calculated based on the standard Oliver-Pharr method (Oliver and Pharr, 1992). The obtained Young's moduli were averaged and presented in later sections. (ii) Nanoindentation of nanoribbons. Using the nanoVision SFM option, the DCM head was able to image (scan time: 15 s, scan load applied: 0.001 times the load that must be applied to the tip to keep it on the surface when traveling on a 45° slope (MTS, 2007) and indent individual nanoribbons. For each nanoindentation test, a maximum depth of 15 nm was employed. To obtain reliable data, at least 10 nanoribbons on each substrate were tested. After indentation, the residual indentations were examined by both the nanoVision SFM and AFM. Only the data obtained from those nanoribbons

with well-centered residual indentations were accepted and processed by the software associated with the nanoindenter.

3.3 Finite Element Modeling

Three-dimensional (3D) finite element modeling (FEM) was carried out to simulate indenting the nanoribbon-on-substrate system using the commercial software ABAQUS. The Berkovich indenter was modeled as a rigid cone indenter with a half-included angle of 70.3°, and an apex radius of the indenter at 80 nm. Due to symmetry, only a quarter of the nanoribbon-on-substrate system was considered. The bottom of the substrate was constrained in the *x*-, *y*- and *z*-directions. Symmetry conditions were applied on all symmetry planes. The contact between the indenter and the nanoribbon was assumed to be frictionless, as was the interaction between the nanoribbon and the substrate. Bulk parts of the nanoribbon and the substrate were modeled with C3D20R brick elements. The remaining elements where contact may occur were C3D27R brick elements, the midface nodes were added on the contact slave surface. The meshes gradually coarsened with the increasing distance from the indentation center to optimize the computational cost and accuracy. The minimum element size was 2.53 nm. And the number of elements increased during indentation process. At maximum indentation depth, at least 10 elements were in contact. The load (P) – indenter displacement (h) curve was obtained by recording the reaction force acting on the indenter and the corresponding indenter displacement.

The standard thickness and half-width of a nanoribbon was assumed to be 30 nm and 80 nm, respectively. The Young's modulus of the nanoribbon was assumed to be 110 GPa, 200 GPa and 350 GPa, respectively. As discussed in Section 3.4, these values

were chosen because of their closeness to the experimentally measured values of three different nanoribbon-on-substrate systems. The thickness and half-width of substrates were chosen to be 200 nm and 80 nm, respectively. This selection was based on a few simulations to ensure that the effect of substrate boundary conditions on the simulated reaction force of an indentation test on a half-space was within ~ 4% of the analytical solution, as shown in Figure 3.2. To save computational time and cost, the so-called infinite element method which simulates an infinite domain through a proper mapping (Zienkiewicz, 1989) could be used to simulate the substrate in this work. However, it is believed the results produced by the current simulation and the infinite element method will be similar. The Young's moduli of the substrates were assumed to be 90 GPa, 180 GPa and 500 GPa, respectively. These values correspond to the experimental values of SiO_2/Si, Si(100) and sapphire(0001), as discussed later in the text. The Poisson's ratio was 0.3 for both the nanoribbon and the substrate. Since the unloading process is elastic during the nanoindentation even if the tested material has undergone significant plastic deformation on loading, both the nanoribbon and the substrate were assumed to be elastic, homogeneous and isotropic when investigating the substrate effect on the Young's modulus of a nanoribbon. The basis of the assumption that both the nanoribbon and the substrate could be elastic is a few FEM results (Chen and Vlassak, 2001), which confirmed that contact stiffness must be the same for both elastic and elastic-plastic materials, as long as the contact area between an indenter and the tested material is the same. Note that for the elastic simulations, the loading and unloading curves are overlapped. If the nanostructure is anisotropic, a correction factor to the isotropic model could be introduced to a good approximation (Vlassak and Nix, 1994). That is, given

anisotropic factor a crystal, the indenation modulus on any surface can be easily obtained based on the isotropic model we studied here. For an isotropic material, the only two impendent materials constant is Young's modulus *E* and Possion's ratio.

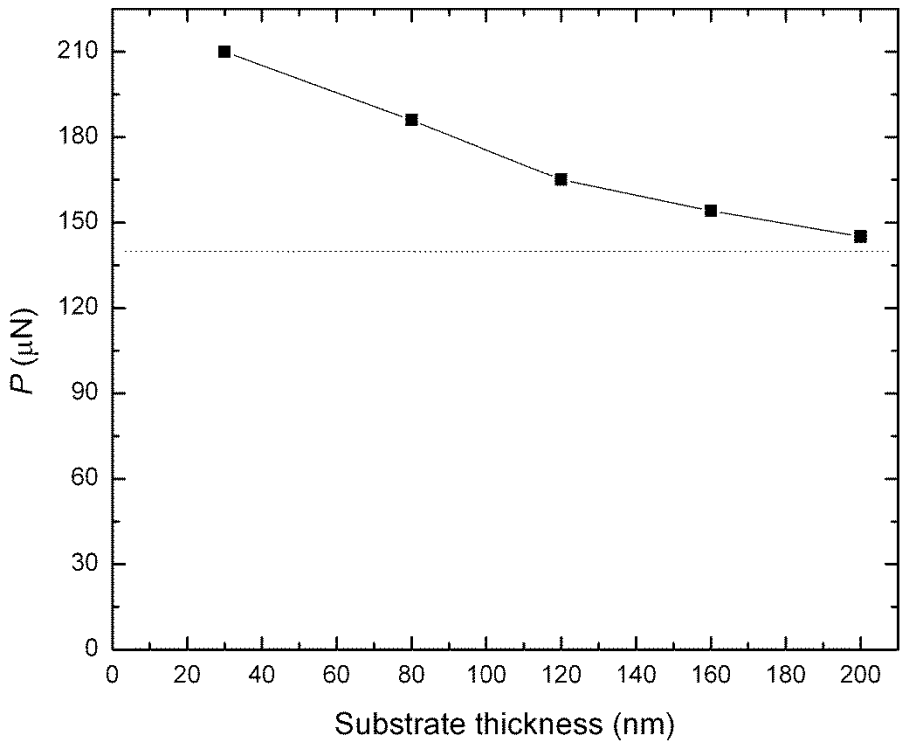

Figure 3.2: Simulated maximum load applied on a bare substrate of different thickness at an indentation depth of 15 nm. The Young's modulus of the substrate was 300 GPa. Tip radius of the spherical indenter in the simulation was 30 nm. The dotted line represented the analytical solution of the maximum load based on Hertz contact mechanics.

3.4 Results and Discussion

3.4.1 Experimental Results

3.4.1.1. Bare substrate characterization. The three substrates used in this study were subjected to nanoindentation as described in Section 3.2. The measured Young's moduli were 85 ± 1 GPa for SiO_2/Si, 185 ± 2 GPa for Si (100) and 503 ± 6 GPa for

sapphire (0001), respectively. These data provide references when performing the numerical simulation.

3.4.1.2. Nanoribbon-on-substrate system characterization. Nanoindentation was performed on individual TiO_2 nanoribbons dispersed on SiO_2/Si, Si(100) and sapphire(0001), respectively. After indentation, AFM was used to examine the residue indentation on nanoribbons. For the indentation of nanoribbon-on-SiO_2/Si, no residual indentation could be detected, indicating the yielding of SiO_2/Si substrate. For nanoindentation of nanoribbon-on-Si and nanoribbon-on-sapphire, clear residual indentations can be identified, implying that the hardness of the nanoribbon is comparable to or less than Si and sapphire. Figure 3.2(a) is a representative AFM image of an indented TiO_2 nanoribbon on a sapphire substrate. Several well-centered residual indentations can be observed. Additionally, indentation-induced fracture is seen at three indentation sites (indicated by the black arrows). It seems the crack initiated at the tips of indentation where stress concentration exists. These experimental observations not only qualitatively demonstrated that the substrate could affect the measurement results, but also provided fundamental information about the fracture behavior of TiO_2 nanoribbons. Figure 3.2(b) shows the typical *P-h* curves for TiO_2 nanoribbons on three different substrates. A pop-in phenomenon was observed in some test results, indicating the possible initiation and propagation of an indentation-induced crack (Yang, *et al.*, 2005). Based on these *P-h* curves, the Young's moduli calculated by the Oliver-Pharr method were around 110 GPa for a nanoribbon-on-SiO_2/Si, 200 GPa for a nanoribbon-on-Si, and 350 GPa for a nanoribbon-on-sapphire, respectively. There is no doubt that the substrate affects the accurate determination of the Young's modulus of TiO_2 nanoribbons. *So*

which experimental data is more reliable and close to the intrinsic modulus of TiO_2 nanoribbons?

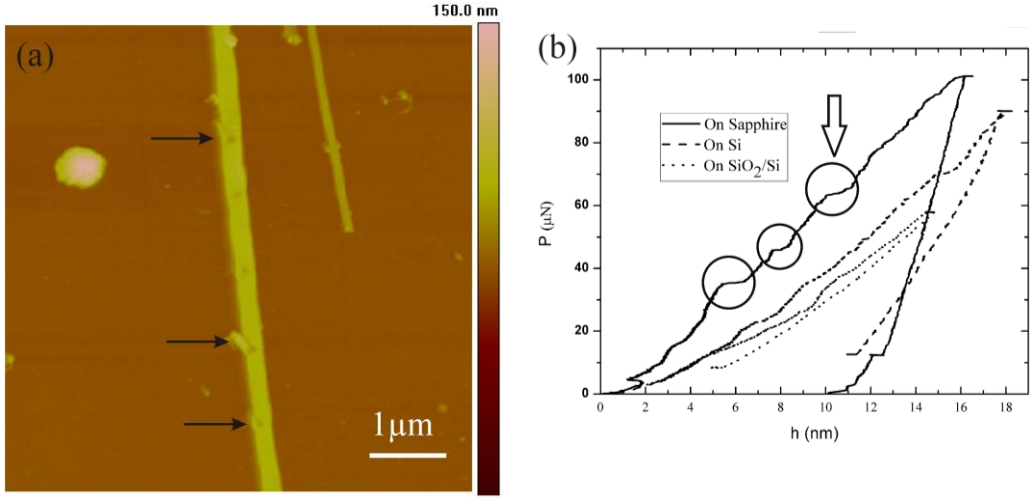

Figure 3.3: (a) AFM image of an indented nanoribbon on a sapphire(0001) substrate. Five well-centered residual indentations are shown. Sites where indentation-induced fracture occurred are indicated by black arrows. (b) Typical load-indenter displacement (P-h) curves for TiO_2 nanoribbons on three different substrates. The circles correspond to the possible pop-in phenomena.

3.4.2 Simulation Results

3.4.2.1. The contact between the nanoribbon and the substrate

Figure 3.3(a) is a typical simulated deformation pattern of a nanoribbon under indentation. The edges of the nanoribbon are lift-up, indicating the contact between the nanoribbon and the substrate is close to a receding contact (Keer, *et al.*, 1972). Figure 3.3(b) shows a typical AFM image of a TiO_2 nanoribbon after indentation. The brighter part between the two residue indentations implies the adhesion between nanoribbon and the substrate was weak so that the nanoribbon was lifted up during the indenting process. From both the simulated deformation pattern and the experimental observation, we

believe that receding contact mechanics should be a good approximation for the contact between the TiO_2 nanoribbon and the substrate.

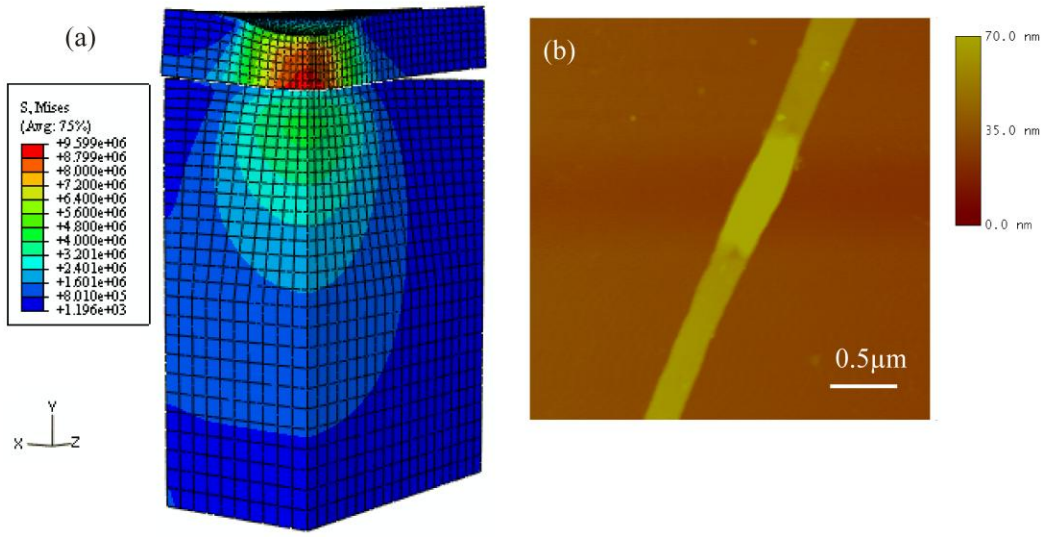

Figure 3.4: (a) Typical simulated deformation pattern of a nanoribbon-on-sapphire system under indentation. The edges of the nanoribbons are clearly lift-up. (b) Typical AFM image of a nanoribbon after nanoindentation. The brighter portion between the two residue indentations implies the nanoribbon was lifted up.

To validate the reliability of the FEM model and further understand the contact mechanics between the nanoribbon and the substrate, the analysis of the contact radius and the Dundurs parameter was carried out. The contact area between the nanoribbon and the substrate is a circle with a radius of a_2, and its value could be obtained from simulation. The Dundurs parameter α is given by $\frac{E'_{sub}-E'_n}{E'_{sub}+E'_n}$, where the reduced Young's modulus E' is defined as $E/(1-\nu^2)$, and E and ν are the Young's modulus and Poisson's ratio. (Note: the subscripts "sub" and "n" denote substrate and nanoribbon, respectively.) The relation between the ratio a_2/t (where t is the thickness of the nanoribbon and was assumed to be 30 nm in this work) and the Dundurs parameter α is plotted in Figure 3.4.

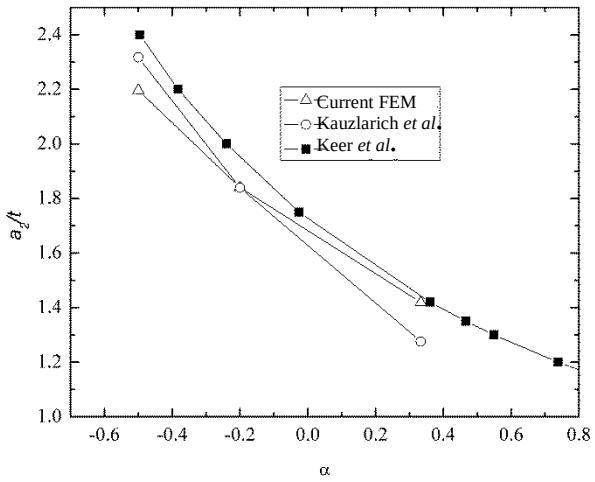

Figure 3.5: Plots of a_2/t vs α obtained from the receding contact model (Keer, *et al.*, 1972), the plate-on-foundation model (Kauzlarich and Greenwood, 2001), and the current FEM results. This analysis validates the reliability of the FEM model.

When E_{sub} is less than E_n ((*i.e.*, $\alpha < 0$), the ratio a_2/t agrees well with that calculated from the plate bending theory (Kauzlarich and Greenwood, 2001), indicating that the indentation test on nanoribbon-on-substrate system is better described by the classical plate-on-foundation model. On the other hand, when E_{sub} is larger than E_n (*i.e.*, $\alpha > 0$), the ratio a_2/t agrees well with that calculated by the axisymmetric receding contact theory (Keer, *et al.*, 1972). This analysis demonstrates that the FEM model is reliable.

3.4.2.2. Implication of the simulation results

Using the above validated FEM model, simulation of nanoindentation on three nanoribbon-on-substrate systems was carried out. The simulation results help us to answer two questions:

Question 1: As reported in Section 3.4.1.2, different values of Young's modulus were obtained when individual nanoribbons were put on different substrates (*e.g.*, 110 GPa for a nanoribbon-on-SiO_2/Si, 200 GPa for a nanoribbon-on-Si, and 350 GPa for a

nanoribbon-on-sapphire). Are any of these measured values close to the intrinsic Young's modulus of TiO_2 nanoribbons? If yes, which one? In other words, to get a reliable Young's modulus of an individual TiO_2 nanoribbon, which substrate should be chosen for nanoindentation tests? To answer these questions, the *P-h* curves of several nanoribbon-on-substrate systems as well as "half space" curves (*i.e.*, the *P-h* curve of an indentation into a homogeneous half-space that is made from the same material as the nanoribbon) were simulated (Figure 3.5(a)). By comparing the *P-h* curve of a nanoribbon-on-substrate system with its corresponding "half space" curve, whether the measured modulus is close to the intrinsic modulus can be identified.

The measured modulus of a TiO_2 nanoribbon was ~ 110 GPa when the nanoribbon was laid on a SiO_2/Si substrate. Assuming this value represents the intrinsic modulus of the nanoribbon, two *P-h* curves were simulated using the aforementioned FEM model. The curve denoted as "110 on SiO_2/Si" represents the *P-h* curve of an indentation of a nanoribbon (assumed Young's modulus: 110 GPa) on a SiO_2/Si substrate (assumed Young's modulus: 90 GPa) system. The assumed values correspond to the experimental values. The curve denoted as "110 half space" is the *P-h* curve of an indentation into a homogeneous half-space that is made from the same material as the TiO_2 nanoribbon whose Young's modulus was assumed as 110 GPa. The two simulated curves do not overlap with each other, indicating the measured modulus of 110 GPa is not the intrinsic modulus of TiO_2 nanoribbons. Similarly, by comparing the simulated curve of "200 on Si" with that of "200 half space", one can find out that the measured modulus of 200 GPa from a nanoribbon-on-Si system is not the intrinsic modulus of TiO_2 nanoribbons either. However, when sapphire was used as the substrate, the simulated *P-h*

curve of “350 on sapphire” overlaps with that of “350 half space”, indicating that the measured modulus of 350 GPa is close to the intrinsic modulus of TiO_2 nanoribbons. In short, the simulation results demonstrate that the measured modulus is not close to the intrinsic modulus unless a suitable substrate is used. For a nanoribbon-on-substrate system, the modulus measured by the software associated with the nanoindenter is actually an effective system modulus because it combines the contribution from both the nanoribbon and the substrate. This effective system modulus could be close to the intrinsic modulus of the nanoribbon if an appropriate substrate is chosen. For this work, sapphire (0001) is the proper substrate for measurement of TiO_2 nanoribbons.

To further illustrate the substrate effect on measurement reliability, the *P-h* curves (Figure 3.5(b)) for nanonindentation of a nanoribbon ($E_{assumed}$ = 350 GPa) on three substrates were simulated. The simulation results clearly showed the significance of substrate effect. When the nanoribbon is put on a substrate with a lower Young’s modulus (*e.g.*, 90 GPa for SiO_2/Si, or 180 GPa for Si), the simulated *P-h* curve is far from the “half-space” curve, and the Young’s modulus of the nanoribbon could be significantly underestimated. When a substrate with a higher Young’s modulus is chosen (*e.g.*, 500 GPa for sapphire), the simulated *P-h* curve closes to the “half-space” curve, indicating that the corresponding substrate is proper to obtain reliable data for nanoindentation of a TiO_2 nanoribbon.

Question 2: When using sapphire as the substrate and an indenter with the tip radius of 80 nm, will the change of the width of the nanoribbon affect the measurement results? Figure 3.5(c) shows the simulated *P-h* curves for nanoribbons with half-width as 40 nm, 60 nm, 80 nm and 100 nm, respectively. The narrower the nanoribbon, the farther

the *P-h* curve is away from the "half-space" curve. In other words, the effective system modulus provided by the nanoindenter software is an underestimation of intrinsic modulus. When the half-width of the nanoribbon increases, the width effect diminishes and the effective modulus is close to the intrinsic Young's modulus of the nanoribbon. Similar results were reported by Xu *et al.*, stating that a significant sample size effect could occur when the sample size is comparable to the indenter size (Xu and Li, 2006).

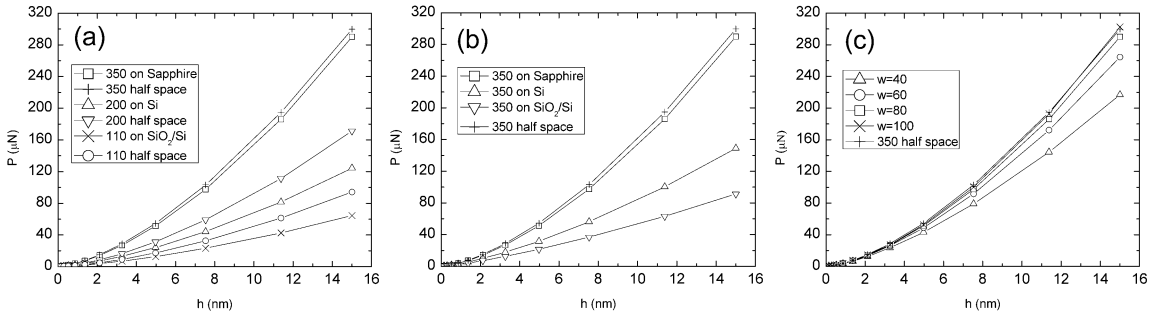

Figure 3.6: (a) Simulated *P-h* curves for nanoindentation of several nanoribbon-on-substrate systems as well as "half space" curves. The simulated "350 on sapphire" curve overlaps the "350 half space" curve, indicating the measured modulus is close to the intrinsic modulus of TiO_2 nanoribbons when sapphire (0001) is used as the substrate. (b) Simulated *P-h* curves for nanoindentation of a nanoribbon with assumed modulus as 350 GPa on three substrates. This result further illustrates the substrate effect on measurement reliability. (c) Simulated *P-h* curves for nanoindentation of nanoribbons with different width on a sapphire substrate. The width effect is significant when the width of a nanoribbon is close to the indenter size.

3.4.3 Data Analysis

The above FEM results showed that sapphire is the suitable substrate for nanoindentation of TiO_2 nanoribbons, and the corresponding measured modulus is close to the intrinsic modulus. The measured modulus was found between 300 GPa and 365 GPa, with an average value of 342 GPa. Though the measured data was close to the intrinsic modulus of TiO_2 nanoribbons, an inverse data analysis process was carried out

to obtain more accurate intrinsic values. The inverse process, as shown in Figure 3.7, was as follows: (i) taking the measured modulus m_0 as an initial guess of the intrinsic modulus of nanoribbons m_1, simulated the modulus of "m_1 on Sapphire", m; (ii) compared m and m_0, then increased or decreased the initial modulus value m_1 to a value m so that the modulus of "m on sapphire" equals to m_0; (iii) m_1 was the intrinsic modulus of the nanoribbon. For the nanoribbons with system moduli of 342 GPa, the extracted the moduli of nanoribbons was 360 GPa.

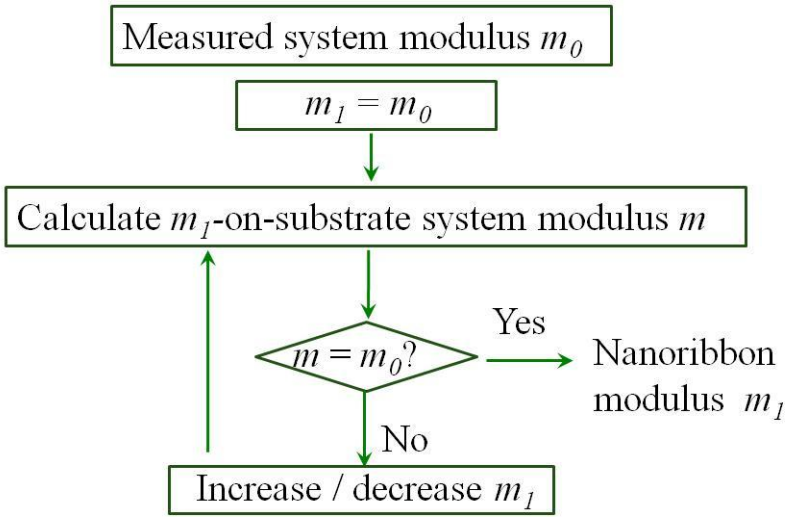

Figure 3.7: A general data inverse process of extracting the intrinsic modulus of a nanoribbon from the measured system modulus

Since the exact crystallographic information relating to the indented surfaces is unknown, it is difficult to make an accurate comparison between our results and the available Young's modulus data of bulk rutile TiO_2. However, it seems that the obtained Young's modulus of TiO_2 nanoribbons (*i.e.*, ~360 GPa) is comparable to that of bulk rutile TiO_2 (*e.g.*, $E_{\perp(110)}$=368.8 GPa, $E_{\perp(001)}$=385.8 GPa, $E_{\perp(111)}$=318.9 GPa) (Li and Bradt,

1993). The measured hardness is around 15 GPa, which is also comparable to the hardness of bulk rutile TiO_2 (*i.e.*,13 GPa (Mayo, *et al.*, 1990)).

3.4.4 A General Rule for Studying Young's Modulus of 1D Nanostructures by Nanoindentation

The current work demonstrates that the selection of a proper substrate is one key factor to obtain reliable measurement results of Young's modulus of 1D nanostructures by nanoindentation. The measurement from a single nanostructure-on-substrate system cannot produce reliable results. For example, if we only performed nanoindentation on TiO_2 nanoribbons laid on Si substrates, the obtained modulus of 200 GPa would be a significant underestimation of intrinsic modulus of TiO_2 nanoribbons.

Thus, to study the Young's modulus of 1D nanostructures by nanoindentation, experimental work need to be first performed on *different* nanostructure-on-substrate systems. For each nanostructure-on-substrate system, by comparing the measured modulus ($E_{n\ (measured)}$) with the Young's modulus of the substrate (E_{sub}), the substrate is identified as either proper or not. If $E_{n(measured)} > E_{sub}$, the substrate is not proper and the measured value is an underestimation of intrinsic modulus of the nanostructure. If $E_{n(measured)} < E_{sub}$, the substrate can be proper. However, the measured value might be overestimated. As a result, FEM work (such as the aforementioned inverse data analysis process) needs to be carried out to obtain a more reliable Young's modulus.

3.5 Conclusions

In summary, both experimental and numerical studies were carried out to investigate the Young's modulus of single crystalline rutile TiO_2 nanoribbons under nanoindentation. Three different substrates, including SiO_2/Si, Si(100) and

sapphire(0001), were used to support nanoribbons. Results show that the receding contact mechanics is a good approximation when describing the contact between the nanoribbon and the substrate. In addition, results demonstrate that a suitable substrate is one of the keys to obtain reliable measurement data of 1D nanostructures. The Young's modulus of TiO_2 nanoribbons was found to be around 360 GPa, comparable to that of bulk TiO_2. The work done here is a good example, demonstrating that both experimental and numerical investigations are needed for studying the mechanical properties of 1D nanostructures by nanoindentation. Otherwise, the Young's modulus of the nanoribbon could either be overestimated or underestimated.

To further improve the accuracy of results, there are several issues that need future consideration. For example, (i) Information related to the indenter tip radius/shape and nanoribbon width is critical for a quantitative mechanical properties extraction. Given this information, the intrinsic mechanical properties of the nanoribbon can be deduced more accurately through the aforementioned inverse process. (ii) Although the Young's modulus of the nanoribbon can be deduced from the elastic model of nanoribbon and substrate, the actual hardness of the nanoribbon should be studied based on a model including the plastic deformation.

CHAPTER 4: MEASUREMENT OF MECHANICAL PROPERTIES OF ALKALINE EARTH METAL HEXABORIDE ONE-DIMENSIONAL NANOSTRUCTURES BY NANOINDENTATION

4.1 Introduction

In Chapter 3, nanoindentation test on TiO_2 nanoribbons with width to thickness ratio about 5 was conducted. A general rule on selecting a proper substrate to support a nanostructure so that the measured nanostructure-on-substrate system modulus is closed to the nanostructure's modulus itself was discussed. Will the rule works for MB_6 nanostructures which have a width to thickness ratio about 1 to 2? This chapter tries to answer the question.

The divalent alkaline earth metal hexaborides MB_6 (M=Ca, Sr, Ba) crystallize in a CsCl-type structure with the cubic symmetry as Pm3m (Adams, 1964). The B_6 boron octahedra are at eight corners of a cube, whereas the metal atom is at the cubic body center (Adams, 1964). The B_6 boron octahedra link to each other by B-B bonds to form a rigid three-dimensional boron framework (Adams, 1964). As a result, MB_6 materials have properties of low densities, low thermal expansion coefficients, high hardness, high melting points and good chemical stability (Adams, 1964). They are also promising *n*-type high temperature thermoelectric materials because of their rising Seebeck coefficients (absolute value) and electrical conductivities as temperature increases (Imai, *et al.*, 2001, Takeda, *et al.*, 2006). Recent advances have shown that low-dimensional materials such as quantum dots, one-dimensional (1D) nanostructures and thin films provide new opportunities to achieve enhanced thermoelectric figure-of-merit (Dresselhaus, *et al.*, 2007, Dresselhaus, *et al.*, 1999).

Our latest synthesis of single crystalline MB_6 1D nanostructures, nanowires, has made the exploration of their thermoelectric performance possible (Amin, *et al.*, 2009, Xu, *et al.*, 2004). In addition to the study of thermoelectric properties, understanding the mechanical behavior of these MB_6 1D nanostructure is essential before they can be integrated into new devices. However, there have been no reports on mechanical properties of MB_6 1D nanostructures. Even for bulk MB_6 materials, only scarce data can be found (Grechnev, *et al.*, 2008, Kosolapova, 1990, Shang, *et al.*, 2007(Wei, *et al*., 2011), Datta, 1975).

The aim of this chapter is to measure the mechanical properties of 1D MB_6 nanostructures using nanoindentation. The measured moduli were quite scattering. Both experimental observation and numerical simulation demonstrate that the data scattering was due to several factors such as the width-to-thickness ratio of a nanostructure, the interaction between a nanostructure and a substrate, and the cross section of a nanostructure. A smaller nanostructure width-to-thickness ratio, a frictionless receding interaction and a circular cross section could all lead to a lower measured modulus. To find out the intrinsic Young's modulus of a nanostructure, the data inverse process was used to correct the experimentally measured modulus. The extracted intrinsic modulus of SrB_6, BaB_6 and CaB_6 1D nanostructures fell within ranges of 300-425, 270-475, and 175-365 GPa, respectively.

4.2 Experimental Details

Using the methodology described in our previous reports (Amin, *et al.*, 2009, Xu, *et al.*, 2004), single crystalline MB_6 1D nanostructures were synthesized by pyrolysis of diborane over nickel-coated alkaline earth metal oxide (MO) powders at elevated temperature and low pressure. The as-synthesized MB_6 nanostructures grew on top of

MO powders, forming an urchin-like geometry (Amin, *et al.*, 2009). The nanostructures were transferred to two different substrates: silicon(100) and sapphire(0001). The width and length of each substrate were about 0.5 cm and 1 cm, respectively. Two different methods were used for transferring nanostructures. (i) "Wet transfer" method. The nanostructures were scraped off from powders and dispersed uniformly into absolute alcohol by ultrasonication. A few drops of alcohol solution were deposited onto substrates which were subsequently blow dried by compressed nitrogen. (ii) "Dry transfer" method. Bare substrates were slid against powders for direct transferring of nanostructures. The substrates were then gently washed by stream alcohol and blow dried. Although it was confirmed later that the testing results were not affected by sample transfer methods, the "dry" one is preferred because it can transfer more nanostructures to a substrate. Optical microscopy (Olympus BX51 research-level microscope; dark field) was used to locate individual MB_6 nanostructures on substrates. The nanostructures were then studied by Atomic Force Microscopy (AFM; Dimension 3100, Veeco Instruments Inc.) to examine their geometry and obtain dimensional information. To avoid the sliding problem during nanoindentation, nanostructures with rectangular cross sections are preferred, as discussed in Chapter 3. Experimental results presented in Section 4.4.1 are all from nanostructures with well-defined rectangular cross sections. Both selected SrB_6 and BaB_6 nanostructures had a width of ~ 100-200 nm. However, the average thickness of SrB_6 nanostructures was ~ 100 nm and that of BaB_6 nanostructures was ~ 160 nm. The CaB_6 nanostructures were relatively small. Most of them had both thickness and width less than 100 nm. A few CaB_6 nanostructures were found to have circular cross sections.

Sliding phenomenon was observed for these CaB_6 nanostructures whose corresponding experimental results were discarded without further analysis.

All nanoindentation tests were conducted in the continuous-stiffness-measurement (CSM) mode of an Agilent Technology G200 nanoindenter, which is equipped with the nanoVision Scanning Force Microscopy (SFM) option and the Dynamic Contact Module (DCM) option. The indentation-loading scheme was similar to those described in Chapter 3. For general measurements of modulus and hardness, the maximum indenter displacement was set to 20 nm for SrB_6 and BaB_6 nanostructures, and 15 nm for CaB_6 nanostructures. For fracture behavior studies, the maximum indenter displacement was set to 30 nm for SrB_6 and BaB_6, and 20 nm for CaB_6. For each material, at least ten nanostructures on sapphire substrates were tested. For each nanostructure, multiple indentation tests were performed along its preferred growth direction. The residual indentations (~1-2 nm) were checked by the nanoVision SFM. Data analyses were only done on those nanostructures with well-centered residual indentations.

4.3 Modeling of Nanoindentation Experiment

4.3.1 A Better Way to Simulate Nanoindenter

For depth-sensing nanoindentation, with the help of an experimentally obtained indentation load - displacement (*P*-*h*) curve, the reduced elastic modulus E_r of a tested material can be determined based on the Sneddon theory (Oliver and Pharr, 1992)

$$E_r = \frac{\sqrt{\pi}}{2}\frac{dp}{dh}\frac{1}{\sqrt{A}} \tag{4-1}$$

where *P* is the load applied on the indenter, *h* is the indenter displacement into the surface of a tested material, *dP/dh* is the slope of the *P*-*h* curve upon unloading and *A* is the

projected contact area between the indenter and the tested material. Given E_r, Young's modulus for the tested material (E) can be obtained from the following equation with minor algebraic manipulation

$$\frac{1}{E_r} = \frac{1-v_i^2}{E_i} + \frac{1-v^2}{E} \tag{4-2}$$

where v is Poisson's ratio of tested material, and E_i and v_i are elastic properties of the indenter.

By observing the above two equations, the projected contact area A is obviously one important parameter need to be carefully analyzed. For example, an underestimation of A could lead to an over-determination of E. Thus, when performing numerical simulation, the shape of an indenter needs to be properly modeled to assure that the simulated values of A is close to the experimental data.

The solid line in Figure 4.1 is a plot of A vs. h_c (contact depth) obtained from our tip geometry calibration experiment. The line can be mathematically represented by the following functional form

$$A = \alpha_1 h_c^2 + \alpha_2 h_c \tag{4-3}$$

where α_1 = 24.427 and α_2 = 500. In Chapter 3, a conical indenter with a tip apex of $R = \alpha_2/2\pi$ were used to mimic the Berkovich indenter. The corresponding A-h_c curve is calculated and presented as the dashed line in Figure 4.1. The curve is obviously not overlapped with the experimental A-h_c curve, indicating the Berkovich indenter in our experiment should not be simply modeled as a conical one. Inspired by the work done by the Pharr's group (Bei, *et al.*, 2005), a rigid axially symmetric indenter of a revolution spline is used to simulate the Berkovich indenter. The inset in Figure 4.1 illustrates the

profile of the indenter, where r the contact radius is defined as $r = \sqrt{A/\pi}$ at any contact depth h_c.

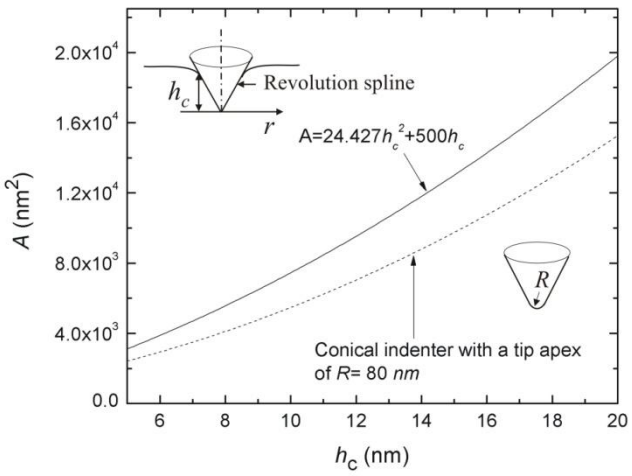

Figure 4.1: Projected contact area A vs. contact depth h_c curves. The solid line was obtained from a tip geometry calibration experiment of a Berkovich indenter. The dashed line was calculated assuming the intender is conical whose tip apex R is 80 nm.

4.3.2 Finite Element Modeling

Three-dimensional (3D) finite element modeling (FEM) was carried out to simulate indenting nanostructure-on-substrate systems using the commercial software ABAQUS. While the simulation parameters were similar to those used in Chapter 3, a couple of important modifications were employed in this chapter. (i) As discussed in Section 4.3.1, the Berkovich indenter was modeled as a rigid axially symmetric indenter of a revolution spline to ensure the accurate representation of A. (ii) The dimension parameters of nanostructures and sapphire substrates used to generate results in Section 4.4.2 are listed in Table 4.1. The thickness of a substrate was chosen to be at least 7 times of that (or diameter) of a nanostructure so that the substrate finite boundary condition effect can be

ignored. (iii) To compromise between the computational accuracy and cost, a coarse mesh with the minimum element size of 10 nm was chosen. This selection was based on a mesh sensitivity study. The maximum load applied on the indenter at the maximum indentation depth was compared between simulations using coarse (minimum element size: 10 nm) and fine meshes (minimum element size: 3.2 nm). The load difference was found to be 0.03%, indicating that the *P-h* curve is insensitivity to a mesh size. (iv)Two types of interactions between a nanostructure and a substrate were simulated. One was the frictionless receding contact. The other was a "tie" constraint to simulate the perfect bond interaction. For a nanostructure with the rectangular cross section, all six degrees of freedom of the nanostructure bottom surface were constrained with those of the substrate top surface. For a circular nanowire, it initially contact with the substrate on one line. The degrees of freedoms of nodes on the contact line were constrained with each other. (v) The Young's modulus of sapphire was set to be 500 GPa. The Poisson's ratio was chosen to be 0.3 for both the nanostructure and the substrate. Varying Poisson's ratios from 0.3 to 0, the simulation result (*i.e.*, the maximum load applied on the indenter at the maximum depth) was changed less than 5%, indicating the *P-h* curve is insensitivity to Poisson's ratios.

Table 4.1: Dimensions for nanostructures and sapphire substrate used in simulation. The units are nm.

Material	Nanostructure			Sapphire substrate		
	thickness (t)	half-width (w)	half-length	thickness	half-width	half-length
SrB_6	100	50 or 100	300	700	300	300
BaB_6	160	50 or 100	300	1120	300	300
CaB_6	$t = 2w$ = diameter (D) = 30, 60 or 80		300	560	300	300

4.4 Results and Discussion

4.4.1 Experimental Results

Preliminary tests were done on both nanostructure-on-silicon and nanostructure-on-sapphire systems. Sliding phenomenon was observed when indenting individual nanostructures on silicon, producing unreliable testing results. Thus, sapphire was chosen as the proper substrate to support MB_6 nanostructures for later nanoindentation tests.

Since similar experimental phenomena were observed for nanoindenting of MB_6 nanostructure-on-sapphire systems, only results for SrB_6 nanostructures are qualitatively described here. Figure 4.2(a) is a representative AFM image, showing a part of a SrB_6 nanostructure lying on sapphire. The inset presents the result of section analysis, revealing the nanostructure has a rectangular cross section and its thickness and width are ~ 108 nm and 100 nm, respectively. Figure 4.2(b) shows a typical *P*-*h* curve of a deformation process of the SrB_6 nanostructure-on-sapphire system. The elastic-like deformation behavior is observed. Figure 4.2(c) and (d) present the measured Young's modulus and "nanohardness", respectively. These data were automatically produced by the software associated with the nanoindenter, by which they were calculated based on the Oliver-Pharr method (Oliver and Pharr, 1992). The measured modulus seems to be constant when the indenter displacement is larger than 8 nm. The data variation at the initial stage could be due to the indenter tip rounding, surface roughness and machine resolution (Chen, *et al.*, 2005). Generally, the "nanohardness" (H) is defined as the peak load (P_{max}) applied during a nanoindentation divided by the projected contact area (A) of the indentation (Oliver and Pharr, 1992). It can also be considered as mean contact pressure (P_m) for a material under an elastic deformation. Depending on the indenter tip

geometry, various expressions of "nanohardness" with respect to the indenter displacement for elastic deformation was derived based on contact mechanics (Maugis, 2000). For a spherical indenter, the "nanohardness" is proportional to the square root of the indenter displacement (*i.e.*, $H \propto \sqrt{h}$). For a conical indenter, the "nanohardness" is independent of the indenter displacement. For a flat punch, the "nanohardness" is directly proportional to the indenter displacement (*i.e.*, $H \propto h$). Carefully analyzing Figure 4.2(d), one can find that the "nanohardness" increases with the indenter displacement in an asymptotic manner (*i.e.*, $H \sim h^{\alpha}$, $0.5<\alpha<1$), which indicates that the geometry of the indenter tip in our experiments is neither spherical nor conical indenter nor flat punch. This observation is consistent with the result obtained by analyzing the projected contact area *A*, as discussed in Section 4.3.1.

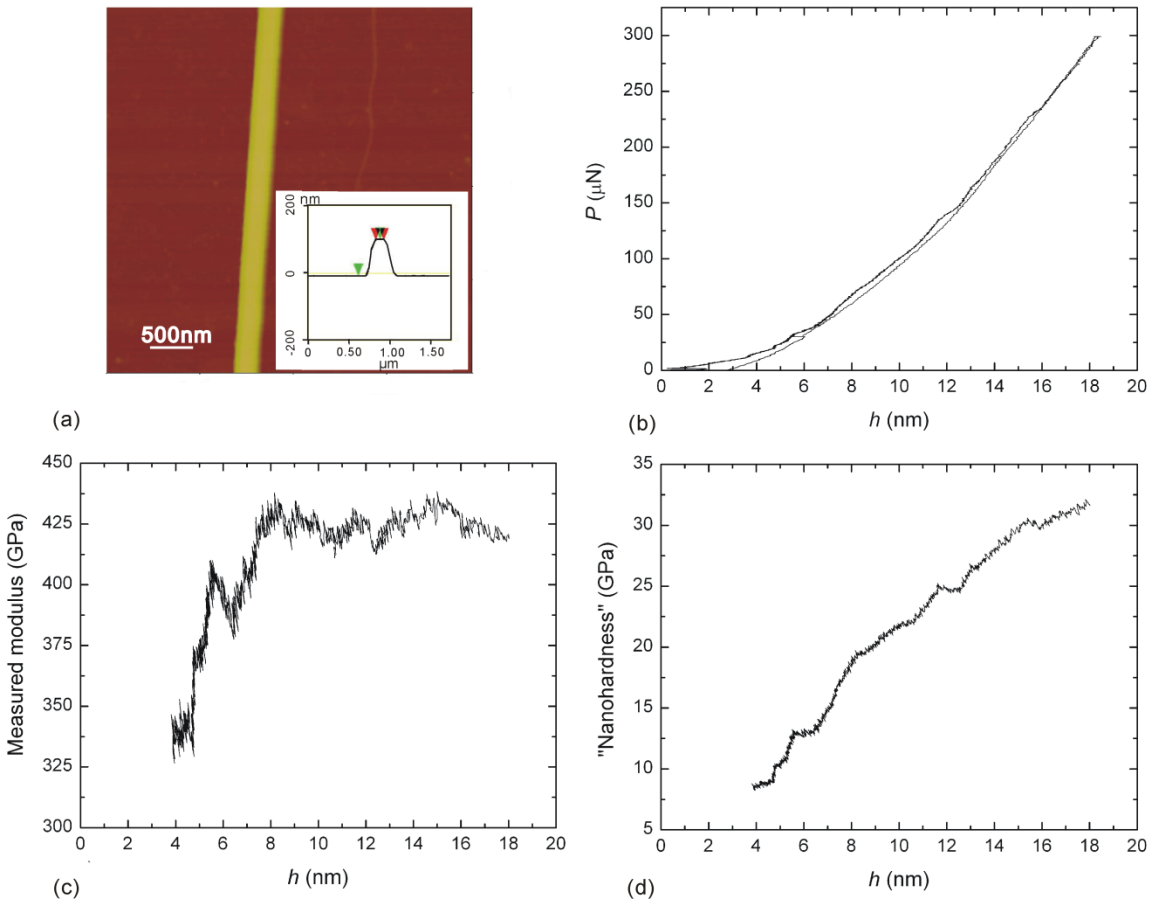

Figure 4.2: (a) An AFM image of a part of a SrB_6 nanowire on sapphire. The inset is the result of section analysis, revealing the nanostructure has a rectangular cross section. Its thickness and width is about 108 nm (vertical distance between two green arrows) and 100 nm (horizontal distance between two red arrows), respectively. (b) A typical load-indenter displacement (*P*-*h*) curve of the SrB_6 nanostructure-on-sapphire system. (c) Measured modulus and (d) "nanohardness" given automatically by the software associated with the nanoindenter. The values were calculated using the Oliver-Pharr method. Note: the noisy data points within the initial contact range (i.e., between 0 and 4 nm) were removed for clarity.

Figure 4.3 shows a *P*-*h* curve of a SrB_6 nanostructure fractured during an indentation process with the original maximum indenter displacement setting as 30 nm. When the indenter displacement reached 23 nm, the nanostructure suddenly fractured and the software lost control of the indenter until the indenter touched the sapphire substrate. Then the software "realized" that the indenter displacement was larger than the target

displacement and started to unload. Cracks might initiate when the indenter displacement was close to 23 nm, follow by a quick propagation and catastrophic fracture of the nanostructure. For total nine MB_6 nanostructures subjected to fracture behavior studies, similar *P-h* curves as shown in Figure 4.3 were observed. SrB_6 and BaB_6 nanostructures typically fractured when the indenter displacement was around 25 nm, whereas CaB_6 nanostructures failed when the indenter displacement was around 19 nm. The above indenter displacement at fracture is typically less than 30% of the thickness of a nanostructure. Each nanostructure broke into two parts, which was confirmed by the follow-up OM or AFM examination. This observed catastrophic fracture is different from other indentation-induced failure behavior reported for SnO_2 nanobelts (Mao, *et al.*, 2003) and ZnS nanobelts (Li, *et al.*, 2005, Yang, *et al.*, 2005) from which only crack initiation at the edges of the residual indentation or limited amount of crack propagation was found even the indentation displacement is about 40% of the thickness of the nanostructure. This study of fracture processes demonstrates the brittle nature of as-synthesized MB_6 1D nanostructures.

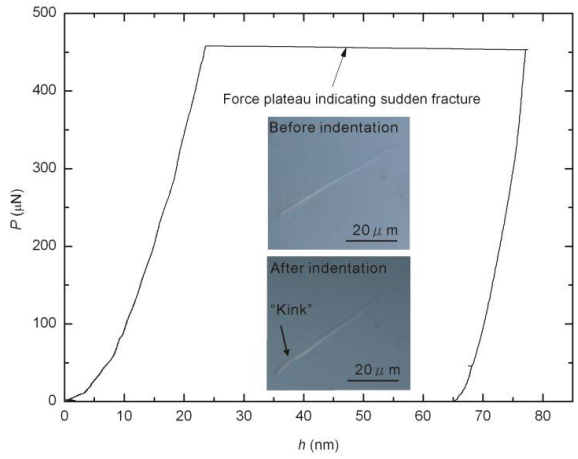

Figure 4.3: A *P-h* curve of a SrB_6 nanostructure experiencing sudden fracture during an indentation process

As mentioned in Section 4.2, multiple indentation tests were performed along the preferred growth direction of each tested 1D nanostructure. Most of time, two to four tests would be found valid (*i.e.*, a test produces a well-centered residual indentation), generating useful experimental data. As shown in Figure 4.4, for each tested nanostructure, the measured moduli are presented as a symbol against a vertical line. The symbol represents the mean value, whereas the ends of the vertical line (terminated by horizontal bars) indicate the minimum and maximum values. Analyzing experimental results presented in Figure 4.4, three important issues can be identified. (i) The measured moduli for MB_6 nanostructure-on-sapphire systems are scattering, and generally lower than the Young's modulus of MB_6 bulk materials (see dashed lines in Figure 4.4 and detailed data in Table 4.2). (ii) Special attention was paid to those data points (cf. SrB_6 at 103 and 117 nm thickness in Figure 4.4(b) and BaB_6 at 127 and 137 nm thickness in Figure 4.4(c)) associated with longer vertical lines (*i.e.*, have larger difference between the maximum and minimum values). It was found that these data were obtained from tapered nanostructures. Figure 4.5(a) is an AFM image of a typical tapered SrB_6 nanostructure. Two areas subjected to nanoindentation tests are outlined by white frames. The two areas are 2 μm apart. They are further enlarged in Figure 4.5(b) and (c) which were images produced by nanoVision SFM. Each image represents a 0.4 μm × 0.4 μm area, showing a part of the tested nanostructure. The black portion corresponds to the flat top of the nanostructure, from which the width of the nanowire can be determined. The width of the part of the nanostructure shown in Figure 4.5(b) is about 150 nm, while that in Figure 4.5(c) is about 200 nm. The corresponding measured modulus in these two areas is (b) 340 GPa and (c) 380 GPa, respectively. This result indicates that the

measured modulus is sensitive to the width of a nanostructure. (iii) Further examination of those data (−◊−) with lower measured modulus shown in Figure 4.4(b) and (c) revealed that the associated tested nanostructures were ~ 25-50% narrower than other tested nanostructures. For example, in Figure 4.4(b), the nanostructure of 108 nm in thickness was only 100 nm in width, and the nanostructure of 113 nm in thickness was about 150 nm in width. Other tested SrB_6 nanostructures were about 200 nm in width. This result again demonstrated that the measured modulus of a nanostructure-on-substrate system is sensitive to the width of the nanostructure. The narrower the nanostructure is, the lower the measured modulus can be.

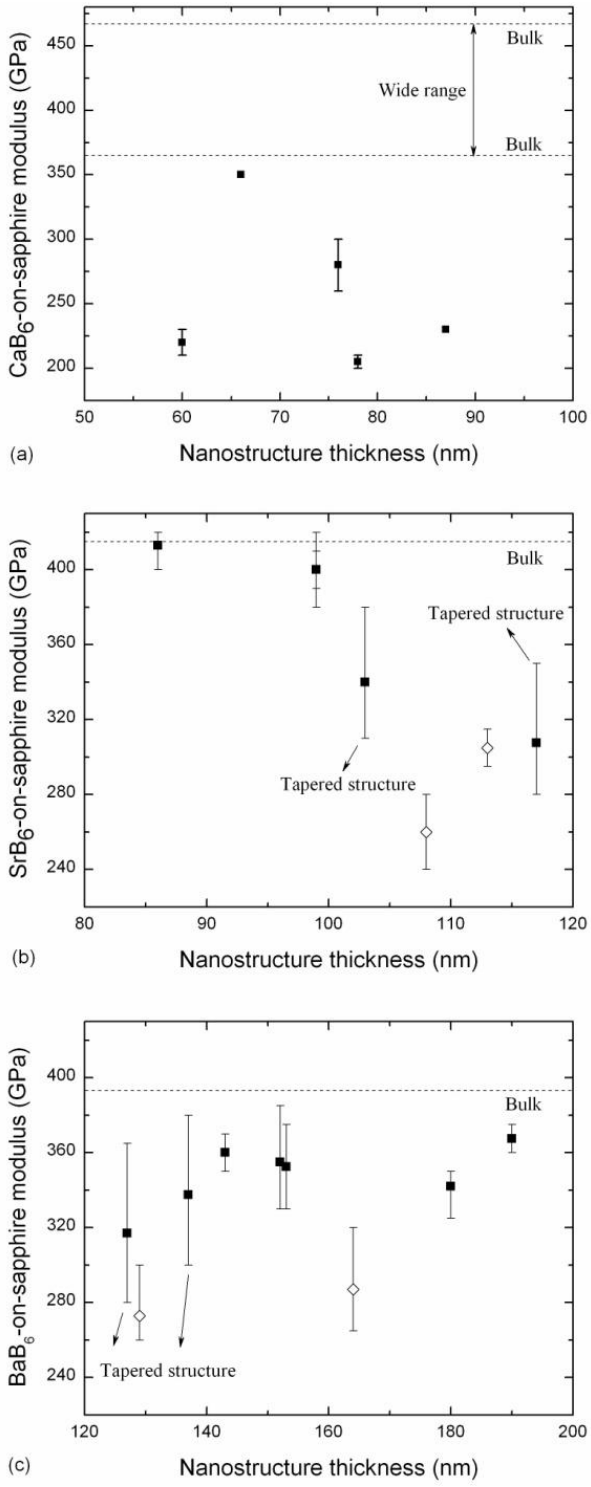

Figure 4.4: Measured moduli of (a) the CaB_6 nanostructure-on-sapphire system, (b) the SrB_6 nanostructure-on-sapphire system, and (c) the BaB_6 nanostructure-on-sapphire system.

Table 4.2: Experimental and theoretical values of elastic constants of some hexaborides

Materials	C_{11} (GPa)	C_{44} (GPa)	C_{12} (GPa)	B_{exp} (GPa)	B_{theory} (GPa)	E (GPa)
CaB_6	423[a]	43[a]	5.6[a]	–	145[a],159[b],139[c]	423[a],467[d], 365-399[e]
SrB_6	–	–	–	–	160[b],141[c]	415[d]
BaB_6	–	–	–	–	162[b],139[c]	393[d]
LaB_6	463[b]	89[b]	45[b]	184[b]	185[b]	488[d],439[f]

B=(C_{11}+2C_{12})/3 is the bulk modulus.
[a] Theoretical data at 0 K(Wei, *et al*., 2011)
[b] Experimental and theoretical data at 78K (Grechnev, *et al.*, 2008)
[c] Theoretical data at 298K (Shang, *et al.*, 2007)
[d] Calculated or experimental (hot-pressed) data (Kosolapova, 1990)
[f] Experimental (hot-pressed) data (Dutta, 1975)
[f] Single crystal nanostructure (Zhang, *et al.*, 2008)

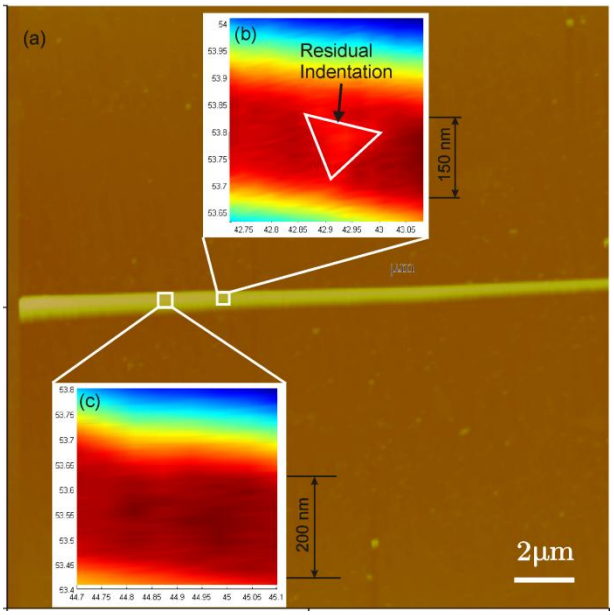

Figure 4.5: (a) AFM image of a tapered SrB_6 nanostructure on sapphire. (b) Zoom-in SFM image of an indented section of the nanostructure. The white triangle frame outlines the residual indentation. (c) Zoom-in SFM image of a section before indentation. The width of the two sections is obviously different.

4.4.2 Numerical Simulation

The aforementioned experimental results unambiguously demonstrate the scattering of measured moduli could be due to several factors such as the width-to-thickness ratio of a nanostructure with a rectangular cross section. To further study the effects of these factors, FEM-based simulation of nanoindentation on nanostructure-on-substrate systems were carried out. The dimensions listed in Table 4.1 were used for simulation. Due to the similarity of simulation results obtained from three MB_6 nanomaterials, data presented here is typically for SrB_6 unless noted otherwise.

Factor 1: the width of a nanostructure with a rectangular cross section. Figure 4.6(a) shows the simulated *P-h* curves of nanostructures with different width. The legend "w=100 400 on 500 perfect bond" represents a nanostructure with a half-width *w* of 100 nm and a Young's modulus of 400 GPa is perfectly bonded to a sapphire substrate with a Young's modulus of 500 GPa. "400 half space" denotes a homogeneous half space with a modulus of 400 GPa. The *P-h* curve of "w=100 400 on 500 perfect bond" is steeper than that of "400 half space" (note: comparison was done on the slope *dP*/*dh* upon unloading of each curve), indicating that the measured modulus of this nanostructure-on-sapphire system would be higher than the intrinsic nanostructure modulus: 400 GPa. When the half-width of the nanostructure is reduced to 50 nm, the corresponding *P-h* curve of "w=50 400 on 500 perfect bond" is now less steep than that of "400 half space", implying the measured modulus will be lower than 400 GPa. These simulation results are consistent with aforementioned experimental findings. They clearly demonstrate that the measured modulus is not the intrinsic nanostructure modulus and can be affected by the width of a nanostructure. The measured modulus decreases as the width of a

nanostructure decreases. This conclusion is also valid when the interaction between a nanostructure and a substrate becomes frictionless receding contact.

The width effect is qualitatively illustrated in the inset of Figure 4.6(a). Considering a nanostructure with an infinite width and finite thickness t laid on a substrate, the interaction radius between the nanostructure and the substrate is a_2 during an indentation of a certain indentation depth-to-nanostructure thickness (h/t) ratio. When the width of the nanostructure becomes finite, two situations exist. (i) The half-width w of the nanostructure is larger than a_2. Indentation on this type of nanostructures is same as indentation on infinite wide nanostructures. In other words, no width effect exists. (ii) The half-width of the nanostructure is smaller than a_2. Indentation of these narrower nanostructures deviates from that of infinite wide nanostructures. The deviation increases as the half-width of the nanostructure decreases. One implication is that the rule on selecting a proper substrate, proposed in Chapter 3, is invalid for a nanostructure with a half-width less than a_2. Detailed studies of the width effect have been carried out and the results will be discussed in Chapter 5. It was found that analytical solution can be used to study nanoindenting of wider nanostructures whereas FEM-based modeling is needed for narrower nanostructures.

Factor 2: the interaction between a nanostructure and a substrate. As shown in Figure 4.6(b), the *P-h* curve of "w=100 400 on 500 perfect bond" is steeper than that of "w=100 400 on 500 receding". This result indicates a perfect bond interaction between a nanostructure and a substrate could lead to a higher measured modulus. Based on the inverse data analysis method introduced in Chapter 3, it can also be derived that a perfect bond interaction could lead to a corrected modulus at the lower bound.

Factor 3: the cross section of a nanostructure. As mentioned in Section 4.2, a few CaB_6 nanostructures were found to have circular cross sections. Although nanoindentation on these circular nanostructures not produces reliable testing results due to the sliding problem, it is natural to ask ourselves a question: "Is there any effect of cross section on measured moduli if no sliding happens?" Simulations were done on nanostructures with two different cross sections: square and circular. The square has an edge length of 80 nm, whereas the circle has a diameter of 80 nm. Receding contact interaction was considered between the nanostructure (assumed modulus: 300 GPa) and the substrate (assumed modulus: 500 GPa). As shown in Figure 4.6(c), the simulated *P-h* curve for a nanostructure with a circular cross section is less steep than that with a square cross section, and also the "300 half space" curve. In other words, a circular cross section could result in a lower measured system modulus. This result is qualitatively consistent with the previous work (Shu *et al*., 2009), in which they concluded that for a nanostructure with a circular cross section, the measured moduli could be 50% lower than the intrinsic modulus of the nanostructure.

Factor 4: *the diameter of a nanostructure with a circular cross section.* Most of the tested CaB_6 nanostructures have circular cross sections. How does the diameter (D) of a nanostructure affect measured moduli? Our simulation results revealed that the diameter effect is tangled with the substrate effect. A smaller diameter indicates a smaller contact width (which is the short axis of the contact ellipse) between a nanostructure and a substrate, which shall result in a lower measured modulus. However, a smaller diameter also means that the nanostructure is shallow and the measured modulus is prone to be affected by the underlining substrate. Several *P-h* curves of nanoindenting nanostructures

of different diameters are shown in Figure 4.6(d). The assumed modulus of the nanostructure is 400 GPa, whereas that of the substrate is 500 GPa. The *P-h* curve of a nanostructure with a diameter of 60 nm is less steep than that of 80 nm, implying the measured modulus decreases as diameter decreases. However, when the diameter is further decreased to 30 nm, the corresponding *P-h* curve becomes steeper, indicating that a higher measured modulus would be obtained. The inset in Figure 4.6(d) shows the load at the maximum indentation depth: 15 nm for three different diameters, from which no linear relation between *P* and *D* can be found. These results demonstrate that the reduction of diameter does not always lead to a lower measured modulus. When the diameter is smaller than a certain value, substrate effect could show out, resulting in a higher measured modulus.

Factor 5: the oxide layer surrounding a nanostructure. Each as-synthesized nanostructure has a core-sheath geometry (Amin, *et al.*, 2009, Xu, *et al.*, 2004). The core is crystalline MB_6. The sheath is amorphous oxide whose thickness can be up to 4 nm. Will this oxide layer affect the *P-h* curve of a nanostructure-on-substrate system when the maximum indentation depth is 20 nm? To answer this question, simulation was conducted on a sandwich nanostructure combining of a thick core and two thin oxide surface layers. The thickness of the core and each oxide layer is 92 nm and 4 nm, respectively. Simulation was also done on a "pure nanostructure" whose thickness is 100 nm. The half-width of both nanostructures is 100 nm. The core and oxide layer modulus were assumed to be 400 and 150 GPa respectively. Both perfect bond and receding contact interaction were considered, and similar results were obtained. As revealed in Figure 4.6(e), the difference between the slope *dP*/*dh* upon unloading for the simulated

P-h curves of a "pure nanostructure" and a "sandwich nanostructure" is less than 3%. In other words, the oxide layer has minor effects on nanoindentation tests. This is due to the factor that the effective flexural rigidity of the sandwich nanostructure is close to that of a pure material (Chen, *et al.*, 2006).

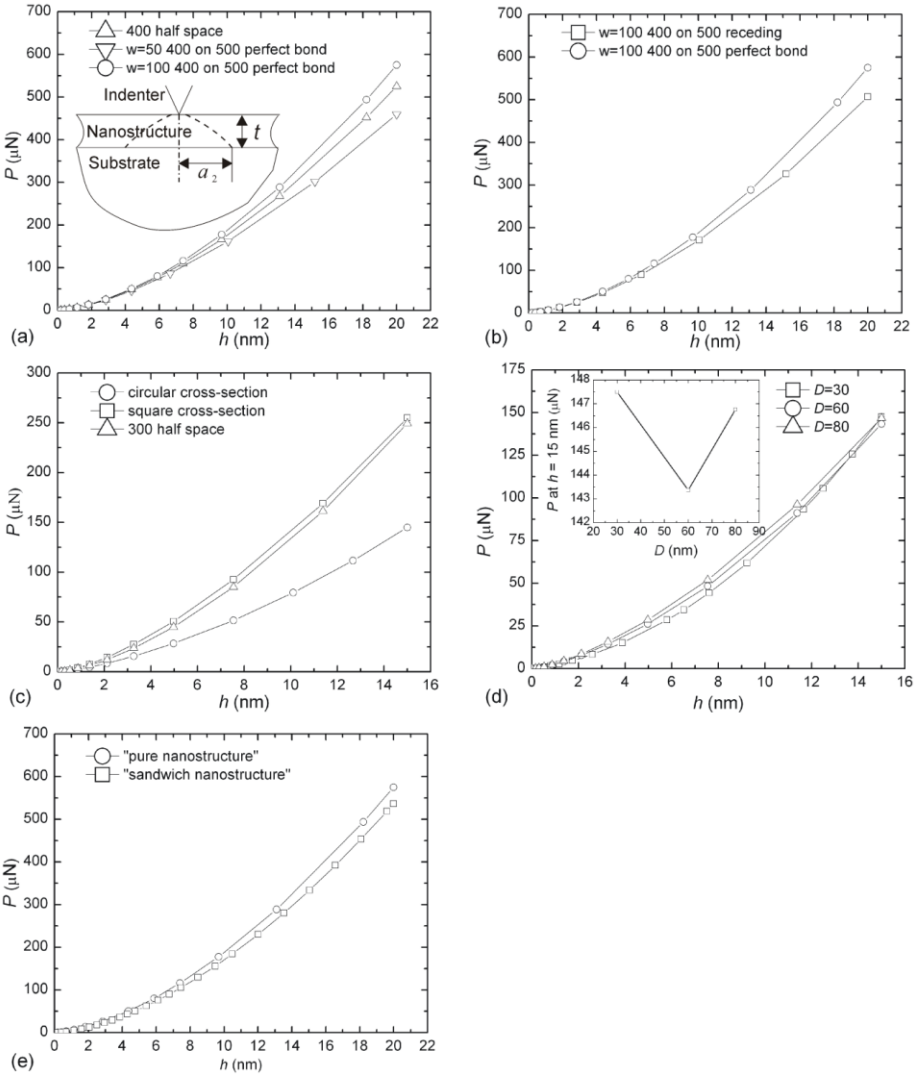

Figure 4.6: Simulated *P-h* curves for studying of various factors affecting measured moduli. These factors include (a) the width of a nanostructure with a rectangular cross section, (b) the interaction between a nanostructure and a substrate, (c) the cross section of a nanostructure, (d) the diameter of a nanostructure with a circular cross section and (e) the oxide layer on a nanostructure.

4.5 Data Analysis

The aforementioned experimental results and numerical simulation have clearly revealed that the measured modulus generally cannot represent the intrinsic Young's modulus of a nanostructure. In addition, the measured modulus can be easily affected by several factors. A narrower nanostructure, a frictionless receding contact and a circular cross section can all generally result in a lower measured modulus. To obtain a reliable value of Young's modulus of a nanostructure, the data inverse method proposed in Chapter 3 is used to correct the measured modulus.

As outlined in the introduction section, correction needs to be done for both the perfect bond and the frictionless receding interaction mechanisms. The perfect bond interaction leads to a corrected modulus at the lower bound, whereas the frictionless receding contact interaction yields a modulus at the upper bound. The intrinsic modulus shall fall between the two bounds. It is possible that the value is more towards to the lower bound since ultrasonication tests revealed relatively strong adhesion between the nanostructures and the substrate. Table 4.3 shows the data analysis results for a couple of tested 1D nanostructures. For each material, data correction was done on two nanostructures. The two nanostructures were chosen because their width-to-thickness ratio and measured modulus are the maximum and minimum among all tested nanostructure. As shown in Table 4.3, it seems that the intrinsic modulus of MB_6 nanostructures is dependent on the width-to thickness ratio. The larger the width-to-thickness ratio is, the higher the intrinsic modulus can be.

Table 4.3: Measured nanostructure-on-substrate system moduli and corrected nanostructure moduli for two different nanostructure-substrate contact interactions.

Material	Thickness × Width (nm × nm)	Width-to-thickness ratio	Measured Modulus (GPa)	Corrected Modulus (GPa)	
				Receding	Perfect Bond
CaB_6	66 × 95	1.43	350	365	300
	78 × 84	1.08	205	210	175
SrB_6	86 × 200	2.33	413	425	325
	108× 100	0.93	260	370	300
BaB_6	143 × 183	1.28	360	475	400
	129 × 129	1.00	273	330	270

Mechanical properties of single crystals are commonly anisotropic. Therefore, it is important to correlate the measured properties with crystallographic information. The surfaces of as-synthesized MB_6 1D nanostructures are (100) planes (Futamoto, *et al.*, 1979, Xin, *et al.*, 2011, Zhang, *et al.*, 2008). In other words, the nanoindentation loading direction is perpendicular to (100) planes. MB_6 materials have a cubic symmetry, indicating only three elastic constants are needed to estimate the crystallographic direction-dependent Young's moduli. Unfortunately, rare experimental and theoretical data about the elastic constants of MB_6 can be found after extensive literature search (Table 4.2). The unavailability of reliable information on elastic constants prevented us to estimate effective modulus for indenting against MB_6 nanostructures, study their anisotropic ratio, and make detailed comparison between experimental data and theoretical values.

4.6 Conclusions

In summary, Young's moduli of alkaline-earth metal hexaboride 1D nanostructures were studied by nanoindentation. The experimentally measured moduli were scattering. Systematic experimental investigation and numerical simulation

revealed that the data scattering can be caused by several factors such as the width of a nanostructure with a rectangular cross section and the interaction between a nanostructure and a substrate. A narrower nanostructure, a frictionless receding interaction, a circular cross section can all lead to a lower measured modulus. To obtain a reliable intrinsic modulus of a nanostructure, a FEM-based inverse data processing method was used. The modulus extracted based on the receding contact and the perfect bond interaction gives upper and lower bound values of the intrinsic modulus of the nanostructure, respectively. The intrinsic modulus of MB_6 nanostructures is dependent on the width-to thickness ratio. The larger the width-to-thickness ratio is, the higher the intrinsic modulus can be.

CHAPTER 5: NANOINDENTATION-THEORETICAL MODELING

5.1 Introduction

In Chapter 3 and 4, nanoindentation was conducted on TiO_2 nanoribbons and MB_6 nanostructures. The measured nanostructure-on-substrate system modulus could be significantly different from modulus of the nanostructure itself. This chapter revisited the semi-analytical solution of nanoindentation on a nanostructure-on-substrate system. A Mathematica program was developed to calculate system modulus under nanoindentation using a conical, spherical indenter or a general indenter with a given area function. Two different interactions between a nanostructure and a substrate, *i.e.* perfect bond and frictionless contact, were considered in the semi-analytical solution.

5.2 Chebyshev Polynomial

Chebyshev polynomials have been used to solve integral equations. They will be used to solve the Fredholm equation in Section 5.4. The properties of the polynomials, expression a function with the polynomials, derivative and integral of the function are reviewed in this section.

The m^{th} Chebyshev polynomial has m distinct roots on [-1,1], where the roots $(x_i)_{i=1}^{m}$ are:

$$x_i = -\cos\left(\frac{(2i-1)\pi}{2m}\right)$$

The Chebyshev polynomials are discrete orthogonal. In other words, for all $i, j < m$, the following relationship holds true (Chen, *et al.*, 2005),

$$\sum_{k=1}^{m} T_i(x_k)T_j(x_k) = \begin{cases} 0, & i \neq j \\ m/2, & i = j \neq 0 \\ m, & i = j = 0 \end{cases} \quad (5\text{-}1)$$

To approximate a function $f(\cdot)$ defined on [-1,1] using the first *m=n+1* Chebyshev polynomials, the *j* weights $(w_j)_{j=1}^{m}$ needs to be given. To solve the weights,

$$\sum_{j=0}^{n} w_j T_j(x_k) = f(x_k), \qquad k = 1, \dots, m. \quad (5\text{-}2)$$

Multiply both sides by $T_i(x_k)$, getting

$$\sum_{j=0}^{n} w_j T_i(x_k)T_j(x_k) = T_i(x_k)f(x_k)$$

Sum across *k*=1,2,…, m, getting

$$\sum_{k=1}^{m}\sum_{j=0}^{n} w_j T_i(x_k)T_j(x_k) = \sum_{k=1}^{m} T_i(x_k)f(x_k)$$

According to the discrete orthogonality property, the terms on the left side where $i \neq j$ are equal to zero. Thus

$$w_i \sum_{k=1}^{m} T_i(x_k)T_i(x_k) = \sum_{k=1}^{m} T_i(x_k)f(x_k)$$

Hence,

$$w_0 = \frac{1}{m}\sum_{k=1}^{m} f(x_k)$$

$$w_i = \frac{2}{m}\sum_{k=1}^{m} T_i(x_k)f(x_k) \qquad i = 1, \dots, n$$

A continuous and bounded variation function $f(x)$ can be approximated in the interval [-1, 1] by the formula

$$f(x) = w_0 + \sum_{i=1}^{n} w_i T_i(x)$$

The integral can be computed as

$$\int_{-1}^{1} f(x)dx = \frac{2}{m}\sum_{k=1}^{m} f(x_k) + \frac{2}{m}\sum_{i=1}^{n}\sum_{k=1}^{m} T_i(x_k) f(x_k) \frac{1+\cos i\,\pi}{1-i^2}$$

5.3 Formulation of the Indentation on Nanostructures (2w/t→∞)-on-Substrate System

For a nanostructure with width to thickness ratio approaches infinite, the nanostructure-on-substrate system is similar to a thin film-on-substrate system, which was solved by Yu *et al* (Yu, *et al.*, 1990). In their approach, two pairs of harmonic Papkovich-Neuber functions were used to formulate the thin film and the substrate respectively. Substituting the two functions into boundary conditions and continuity conditions between the nanostructure and the substrate, nanoindentation on nanostructure-on-substrate system was transformed into a Fredholm integral equation. The kernel of the Fredholm integral equation was complicated. In this Chapter, Airy's stress function was used to formulate the thin film and the substrate respectively so that the kernel of the Fredholm integral equation was greatly simplified. Equations to obtain *P–h* curves of nanoindentation on a nanostructure-on-substrate system and system modulus were presented. Interface stress between the nanostructure and substrate was also included to justify the applicable range for $2w/t \to \infty$ assumption.

Here, three rigid axisymmetric indenters indenting on a nanostructure with elastic constant μ_1, ν_1 -on-substrate with elastic constant μ_2, ν_2 system were considered. The indenters were chosen because they could represent an actual indenter used in an experiment. A cylindrical coordinate system, as shown in Figure 5.1 was used, where *z*

axis is along nanostructure thickness direction and *r* axis perpendicular to *z*. The origin of the coordinates is located at the center of the top surface of the substrate.

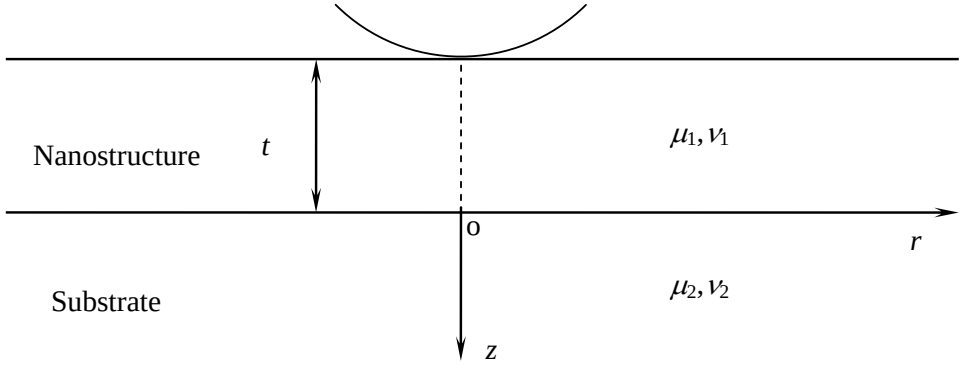

Figure 5.1: A composite system of an elastic nanostructure either perfect bond or frictionlessly overlaid on a half-space substrate indented by an indenter.

Assume the zero-order Hankel transform of the Airy's functions for a nanostructure and a substrate are $\Phi_0^H(\xi,z) = (A + B\xi z)e^{-\xi z} + (C + D\xi z)e^{\xi z}$ and $\phi_0^H(\xi,z) = (E + F\xi z)e^{-\xi z}$ respectively, displacements and stresses of the nanostructure and substrate can be expressed as function of arbitrary constants *A*, *B*, *C*, *D*, *E*, *F*(Maugis, 2000). For perfect bond condition between a nanostructure and a substrate, continuity of displacements and tractions are $\|u_r\|_{z=0} = \|u_z\|_{z=0} = \|\sigma_z\|_{z=0} = \|\tau_{rz}\|_{z=0} = 0$, where $\|\cdot\|$ denotes jump across the nanostructure and substrate interface. And boundary conditions on the surface of the nanostructure are:

$$\tau_{rz}(r,-t) = 0 \tag{5-3}$$

$$u_z(r < a,-t) = \delta - f(r) \tag{5-4}$$

$$\sigma_z(r > a,-t) = 0 \tag{5-5}$$

where $f(r)$ is the profile of an indenter. $f(r) = r\cot\alpha$, $f(r) = R(1-(1-r^2/R^2)^{1/2})$ and $f(r) = (-\alpha_2 + \sqrt{\alpha_2^2 + 4\pi\alpha_1 r^2})/(2\alpha_1)$, $0 \le r \le a$ for a conical, a spherical indenter and an axial symmetry general indenter with an area function $A = \alpha_1 h_c^{\ 2} + \alpha_2 h_c$ respectively. α is the half-angle of a conical indenter and R is the radius of the spherical indenter. α_1 and α_2 are experimentally calibrated indenter parameter.

A, *B*, *C*, *D* and *E* were solved in terms of *F* from the continuity condition and boundary condition (5-3). And displacement and stress boundary conditions (5-4) and (5-5) were expressed as follows:

$$\int_0^\infty M(\xi) J_0(\xi r)\, d\xi = -\frac{\mu_1}{(1-\nu_1)}(h - f(r)) \quad 0 \le r < a \tag{5-6}$$

$$\int_0^\infty \xi \frac{M(\xi)}{1-g(\xi)} J_0(\xi r)\, d\xi = 0 \qquad a \le r < \infty \tag{5-7}$$

Where,

$$M(\xi) = \frac{F\xi^2((1-\lambda_2^2)\exp(3\xi t) - 4\xi t(1-\lambda_2)(\lambda_1-\lambda_2)\exp(\xi t) + (\lambda_2^2-\lambda_1^2)\exp(-\xi t))}{(1+\lambda_1)(1+\lambda_2)\exp(2\xi t) - (1-2\xi t)(1+\lambda_1)(\lambda_2-\lambda_1)}$$

$$g(\xi) = 1 - \frac{(1-\lambda_2^2)\exp(4\xi t) - 4\xi t(1-\lambda_2)(\lambda_1-\lambda_2)\exp(2\xi t) + \lambda_2^2 - \lambda_1^2}{(1-\lambda_2^2)\exp(4\xi t) + (4(\xi t)^2(1-\lambda_2)(\lambda_1-\lambda_2) + 2(\lambda_1+\lambda_2^2))\exp(2\xi t) + \lambda_1^2 - \lambda_2^2}$$

The above formulations used the generalized Dundurs parameters

$$\lambda_1 = \frac{\mu_2(1-\nu_1) - \mu_1(1-\nu_2)}{\mu_2(1-\nu_1) + \mu_1(1-\nu_2)}$$

$$\lambda_2 = \frac{\mu_2(1-2\nu_1) - \mu_1(1-2\nu_2)}{2(\mu_2(1-\nu_1) + \mu_1(1-\nu_2))}$$

Assuming $M(\xi) = (1-g(\xi))\int_0^a \varphi(s)\cos(\xi s) ds$, $\varphi(x) = -\frac{2\mu_1 h}{\pi(1-\nu_1)} H(\tau)$ and $\tau = \frac{x}{a}$ the above two equations were solved if $H(\tau)$ satisfied the following Fredholm integral equation:

$$H(\tau) - \frac{a}{\pi}\int_0^1 H(v)[G(v+\tau) + G(v-\tau)]\, dv = F_0(\tau) \tag{5-8}$$

$$H(1) = 0 \tag{5-9}$$

The kernel of the integral equation is $G(x) = \int_0^\infty g(\xi)\cos(\xi x)d\xi$. $F_0(\tau)$ depends on the shape of a indenter. $F_0(\tau) = 1 - \gamma\tau$ for a conical indenter and $F_0(\tau) = 1 - \gamma^2\tau^2$ for a spherical indenter while indentation depth is less than 0.2 t (Yu, *et al.*, 1990). For the aforementioned general indenter, $F_0(\tau) = 1 - \frac{a\tau}{h}\int_0^{\frac{\pi}{2}} \frac{2\pi a\tau \sin s}{\sqrt{\alpha_2^2 + 4\pi\alpha_1 a^2\tau^2(\tau\sin s)^2}} ds$.

Likewise, for indentation on a nanostructure frictionlessly in contact with a substrate, the nanoindentation problem satisfies the same Fredholm integral equation (5-8) and (5-9) except for a different kernel

$$G(x) = \int_0^\infty \left(1 - \frac{(exp(4\xi h) + (2(1-\lambda_1)\xi h - (1+\lambda_1))\, exp(2\xi h) + \lambda_1)}{(exp(4\xi h) + (-2(\xi h)^2(1-\lambda_1) + 2\xi h(1+\lambda_1) - 1 + \lambda_1)\, exp(2\xi h) - \lambda_1)}\right)\cos(\xi x)d\xi$$

The Fredholm integral equations ((5-8) and (5-9)) were solved numerically using the Elgendi's method (El-gendi, 1969). The detailed procedures were as follows: (i) Approximating $H(\tau)$ with first N+1 Chebyshev polynomial ($N \geq 5$), as discussed in Section 5.2, and substituting it into equations (5-8) and (5-9), N+2 linear algebraic equations with N+2 unknowns (in Table 5.1) were obtained at a given a/t. Instead of guessing a value for γ_j (j = c, s) and solving $H(\tau_i)$ from equation (5-8) and iterating the procedure until equation (5-9) was satisfied, as suggested in reference (Yu, *et al.*, 1990), all the unknowns were solved directly by solving (5-8) and (5-9) together by a direct matrix inversion. The computation time was greatly minimized by using the scheme compared to the iterative one. For a conical and spherical indenter, γ_j (j = c, s) was deliberately chosen as an unknown. Once the linear equations were solved for a a/t through the direct matrix inversion using MATHEMATICA 5.1, a_h was calculated from $a\gamma_j$ and the corresponding h, t given in Table 5.1. For a general indenter, $\delta = t/h$ was

chosen as an unknown and solved instead. (ii) P was expressed in terms of unknowns, as listed in Table 5.1. System modulus was defined as $M_{sys} = S_{sys} / 2a$, whereas nanostructure modulus was defined as $M_1 = S_1 / 2a_h$. $M_{sys} / M_1 = S_{sys} / (\gamma_j S_1)$ was derived from the definition of the two modulus. where stiffness S_j (j = *sys* and 1) is the derivation of P with respect to h, which was numerically determined using a central difference scheme $(P|_{h+\Delta h1} - P|_{h-\Delta h2}) / (\Delta h1 + \Delta h2)$, in which $\Delta h1$ and $\Delta h2$ were small deviation from h. For indentations with a conical or a spherical indenter, the numerically determined stiffness of indenting a half-space was carefully compared with the analytical solutions. The closeness of the two values gives confidence of using the central difference scheme to determine stiffness.

For a conical and a spherical indenter, all relevant information can be assembled in a spreadsheet (Han, *et al.*, 2006) and M_{sys} / M_1 can be readily calculated at any h. For the general indenter, the calculation was conducted in a different way and results were organized in a format shown in Table 5.2. The first four columns are a/t, load P, h and stiffness of a nanostructure-on-substrate system. The fifth column is a'_h/t for a half-space made of the nanostructure, which is same as first column. The sixth and seventh columns are corresponding load and displacement into the nanostructure/system. Note that column six and seven corresponding to a different displacement into surface as listed in column three. The eighth and ninth columns list the interpolated load and a_h/t at a given indentation depth h so that M_{sys} / M_1 can be calculated at that depth. Stiffness and M_{sys} / M_1 were then calculated and listed in the following two columns.

Table 5.1: Unknowns and equations for the three indenters

Indenter	Unknowns	h/t	P
Conical	$H(\tau_i),\ \gamma_C$	$\frac{\pi}{2\gamma_c \tan\alpha}\frac{a}{t}$	$-\frac{8\mu_1}{\pi(1-\nu_1)}\gamma_C h^2 \tan\alpha \int_0^1 H(\tau)d\tau$
Spherical	$H(\tau_i),\gamma_s^{\ 2}$	$\frac{t}{\gamma_S^{\ 2}R}(\frac{a}{t})^2$	$-\frac{4\mu_1}{1-\nu_1}\gamma_S h^{3/2}R^{1/2}\int_0^1 H(\tau)d\tau$
General	$H(\tau_i),\ \delta$	$1/\delta$	$-\frac{4\mu_1}{1-\nu_1}ha\int_0^1 H(\tau)d\tau$
Notes: 1. $i=1,\ldots,N+1$; 2. $\delta = t/h$			

Table 5.2: Spreadsheet configuration of derived results from the Fredholm equation for the general indenter

Nanostructure-on-substrate				Half-space						
a/t	P (N)	h (m)	S_{sys} (N/m)	a'_h/t	P_1' (N)	h' (m)	P_1 (N)	a_h/t	S_1 (N/m)	M_{sys}/M_1
0.01	-	-	-	0.01	-	-	-	-	-	-

Given the solution of above unknowns, the indentation on a nanostructure-on-substrate system problem is fully solved. Here, interface stress $\sigma_z(r,0)$ between a nanostructure and a substrate was studied to justify the applicable range of the assumption $2w/t\to\infty$. Substituting A_1, B, C, D into $\sigma_z(r,0) = (1-\nu_1)\frac{d^3\Phi_0^H(\xi,z)}{dz^3} - (2-\nu_1)\xi^2\frac{d\Phi_0^H(\xi,z)}{dz}$, the interface stress was be expressed in terms of F or $\frac{M(\xi)N(\xi)}{1-g(\xi)}$, *i.e.*

$$\sigma_z(r,0) = -a\int_0^\infty H(\tau)\int_0^1 N(\xi)J_0(\xi r)\cos(\xi\tau)\xi\, d\xi d\tau.$$

For the perfect bond condition between a nanostructure and a substrate,

$$N(\xi) = -\frac{(1+\lambda_1)((1+\xi t(1-\lambda_2))\exp(3\xi t)+(\lambda_1+\xi t(\lambda_2-\lambda_1))\exp(\xi t))}{(1-\lambda_2^2)\exp(4\xi t)+(4(\xi t)^2(1-\lambda_2)(\lambda_1-\lambda_2)+2(\lambda_1+\lambda_2^2))\exp(2\xi t)+\lambda_1^2-\lambda_2^2}$$

And for frictionless contact condition between a nanostructure and a substrate,

$$N(\xi) = \frac{(1+\lambda_1)(-1+\xi t+\exp(2\xi t)(1+\xi t))\exp(\xi t)}{\exp(4\xi t)+(-2(\xi t)^2(1-\lambda_1)+2\xi t(1+\lambda_1)-1+\lambda_1)\exp(2\xi t)-\lambda_1}$$

5.4 Numerical Observations

Assuming both nanostructure and substrate are elastic, M_{sys}/M_1 vs. h/t for a perfect bond and a frictionless contact between a nanostructure and a substrate were calculated and shown in Figure 5.2(for a conical indenter) and Figure 5.3 (for a spherical indenter) respectively. The range of *a*/*t* studied here was from 0 to 1 with increments of 0.01. The Modulus mismatch between a nanostructure and a substrate (λ_1) was from -0.5 to 0.5 with a step size of 0.1. Assuming the nanostructure and substrate have same Poisson's ratio 0.3, the relationship between the Dundurs is given by $\lambda_2 = \lambda_1/3.5$. Note that all calculations for a spherical indenter listed in Figure 5.3 were based on an assumption that the indentation depth was small, *i.e.* indentation depth is less than 0.2*t.* Some findings were listed as follows:

1. *Nanostructure and substrate contact effect.* For both contact conditions between a nanostructure and a substrate, system modulus is different from nanostructure modulus ($M_{sys}/M_1 \neq 1$) for a large modulus mismatch between a nanostructure and a substrate λ_1 and a relative indentation depth larger than 0.1, $h/t > 0.1$. The System elastic modulus further deviates from the modulus of a nanostructure as the indentation depth h/t increases. As h/t approaches zero, i.e., h approaches zero (a shallow indentation) or t increases to ∞ (a very thick nanostructure), the system modulus approaches to that of a nanostructure. In Figure 5.2 (a) and (b), the dotted lines correspond to contour of constant contact area $a/t = 1$ and 0.5. Smaller λ_1 implies larger

h/t at same a/h, which indicates that the substrate with lower modulus can accommodate larger deformation and larger h/t, whereas substrate with higher modulus confines the deformation of the nanostructure with lower modulus and gives smaller h/t. Same conclusions hold true for a spherical and any other general indenter.

On the other hand, different interaction conditions imply different system moduli while other variables such as h/t and λ_1 are same. For perfect bond condition, the nanostructure-on-substrate system modulus is same as the modulus of the nanostructure, *i.e.* $M_{sys}/M_1 = 1$, when the nanostructure and the substrate are identical materials. Nonetheless, system modulus is less than the modulus of the nanostructure, $M_{sys}/M_1 < 1$, when the nanostructure and the substrate have same modulus and be frictionlessly contacted with each other. Instead, $M_{sys}/M_1 = 1$ when the nanostructure is put on a substrate with higher modulus, which gives a Dundurs parameter λ_1 is about 0.2. Moreover, for a nanostructure with high modulus on a substrate with a low modulus, frictionless contact interaction condition shows larger m_{perc} (percent difference between system modulus and nanostructure modulus) than its perfect bond counterpart.

2. *Indenter type effect*. For a conical indenter, modulus of the system depends on half-angle of the indenter for both perfect bond and frictionless contact interactions, as shown in Figure 5.2(c), where h/t and $\lambda_1 = 0.3$. The larger the indenter half-angle, the further the deviation of system modulus from modulus of the nanostructure. As a result, a cube corner indenter with a smaller equivalent half-angle of 42.3^{o} (Zhang, *et al.*) is more preferable to probe the mechanical properties of small-scale structures than a Berkovich indenter, which typically has an equivalent half-angle of 70.3^{o}. For a spherical indenter, modulus of the system depends on radius R of the

indenter. System modulus further deviates from the modulus of a nanostructure as the radius increases.

For both conical and spherical indenters, the Fredholm integral equation is only a function of a/t, which is related to h/t. M_{sys}/M_1 is a function of h/t instead of h as a result, whereas the equation depends on both a/t and the thickness t of the nanostructure for a general indenter, which implies that M_{sys}/M_1 is function of t as shown in Figure 5.4, where dash line shows M_{sys}/M_1 for a conical indenter on a nanostructure perfectly bonded with a substrate system and $\lambda_1 = 0.3$. The solid lines represent a general indenter with area function $A = 24.427h_c^{\,2} + 500h_c$ indenting on the same nanostructure-on-substrate system but with different nanostructure thickness. Thinner nanostructure demonstrates that system modulus is more affected by underlying substrate.

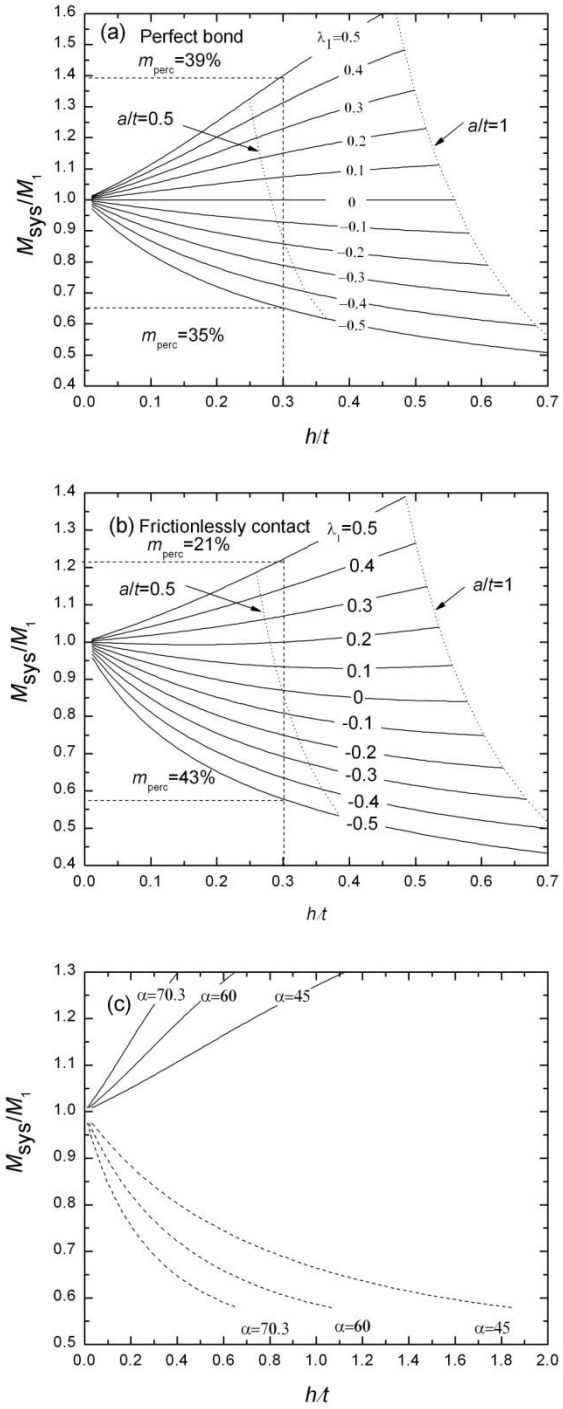

Figure 5.2: M_{sys}/M_1 vs. h/t for different elastic mismatch with a conical indenter of half-angle $\alpha = 70.3^{o}$ for (a) perfect bond and (b) frictionless contact between a nanostructure and a substrate. And (c) its dependence on the half angle of a conical indenter for the perfect bond interaction while $\lambda_1 = 0.3$(—) and for frictionless contact interaction while $\lambda_1 = -0.3$(----).

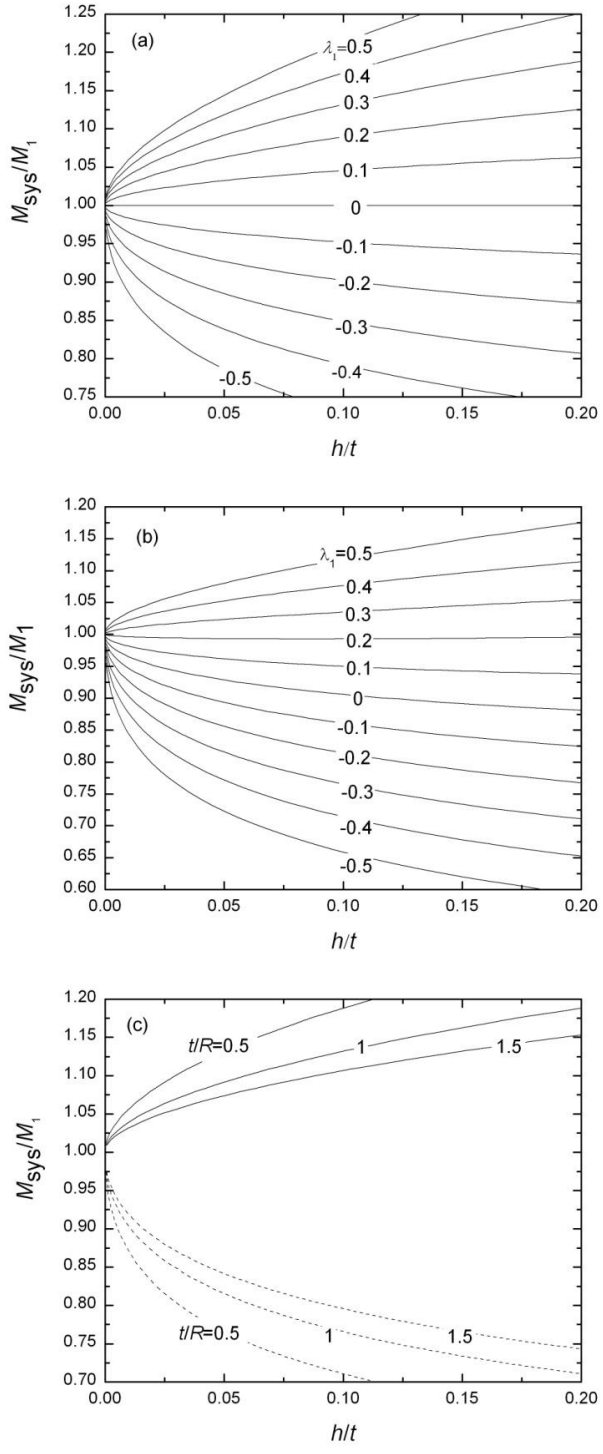

Figure 5.3: M_{sys}/M_1 *vs.* h/t for different elastic mismatch with a spherical indenter for (a) perfect bond and (b) frictionless contact between a nanostructure and a substrate when *t/R* = 1. And (c) its dependence on *t/R* for the perfect bond interaction while $\lambda_1 = 0.3$(—) and for frictionless contact interaction while $\lambda_1 = -0.3$(----).

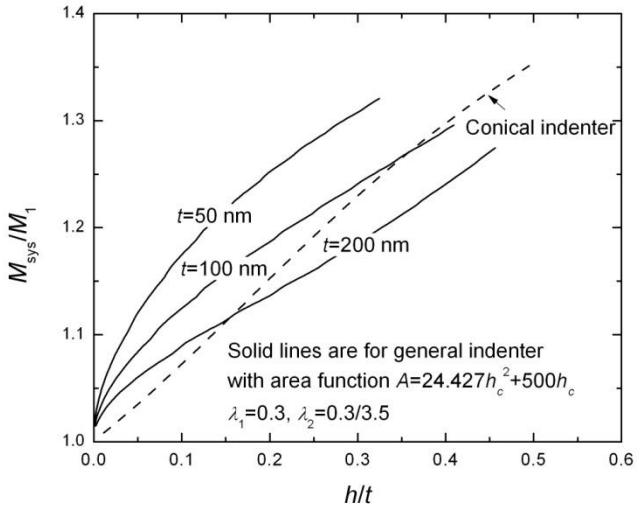

Figure 5.4: Comparison of M_{sys}/M_1 *vs.* h/t between a conical indenter and a general indenter in a nanoindentation test. The modulus of a nanostructure-on-substrate system using a general indenter is function of *t* and *h*/*t*, where the modulus of the system using a conical indenter is only function of *h*/*t*.

5.5 Applicable Range for 2w/t→∞ Assumption

In Section 5.3, mathematical equations have been developed to evaluate system modulus of an infinite wide nanostructure-on-substrate system. However, *what is the applicable range for infinite wide assumption? When can nanostructure be considered as infinite wide in reality?* Using the equations derived in Section 5.3, normalized interface stress between a perfectly bonded nanostructure and substrate $\sigma_z(r,0)$ along radius direction (*r*/*t*) when $\lambda_1 = \pm 0.3$ and $a/t = 0.1$ is calculated and shown in Figure 5.5. The interface stress quickly decays to zero as *r*/*t* approaches 2, which indicates that the infinite wide assumption for nanostructure is valid when half-width to thickness ratio, *w*/*t*, is larger than 2. In other words, the solution derived in this chapter is inapplicable for nanostructures with a width to thickness ratio being less than 4, for example, the MB_6 nanostructures we studied in Chapter 4. Finite element modeling, which was used in

Chapter 3 and 4, should be used to study the nanostructure-on-substrate system. The conclusion we drew here holds true for any indenters and interaction conditions between a nanostructure and a substrate.

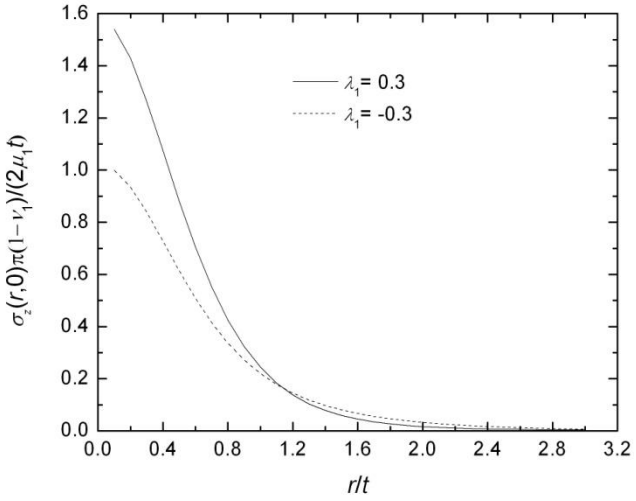

Figure 5.5: Normalized interface stress between a nanostructure and a substrate, which are perfectly bonded, under indentation using a conical indenter. $\lambda_1 = \pm 0.3$, $a/t = 0.1$.

5.6 Conclusions

In summary, the nanoindentation on a nanostructure-on-substrate system was revisited. Using Airy's functions, the kernel of the Fredholm integral equation was simplified. Modulus of a nanostructure-on-substrate system under a conical, spherical and a general indenter with calibrated area function *vs.* contact indentation depth were calculated. Compared to the finite element model presented in Chapter 3 and 4, the semi-analytical solution could greatly reduce the time of extracting the modulus of a nanostructure from a measured modulus of a nanostructure-on-substrate system. Moreover, the applicable range for the solution was discussed. The solution applies to a nanostructure with a width-to-thickness ratio larger than 4.

CHAPTER 6: CONCLUSIONS AND FUTURE WORK

6.1 Conclusions

AFAM based method was used to measure mechanical property of a BaB_6 nanostructure. During the experiment, an AFM tip could be easily blunted while it was in contact with a material having a Young's modulus higher than the material of tip, Si. Moreover, the mechanical property of the surface layer of the nanostructure could be measured because of the small load applied in the experiment, as discussed in Chapter 2. As a result, nanoindentation was mainly used to study mechanical property of nanostructures throughout the dissertation. Both experimental and numerical studies were carried out to investigate Young's modulus of nanostructures.

In single crystalline rutile TiO_2 nanoribbons under nanoindentation experiments, three different substrates, including SiO_2/Si, Si(100) and sapphire(0001), were used to support nanoribbons. AFM images of the nanoribbons after nanoindentation tests showed that the receding contact mechanics described the contact between the TiO_2 nanoribbons and a substrate well. In addition, finite element simulations demonstrated that sapphire was the best substrate to support TiO_2 nanoribbons. The modulus of a nanoribbon-on-sapphire system was close to the modulus of the nanoribbon itself, whereas the moduli of a nanoribbon-on-SiO_2/Si or a nanoribbon-on-Si system were quite different from modulus of the nanoribbon. The Young's modulus of TiO_2 nanoribbons was found to be around 360 GPa, which is comparable to that of bulk TiO_2.

In alkaline-earth metal hexaboride 1D nanostructures nanoindentation experiments, experimentally measured nanostructure-on-system moduli were scattering. Systematic experimental and numerical investigation revealed possible reasons for the data scattering, for example, the width and cross section of a nanostructure, the interaction between a nanostructure and a substrate. Using a rigid axi-symmetric indenter of a revolution spline, based on experimentally calibrated projected area of contact vs. h_c curve, modulus of a nanostructure was extracted from the measured modulus of the nanostructure-on-substrate system. The modulus was determined to fall between two bounds set by the receding contact and the perfect bond contact mechanisms between a nanostructure and a substrate, respectively. The extracted modulus increases as the width-to-thickness ratio of a nanostructure increases from one to two.

The process of extracting the modulus of a nanostructure from the measured system modulus is an iterative process–iteratively finds such a modulus of a nanostructure that the simulated modulus of the nanostructure-on-substrate system equals to the measured system modulus. Each simulation of nanostructure-on-substrate system modulus using a finite element model is time consuming. To speed-up the process, nanoindentation on a nanostructure-on-substrate system was "analytically" solved. The analytical solution applies to any nanostructures with a width to thickness ratio larger than 4.

6.2 Future Work

The dissertation mainly studied the mechanical properties of TiO_2 nanoribbons and MB_6 nanostructures using nanoindentation. An elastic finite element model and analytical solution were used in conjunction with experimental measurement to obtain

accurate intrinsic modulus of a nanostructure. There are a few areas could be improved along with the current research.

(i) Although Young's modulus of nanostructures can be deduced from the measured system modulus based on an elastic model of a nanostructure and a substrate, the hardness of the nanostructure should be extracted from measured system hardness based on a model including the plastic deformation for both the nanostructure and substrate. However, the elastic-plastic constitutive equations for the nanostructures studied here are lacking. Whether nanostructures are perfect-plastic or showing strain hardening are unclear at current stage. Future work could include obtaining a full stress-strain curve by conventional tensile tests for the studied materials.

(ii) Exploring of other mechanical property testing methods of nanostructures, such as a lateral three point bending test, and cross comparing the measured mechanical properties with current measured ones using nanoindentation. The lateral three point bending method is advantageous over a normal three point bending because it avoids contact of an AFM tip apex with nanostructures. The contact could be challenging when the tip size is comparable with dimension of a nanostructure so that sliding off could occur. The challenge does not exist for lateral three point bending, where side of a tip is in contact with the tested nanostructure. However, the AFM used to conduct a lateral bending test should be equipped with a closed-loop control in *z*-direction. With the control, the distance between

the AFM tip apex and the contact point between the nanostructure and side of AFM tip can be known. Moreover, the lateral spring constant of the AFM cantilever should be well calibrated. The spring constant should be comparable to that of the nanostructure under three point bending, as defined in Section 1.3.3. An AFM cantilever with too high spring constant is insensitive to the deflection of a nanostructure. An easy analogy to this would be: a weight scale for adult may not accurately measure the weight of a new-born baby. On the other hand, a cantilever with too small spring constant is insensitive to the deflection of the nanostructure neither since most deformation will come from the cantilever. Moreover, the sensitivity of AFM photodiode needs to be well calibrated so that the load applied on a nanostructure can be accurately determined.

(iii) Software development. Nanoindentation is mainly for mechanical property measurement of bulk materials. It gives a system modulus when a nanostructure or thin film-on-substrate system is tested. Complementary software may directly correlate the measured system modulus with the intrinsic modulus of the nanostructure or thin film. For nanostructures with large width to thickness ratio, such as a TiO_2 nanoribbon, the system modulus of a nanostructure-on-substrate system is discussed in Chapter 5. Given the system modulus M_{sys}, substrate modus μ_2, ν_2 , indenter displacement over thickness h/t, type of indenter (spherical, conical or a general indenter with calibrated area function *vs.* contact depth) and interaction boundary conditions between the nanostructure and the

substrate (frictionless contact or perfect bond) as inputs, the software should be able to extract modulus of the nanostructure directly using the data inverse process proposed in the Section 3.4.3.

REFERENCES

1. Adams, R. M., 1964. Boron, metallo-boron, compounds and boranes. Interscience Publishers, New York.

2. Agrawal, R., and Espinosa, H. D., 2009. Multiscale experiments: state of the art and remaining challenges. Journal of Engineering Materials and Technology-Transactions of the ASME 131, 041208.

3. Amin, S. S., Li, S. Y., Roth, J. R., and Xu, T. T., 2009. Single crystalline alkaline-earth metal hexaboride One-Dimensional (1D) nanostructures: synthesis and characterization. Chemistry of Materials 21, 763-770.

4. Amin, S. S., Nicholls, A. W., and Xu, T. T., 2007. A facile approach to synthesize single-crystalline rutile TiO_2 one-dimensional nanostructures. Nanotechnology 18, 445609.

5. Bei, H., George, E. P., Hay, J. L., and Pharr, G. M., 2005. Influence of indenter tip geometry on elastic deformation during nanoindentation. Physical Review Letters 95, 045501.

6. Belov, M., Quitoriano, N. J., Sharma, S., Hiebert, W. K., Kamins, T. I., and Evoy, S., 2008. Mechanical resonance of clamped silicon nanowires measured by optical interferometry. Journal of Applied Physics 103, 074304.

7. Binnig, G., Quate, C. F., and Gerber, C., 1986. Atomic force microscope. Physical Review Letters 56, 930-933.

8. Bückle, H., 1973. The science of hardness testing and its research applications. American Society for Materials.

9. Bunch, J. S., van der Zande, A. M., Verbridge, S. S., Frank, I. W., Tanenbaum, D. M., Parpia, J. M., Craighead, H. G., and McEuen, P. L., 2007. Electromechanical resonators from graphene sheets. Science 315, 490-493.

10. Burki, J., Stafford, C. A., and Stein, D. L., 2005. Theory of metastability in simple metal nanowires. Physical Review Letters 95, 090601.

11. Butt, H. J., Cappella, B., and Kappl, M., 2005. Force measurements with the atomic force microscope: technique, interpretation and applications. Surface Science Reports 59, 1-152.

12. Cappella, B., and Silbernagl, D., 2008. Nanomechanical properties of polymer thin films measured by force-distance curves. Thin Solid Films 516, 1952-1960.

13. Caron, A., and Arnold, W., 2009. Observation of local internal friction and plasticity onset in nanocrystalline nickel by atomic force acoustic microscopy. Acta Materialia 57, 4353-4363.

14. Chen, C. Q., Shi, Y., Zhang, Y. S., Zhu, J., and Yan, Y. J., 2006. Size dependence of Young's modulus in ZnO nanowires. Physical Review Letters 96, 075505.

15. Chen, S. H., Liu, L., and Wang, T. C., 2005. Investigation of the mechanical properties of thin films by nanoindentation, considering the effects of thickness and different coating-substrate combinations. Surface & Coatings Technology 191, 25-32.

16. Chen, X., and Mao, S. S., 2007. Titanium dioxide nanomaterials: Synthesis, properties, modifications, and applications. Chemical Reviews 107, 2891-2959.

17. Chen, X., and Vlassak, J. J., 2001. Numerical study on the measurement of thin film mechanical properties by means of nanoindentation. Journal of Materials Research 16, 2974-2982.

18. Chen, Y. Q., Zheng, X. J., Mao, S. X., and Li, W., 2010. Nanoscale mechanical behavior of vanadium doped ZnO piezoelectric nanofiber by nanoindentation technique. Journal of Applied Physics 107, 094302.

19. Chen, Y. X., Dorgan, B. L., McIlroy, D. N., and Aston, D. E., 2006. On the importance of boundary conditions on nanomechanical bending behavior and elastic modulus determination of silver nanowires. Journal of Applied Physics 100, 104301.

20. Chen, Y. X., Stevenson, I., Pouy, R., Wang, L. D., McIlroy, D. N., Pounds, T., Norton, M. G., and Aston, D. E., 2007. Mechanical elasticity of vapour-liquid-solid grown GaN nanowires. Nanotechnology 18, 135708.

21. Chueh, Y. L., Hsieh, C. H., Chang, M. T., Chou, L. J., Lao, C. S., Song, J. H., Gan, J. Y., and Wang, Z. L., 2007. RuO_2 nanowires and RuO_2/TiO_2 core/shell nanowires: From synthesis to mechanical, optical, electrical, and photoconductive properties. Advanced Materials 19, 143-149.

22. Ciocan, R., Gaillard, J., Skove, M. J., and Rao, A. M., 2005. Determination of the bending modulus of an individual multiwall carbon nanotube using an electric harmonic detection of resonance technique. Nano Letters 5, 2389-2393.

23. Clifford, C. A., and Seah, M. P., 2009. Nanoindentation measurement of Young's modulus for compliant layers on stiffer substrates including the effect of Poisson's ratios. Nanotechnology 20, 145708.

24. Dutta, S.K., 1975. Hot processing, strength and fracture of Calcium hexaboride. American Ceramic Society Bulletin 54**,** 727.

25. Dresselhaus, M. S., Chen, G., Tang, M. Y., Yang, R. G., Lee, H., Wang, D. Z., Ren, Z. F., Fleurial, J. P., and Gogna, P., 2007. New directions for low-dimensional thermoelectric materials. Advanced Materials 19, 1043-1053.

26. Dresselhaus, M. S., Dresselhaus, G., Sun, X., Zhang, Z., Cronin, S. B., and Koga, T., 1999. Low-dimensional thermoelectric materials. Physics of the Solid State 41, 679-682.

27. Ekinci, K. L., and Roukes, M. L., 2005. Nanoelectromechanical systems. Review of Scientific Instruments 76, 061101

28. El-gendi, S. E., 1969. Chebyshev solution of differential, integral and integro-differential equations. Computer Journal 12, 282-287.

29. Espinosa, H. D., Zhu, Y., and Moldovan, N., 2007. Design and operation of a MEMS-based material testing system for nanomechanical characterization. Journal of Microelectromechanical Systems 16, 1219-1231.

30. Feng, G., Nix, W. D., Yoon, Y., and Lee, C. J., 2006. A study of the mechanical properties of nanowires using nanoindentation. Journal of Applied Physics 99, 074304.

31. Frank, I. W., Tanenbaum, D. M., Van der Zande, A. M., and McEuen, P. L., 2007. Mechanical properties of suspended graphene sheets. Journal of Vacuum Science & Technology B 25, 2558-2561.

32. Futamoto, M., Aita, T., and Kawabe, U., 1979. Microhardness of hexaboride single-crystals. Materials Research Bulletin 14**,** 1329-1334.

33. Gaillard, J., Skove, M., and Rao, A. M., 2005. Mechanical properties of chemical vapor deposition-grown multiwalled carbon nanotubes. Applied Physics Letters 86, 233109.

34. Gan, M., Samvedi, V., Cerrone, A., Dubey, D. K., and Tomar, V., 2010. Effect of compressive straining on nanoindentation elastic modulus of trabecular bone. Experimental Mechanics 50, 773-781.

35. Gao, Y. F., Xu, H. T., Oliver, W. C., and Pharr, G. M., 2008. Effective elastic modulus of film-on-substrate systems under normal and tangential contact. Journal of the Mechanics and Physics of Solids 56, 402-416.

36. Geng, K., Yang, F., and Grulke, E. A., 2008. Nanoindentation of submicron polymeric coating systems. Materials Science and Engineering: A 479, 157-163.

37. Ghebouli, B., Ghebouli, M. A., Fatmi, M., and Benkerri, M., First-principles calculations of structural, elastic, electronic and optical properties of XO (X=Ca,

Sr and Ba) compounds under pressure effect. Materials Science in Semiconductor Processing 13, 92-101.

38. Gomez-Navarro, C., Burghard, M., and Kern, K., 2008. Elastic properties of chemically derived single graphene sheets. Nano Letters 8, 2045-2049.

39. Gordon, M. J., Baron, T., Dhalluin, F., Gentile, P., and Ferret, P., 2009. Size effects in mechanical deformation and fracture of cantilevered silicon nanowires. Nano Letters 9, 525-529.

40. Grechnev, G. E., Baranovskiy, A. E., Fil, V. D., Ignatova, T. V., Kolobov, I. G., Logosha, A. V., Shitsevalova, N. Y., Filippov, V. B., and Eriksson, O., 2008. Electronic structure and bulk properties of MB_6 and MB_{12} borides. Low Temperature Physics 34, 921-929.

41. Hainsworth, S. V., Chandler, H. W., and Page, T. F., 1996. Analysis of nanoindentation load-displacement loading curves. Journal of Materials Research 11, 1987-1995.

42. Han, S. M., Saha, R., and Nix, W. D., 2006. Determining hardness of thin films in elastically mismatched film-on-substrate systems using nanoindentation. Acta Materialia 54, 1571-1581.

43. Han, X. D., Zheng, K., Zhang, Y. F., Zhang, X. N., Zhang, Z., and Wang, Z. L., 2007. Low-temperature in situ large-strain plasticity of silicon nanowires. Advanced Materials 19, 2112-2118.

44. Hao, F., Fang, D., and Xu, Z., 2011. Mechanical and thermal transport properties of graphene with defects. Applied Physics Letters 99, 041901.

45. Heim, L. O., Kappl, M., and Butt, H. J., 2004. Tilt of atomic force microscope cantilevers: Effect on spring constant and adhesion measurements. Langmuir 20, 2760-2764.

46. Huang, L., Meyer, C., and Prater, C., 2007. Eliminating lateral forces during AFM indentation. Journal of Physics: Conference Series 61, 805-809.

47. Huang, X. H., Quinto-Su, P. A., Gonzalez-Avila, S. R., Wu, T., and Ohl, C. D., 2010. Controlled manipulation and in situ mechanical measurement of single Co nanowire with a laser-induced cavitation bubble. Nano Letters 10, 3846-3851.

48. Hurley, D. C., Kopycinska-Muller, M., and Kos, A. B., 2007. Mapping mechanical properties on the nanoscale using atomic-force acoustic microscopy. Jom 59, 23-29.

49. Hurley, D. C., and Turner, J. A., 2007. Measurement of Poisson's ratio with contact-resonance atomic force microscopy. Journal of Applied Physics 102, 033509.

50. Hutter, J. L., and Bechhoefer, J., 1993. Calibration of atomic-force microscope tips. Review of Scientific Instruments 64, 1868-1873.

51. Iijima, S., Brabec, C., Maiti, A., and Bernholc, J., 1996. Structural flexibility of carbon nanotubes. Journal of Chemical Physics 104, 2089-2092.

52. Imai, Y., Mukaida, M., Ueda, M., and Watanabe, A., 2001. Screening of the possible boron-based *n*-type thermoelectric conversion materials on the basis of the calculated densities of states of metal borides and doped beta-boron. Intermetallics 9, 721-734.

53. Jee, A. Y., and Lee, M., 2010. Comparative analysis on the nanoindentation of polymers using atomic force microscopy. Polymer Testing 29, 95-99.

54. Jeon, S., Braiman, Y., and Thundat, T., 2004. Torsional spring constant obtained for an atomic force microscope cantilever. Applied Physics Letters 84, 1795-1797.

55. Jha, K. K., Suksawang, N., and Agarwal, A., 2010. Analytical method for the determination of indenter constants used in the analysis of nanoindentation loading curves. Scripta Materialia 63, 281-284.

56. Joslin, D. L., and Oliver, W. C., 1990. A new method for analyzing data from continuous depth-sensing microindentation test. Journal of Materials Research 5, 123-126.

57. Kauzlarich, J. J., and Greenwood, J. A., 2001. Contact between a centrally loaded plate and a rigid or elastic base, with application to pivoted pad bearings. Proceedings of the Institution of Mechanical Engineers Part C-Journal of Mechanical Engineering Science 215, 623-628.

58. Keer, L. M., Dundurs, J., and Tsai, K. C., 1972. Problems involving a receding contact between a layer and a half space. Journal of Applied Mechanics-Transactions of the ASME 39, 1115-1120.

59. King, R. B., 1987. Elastic analysis of some punch problems for a layered medium. International Journal of Solids and Structures 23, 1657-1664.

60. Kopycinska-Muller, M., Geiss, R. H., and Hurley, D. C., 2006. Contact mechanics and tip shape in AFM-based nanomechanical measurements. Ultramicroscopy 106, 466-474.

61. Kosolapova, T. Y., 1990. Handbook of high temperature compounds: properties, production, applications. Hemisphere, New York.

62. Kovalev, A., Shulha, H., Lemieux, M., Myshkin, N., and Tsukruk, V. V., 2004. Nanomechanical probing of layered nanoscale polymer films with atomic force microscopy. Journal of Materials Research 19, 716-728.

63. Krishnan, A., Dujardin, E., Ebbesen, T. W., Yianilos, P. N., and Treacy, M. M. J., 1998. Young's modulus of single-walled nanotubes. Physical Review B 58, 14013-14019.

64. Kumar, P., and Kiran, M., 2010. Nanomechanical characterization of Indium nano/microwires. Nanoscale Research Letters 5, 1085-1092.

65. Lee, C., Wei, X. D., Kysar, J. W., and Hone, J., 2008. Measurement of the elastic properties and intrinsic strength of monolayer graphene. Science 321, 385-388.

66. Li, H., and Bradt, R., 1993. The microhardness indentation load/size effect in rutile and cassiterite single crystals. Journal of Materials Science 28, 917-926.

67. Li, X. D., Chasiotis, I., and Kitamura, T., 2010. In situ scanning probe microscopy nanomechanical testing. MRS Bulletin 35, 361-367.

68. Li, X. D., Wang, X. N., Xiong, Q. H., and Eklund, P. C., 2005. Mechanical properties of ZnS nanobelts. Nano Letters 5, 1982-1986.

69. Lozano, J. R., and Garcia, R., 2008. Theory of multifrequency atomic force microscopy. Physical Review Letters 100, 076102.

70. Lozano, J. R., and Garcia, R., 2009. Theory of phase spectroscopy in bimodal atomic force microscopy. Physical Review B 79, 014110.

71. Lu, Y., Ganesan, Y., and Lou, J., 2010. A multi-step method for in situ mechanical characterization of 1-D nanostructures using a novel micromechanical device. Experimental Mechanics 50, 47-54.

72. Lucas, M., Leach, A. M., McDowell, M. T., Hunyadi, S. E., Gall, K., Murphy, C. J., and Riedo, E., 2008. Plastic deformation of pentagonal silver nanowires: Comparison between AFM nanoindentation and atomistic simulations. Physical Review B 77, 245420.

73. Lucas, M., Mai, W. J., Yang, R. S., Wang, Z. L., and Riedo, E., 2007. Size dependence of the mechanical properties of ZnO nanobelts. Philosophical Magazine 87, 2135-2141.

74. Mai, W. J., and Wang, Z. L., 2006. Quantifying the elastic deformation behavior of bridged nanobelts. Applied Physics Letters 89, 073112.

75. Mao, S. X., Zhao, M. H., and Wang, Z. L., 2003. Nanoscale mechanical behavior of individual semiconducting nanobelts. Applied Physics Letters 83, 993-995.

76. Maugis, D., 2000. Contact, adhesion and rupture of elastic solids. Springer, Berlin.

77. Mayo, M. J., Siegel, R. W., Narayanasamy, A., and Nix, W. D., 1990. Mechanical properties of nanophase TiO_2 as determined by nanoindentation. Journal of Materials Research 5, 1073-1082.

78. Miller, R. E., and Shenoy, V. B., 2000. Size-dependent elastic properties of nanosized structural elements. Nanotechnology 11, 139-147.

79. MTS, 2007. G200 nanoindenter manual. Document No. G2A-13192-0.

80. Ngo, L. T., Almecija, D., Sader, J. E., Daly, B., Petkov, N., Holmes, J. D., Erts, D., and Boland, J. J., 2006. Ultimate-strength germanium nanowires. Nano Letters 6, 2964-2968.

81. Ogletree, D. F., Carpick, R. W., and Salmeron, M., 1996. Calibration of frictional forces in atomic force microscopy. Review of Scientific Instruments 67, 3298-3306.

82. Oliver, W. C., and Pharr, G. M., 1992. An improved technique for determining hardness and elastic-modulus using load and displacement sensing indentation experiments. Journal of Materials Research 7, 1564-1583.

83. Palacio, M. L. B., and Bhushan, B., 2010. Normal and lateral force calibration techniques for AFM cantilevers. Critical Reviews in Solid State and Materials Sciences 35, 73-104.

84. Park, H. S., Cai, W., Espinosa, H. D., and Huang, H. C., 2009. Mechanics of crystalline nanowires. MRS Bulletin 34, 178-183.

85. Pettersson, T., Nordgren, N., and Rutland, M. W., 2007. Comparison of different methods to calibrate torsional spring constant and photodetector for atomic force microscopy friction measurements in air and liquid. Review of Scientific Instruments 78, 093702.

86. Poncharal, P., Wang, Z. L., Ugarte, D., and de Heer, W. A., 1999. Electrostatic deflections and electromechanical resonances of carbon nanotubes. Science 283, 1513-1516.

87. Poot, M., and van der Zant, H. S. J., 2008. Nanomechanical properties of few-layer graphene membranes. Applied Physics Letters 92, 063111.

88. Rabe, U., Amelio, S., Kester, E., Scherer, V., Hirsekorn, S., and Arnold, W., Quantitative determination of contact stiffness using atomic force acoustic microscopy. 2000, 38, 430-437.

89. Rabe, U., Janser, K., and Arnold, W., 1996. Vibrations of free and surface-coupled atomic force microscope cantilevers: Theory and experiment. Review of Scientific Instruments 67, 3281-3293.

90. Raman, A., Melcher, J., and Tung, R., 2008. Cantilever dynamics in atomic force microscopy. Nano Today 3, 20-27.

91. San Paulo, A., Bokor, J., Howe, R. T., He, R., Yang, P., Gao, D., Carraro, C., and Maboudian, R., 2005. Mechanical elasticity of single and double clamped silicon nanobeams fabricated by the vapor-liquid-solid method. Applied Physics Letters 87, 053111.

92. Shang, S. L., Wang, Y., and Liu, Z. K., 2007. First-principles calculations of phonon and thermodynamic properties in the boron-alkaline earth metal binary systems: B-Ca, B-Sr, and B-Ba. Physical Review B 75, 024302.

93. Shu, S. Q., Yang, Y., Fu, T., Wen, C. S., and Lu, J., 2009. Can Young's modulus and hardness of wire structural materials be directly measured using nanoindentation? Journal of Materials Research 24, 1054-1058.

94. Silva, E., Tong, L. M., Yip, S., and Van Vliet, K. J., 2006. Size effects on the stiffness of silica nanowires. Small 2, 239-243.

95. Sohn, Y. S., Park, J., Yoon, G., Song, J., Jee, S. W., Lee, J. H., Na, S., Kwon, T., and Eom, K., 2010. Mechanical properties of silicon nanowires. Nanoscale Research Letters 5, 211-216.

96. Song, J. H., Wang, X. D., Riedo, E., and Wang, Z. L., 2005. Elastic property of vertically aligned nanowires. Nano Letters 5, 1954-1958.

97. Stan, G., Ciobanu, C. V., Parthangal, P. M., and Cook, R. F., 2007. Diameter-dependent radial and tangential elastic moduli of ZnO nanowires. Nano Letters 7, 3691-3697.

98. Stan, G., Ciobanu, C. V., Thayer, T. P., Wang, G. T., Creighton, J. R., Purushotham, K. P., Bendersky, L. A., and Cook, R. F., 2009. Elastic moduli of faceted aluminum nitride nanotubes measured by contact resonance atomic force microscopy. Nanotechnology 20, 035706.

99. Stan, G., Krylyuk, S., Davydov, A. V., and Cook, R. F., 2010. Compressive stress effect on the radial elastic modulus of oxidized Si nanowires. Nano Letters 10, 2031-2037.

100. Stan, G., Krylyuk, S., Davydov, A. V., Vaudin, M. D., Bendersky, L. A., and Cook, R. F., Contact-resonance atomic force microscopy for nanoscale elastic property measurements: Spectroscopy and imaging. 2009, 108, 929-936.

101. Stan, G., and Price, W., 2006. Quantitative measurements of indentation moduli by atomic force acoustic microscopy using a dual reference method. Review of Scientific Instruments 77, 103707.

102. Stiernstedt, J., Rutland, M. W., and Attard, P., 2005. A novel technique for the in situ calibration and measurement of friction with the atomic force microscope. Review of Scientific Instruments 76, 083710.

103. Tabib-Azar, M., Nassirou, M., Wang, R., Sharma, S., Kamins, T. I., Islam, M. S., and Williams, R. S., 2005. Mechanical properties of self-welded silicon nanobridges. Applied Physics Letters 87, 113102.

104. Takeda, M., Terui, M., Takahashi, N., and Ueda, N., 2006. Improvement of thermoelectric properties of alkaline-earth hexaborides. Journal of Solid State Chemistry 179, 2823-2826.

105. Tan, E. P. S., Goh, C. N., Sow, C. H., and Lim, C. T., 2005. Tensile test of a single nanofiber using an atomic force microscope tip. Applied Physics Letters 86, 073115.

106. Tao, X. Y., Wang, X. N., and Li, X. D., 2007. Nanomechanical characterization of one-step, combustion-synthesized $Al_4B_2O_9$ and $Al_{18}B_4O_{33}$ nanowires. Nano Letters 7, 3172-3176.

107. Turner, J. A., Hirsekorn, S., Rabe, U., and Arnold, W., 1997. High-frequency response of atomic-force microscope cantilevers. Journal of Applied Physics 82, 966-979.

108. Van Dorp, W. F., and Hagen, C. W., 2008. A critical literature review of focused electron beam induced deposition. Journal of Applied Physics 104, 081301.

109. Vlassak, J. J., and Nix, W. D., 1994. Measuring the elastic properties of anisotropic materials by means of indentation experiments. Journal of the Mechanics and Physics of Solids 42**,** 1223-1245.

110. Walavalkar, S. S., Homyk, A. P., Henry, M. D., and Scherer, A., 2010. Controllable deformation of silicon nanowires with strain up to 24%. Journal of Applied Physics 107, 124314.

111. Wei, Y.-K., Yu, J.-X., Li, Z.-G., Cheng, Y., and Ji, G.-F., 2011. Elastic and thermodynamic properties of CaB_6 under pressure from first principles. Physica B: Condensed Matter 406**,** 4476-4482.

112. Wong, E. W., Sheehan, P. E., and Lieber, C. M., 1997. Nanobeam mechanics: Elasticity, strength, and toughness of nanorods and nanotubes. Science 277, 1971-1975.

113. Wu, B., Heidelberg, A., and Boland, J. J., 2005. Mechanical properties of ultrahigh-strength gold nanowires. Nature Materials 4, 525-529.

114. Wu, B., Heidelberg, A., Boland, J. J., Sader, J. E., Sun, X. M., and Li, Y. D., 2006. Microstructure-hardened silver nanowires. Nano Letters 6, 468-472.

115. Xia, Y. N., Yang, P. D., Sun, Y. G., Wu, Y. Y., Mayers, B., Gates, B., Yin, Y. D., Kim, F., and Yan, Y. Q., 2003. One-dimensional nanostructures: Synthesis, characterization, and applications. Advanced Materials 15, 353-389.

116. Xin, S., Liu, S., Wang, N., Han, X., Wang, L., Xu, B., Tian, Y., Liu, Z., He, J., and Yu, D., 2011. Formation and properties of SrB_6 single crystals synthesized under high pressure and temperature. Journal of Alloys and Compounds 509**,** 7927-7930.

117. Xiong, Q. H., Duarte, N., Tadigadapa, S., and Eklund, P. C., 2006. Force-deflection spectroscopy: A new method to determine the Young's modulus of nanofilaments. Nano Letters 6, 1904-1909.

118. Xu, T. T., Zheng, J. G., Nicholls, A. W., Stankovich, S., Piner, R. D., and Ruoff, R. S., 2004. Single-crystal calcium hexaboride nanowires: Synthesis and characterization. Nano Letters 4, 2051-2055.

119. Xu, Z.-H., and Li, X., 2006. Sample size effect on nanoindentation of micro-/nanostructures. Acta Materialia 54, 1699-1703.

120. Yang, F. Q., Jiang, C. B., Du, W. W., Zhang, Z. Q., Li, S. X., and Mao, S. X., 2005. Nanomechanical characterization of ZnS nanobelts. Nanotechnology 16, 1073-1077.

121. Yu, H. Y., Sanday, S. C., and Rath, B. B., 1990. The effect of substrate on the elastic properties of films determined by the indentation test - Axisymmetrical Boussinesq problem. Journal of the Mechanics and Physics of Solids 38, 745-764.

122. Yu, M. F., Dyer, M. J., Skidmore, G. D., Rohrs, H. W., Lu, X. K., Ausman, K. D., Von Ehr, J. R., and Ruoff, R. S., 1999. Three-dimensional manipulation of carbon nanotubes under a scanning electron microscope. Nanotechnology 10, 244-252.

123. Yu, M. F., Lourie, O., Dyer, M. J., Moloni, K., Kelly, T. F., and Ruoff, R. S., 2000. Strength and breaking mechanism of multiwalled carbon nanotubes under tensile load. Science 287, 637-640.

124. Zhang, D. F., Breguet, J. M., Clavel, R., Sivakov, V., Christiansen, S., and Michler, J., 2010. Electron microscopy mechanical testing of silicon nanowires using electrostatically actuated tensile stages. Journal of Microelectromechanical Systems 19, 663-674.

125. Zhang, H., Tang, J., Zhang, L., An, B., and Qin, L. C., 2008. Atomic force microscopy measurement of the Young's modulus and hardness of single LaB_6 nanowires. Applied Physics Letters 92, 173121.

126. Zhang, T. H., Feng, Y. H., Yang, R., and Jiang, P., A method to determine fracture toughness using cube-corner indentation. Scripta Materialia 62, 199-201.

127. Zhang, Y., 2010. Extracting nanobelt mechanical properties from nanoindentation. Journal of Applied Physics 107, 123518.

128. Zhao, M. H., Xiang, Y., Xu, J., Ogasawara, N., Chiba, N., and Chen, X., 2008. Determining mechanical properties of thin films from the loading curve of nanoindentation testing. Thin Solid Films 516, 7571-7580.

129. Zhao, Q. Z., Nardelli, M. B., and Bernholc, J., 2002. Ultimate strength of carbon nanotubes: A theoretical study. Physical Review B 65, 144105.

130. Zhu, Y., and Espinosa, H. D., 2005. An electromechanical material testing system for in situ electron microscopy and applications. Proceedings of the National Academy of Sciences of the United States of America 102, 14503-14508.

131. Zhu, Y., Ke, C., and Espinosa, H. D., 2007. Experimental techniques for the mechanical characterization of one-dimensional nanostructures. Experimental Mechanics 47, 7-24.

132. Zhu, Y., Xu, F., Qin, Q. Q., Fung, W. Y., and Lu, W., 2009. Mechanical properties of vapor-liquid-solid synthesized silicon nanowires. Nano Letters 9, 3934-3939.

133. Zhu, Y. W., Murali, S., Cai, W. W., Li, X. S., Suk, J. W., Potts, J. R., and Ruoff, R. S., 2010. Graphene and graphene oxide: Synthesis, properties, and applications. Advanced Materials 22, 3906-3924.

134. Zienkiewicz, O. C., 1989. The finite element method. McGraw-Hill, London.